Development of specimen mounting and gripping system for planar biaxial tensile testing of biological membrane tissue

Aashir Siddiqui

Dissertation presented in partial fulfilment of the requirements of the degree of Master of Science

Blast Impact and Survivability Research Unit
Department of Mechanical Engineering
University of Cape Town

February 2023

Declaration

I, Aashir Siddiqui , hereby:

(a) grant the University of Cape Town free license to reproduce the above thesis in whole or in part, for the purpose of research;

(b) declare that:

(i) the above thesis is my own unaided work, both in concept and execution, and that apart from the normal guidance from my supervisor, I have received no assistance apart from that explicitly stated in the Acknowledgements.

(ii) neither the substance nor any part of the above thesis has been submitted in the past, or is being, or is to be submitted for a degree at this University or at any other university.

I am now presenting the report for examination for the degree of M.Sc Eng (Mechanical) .

Signed by candidate

A. Siddiqui

10 February 2023

Abstract

There has always been a need to understand the mechanical properties of biological membrane tissues in the fields of medicine, biomechanical engineering, and cosmetology. These tissues are known to display complex anisotropic, hyperelastic, and non-linear stress-strain properties, while also being sensitive to environmental conditions. Given these complexities, ongoing efforts are being made to develop a suitable testing methodology. At the University of Cape Town, the Blast Impact and Survivability Research Unit is building a testing methodology (using their in-house planar biaxial tensile testing and bulge inflation devices) that has thus far been used to test small intestine submucosa tissue. As part of this ongoing effort, this research aimed to build a tissue-gripping system that can be used to attach a specimen to the planar biaxial tensile testing machine since the previous clamping method was not suitable. A rake clamping system that allowed contra-lateral motion was built, along with the necessary tooling to attach the rakes and excise a square-shaped specimen. Planar biaxial tensile tests were then conducted on small intestine submucosa tissue to assess the performance of these rakes. The rakes were found to be effective at allowing the tissue to expand and contract contra-laterally while also being structurally sound enough to withstand the loads applied during testing. In the progression of this research, improvements were also made to the optical deformation measurements and sample thickness measurements. Regarding the optical deformation measurements, it was found that speckling the sample with multi-coloured paints improved correlation, and the addition of Cross Polarising Line filters removed harsh reflections that would stop the Digital Image Correlation software from evaluating facet displacement. Looking at the thickness measurements, a migration was made from wax histology to cryo-histology for preparing sections to measure the samples' thickness. Images taken showed that the cryo-sectioned tissue had undergone less dilation and fibre fraying than the wax histology used by prior students, offering more realistic and accurate thickness measurements. The successes found with the designed rakes and the improvements made to the testing methodology have laid the groundwork for other biological tissues to be tested.

Acknowledgements

In the name of Allah, The Most Gracious and The Most Merciful

I would like to express my deepest gratitude to my supervisor, Dr Reuben Govender. Without his endless support, mentorship, and engineering passion, this dissertation would not have come to fruition. His feedback and cross-disciplinary knowledge were invaluable in maintaining the momentum of this research over the past two years.

I would like to thank Mr Pierre Smith and his team at the workshop for machining and assembling the many components for this research, including the permission to use the machinery when required.

My thanks also go to the staff at the Centre for Materials Engineering, for offering their space to conduct all experiments. A special mention must go to Maxwell Vos, for spending countless hours with me in the lab, figuring out how best to configure the DIC equipment to achieve good strain data.

I would also like to thank the staff at BISRU for always offering constructive feedback and handling all administrative issues during my degree. My sincere gratitude goes to my post-graduate colleagues (Matthew, Pierre, Nicholas, and Malcolm) for all the extra-curricular activities and humour, which were extremely helpful in lifting my spirits throughout this research.

Most importantly, I would like to thank my mother and my father for their complete love and everlasting support throughout my life.

Contents

1 Introduction **1**

1.1 Background 1

1.2 Objectives 2

1.3 Scope 2

1.4 Dissertation Outline 2

2 Literature Review **5**

2.1 Background on Biology Soft Tissue 5

2.1.1 Structural Composition of Skin 5

2.1.2 Mechanical Properties of Skin 7

2.1.3 Surrogate Test Tissue 10

2.2 Soft Tissue Mechanical Testing Methods 11

2.2.1 Uniaxial Tensile Testing 12

2.2.2 Biaxial Tensile Testing 13

2.2.3 Gripping Methods 15

2.3 Preconditioning 19

2.4 Constitutive Models of Skin 20

2.4.1 Isotropic Models 21

2.4.2 Anisotropic Models 23

2.5 Digital Image Correlation 27

2.5.1 Background 27
2.5.2 Speckling 28
2.5.3 Optics and Lighting 29

3 Design of Experimental Apparatus 31

3.1 Overview of Current Devices 31
3.1.1 Bulge Testing Device 31
3.1.2 Planar Biaxial Tensile Testing Device 32
3.2 Selection of Clamping Configuration 33
3.3 Design Constraints and Specification 34
3.4 Design of Specimen Geometry 34
3.5 Rake Design 35
3.5.1 Fabrication and Assembly of Rakes 36
3.6 Design of Specimen Preparation Rigs 38
3.6.1 Rake Attachment Rig 38
3.6.2 Specimen Punching Device 39
3.6.3 Lifting and Transportation Card 41
3.7 General Modification 42
3.7.1 Biaxial Arms 42
3.7.2 Saline Bath 43
3.7.3 Sleeves 43
3.7.4 PBT DIC Calibration Card Seat 44
3.7.5 Pin Alignment Tool 44

4 Experimental Methodology 47

4.1 Strain Measurement Technique 47
4.1.1 Optics and Lighting Condition 47
4.1.2 Speckling Technique 51

4.2 Sample Preparation for Bulge Test 53
4.3 Bulge Test Methodology 54
4.3.1 Calibration of DIC Equipment 54
4.3.2 Loading and Inflating Sample 55
4.3.3 Mean Fibre Axes Identification 55
4.4 Sample Preparation for PBT test 56
4.4.1 Rake Attachment Process 56
4.4.2 Punching Square Shape 58
4.4.3 Loading Sample 58
4.5 PBT Test Methodology 60
4.5.1 Configuration and Calibration of DIC equipment 60
4.5.2 PBT Extension Protocol 60
4.6 Specimen Thickness Measurement 61
4.6.1 Cryo-section Histology Methodology 61
4.6.2 Image Processing 63

5 Results and Discussions **65**

5.1 Assessment of Designed Components 65
5.1.1 Rakes 65
5.1.2 Rake Attachment Rig 66
5.1.3 Specimen Punching Rig 66
5.1.4 Transportation Card 67
5.2 Assessment of Optical Measuring Technique 68
5.2.1 CPL Effect on Image Quality 68
5.2.2 Speckling with Multi-coloured Paints 69
5.3 Discussion of Experimental Results 70
5.3.1 MFA Identification and Isotropic Index 70

5.3.2 Results From Cryo-histology 72
5.3.3 Overview of Stress-strain Curves From PBT 73
5.3.4 Discussion on Strain Induced During Bulge Testing 77
5.3.5 Out of Plane Displacement During PBT Tests 77
5.4 Curve Fitting GOH Model 79

6 Conclusions and Recommendations 83
6.1 Novel Experimental Hardware Performance 83
6.1.1 Rakes 83
6.1.2 Rake Attachment Rig 84
6.1.3 Specimen Punching Rig 84
6.1.4 Transportation Card 84
6.2 Improvements to Deformation Measurements 85
6.3 Thickness Measurements via Cryo-histology 85
6.4 Constitutive Model Parameter Fitting 85
6.5 Recommendations 86

Appendices 97

A Preliminary Design Concepts 97
A.1 Specimen cutting rig 97
A.2 Rake attachment prototype 100
A.3 Transportation tool 101

B Casting Process and Sleeve Heights 103
B.1 Casting rubber mat 104
B.2 Sleeve Heights 106

C Comprehensive experimental results 109

C.1 Bulge-test results 110
C.2 PBT Video Recordings 111
C.3 Stress-strain curves 112
C.4 Bulge-test strain maps 122
C.5 Greyscale Charts 126

D Curve Fitting Experimental Data **135**
D.1 Gasser-Ogden-Holfzapfel Material Model 135

E Cryo-Histology **139**
E.1 Qualitative assessment of two different preparation methods 139
E.2 Qualitative assessment between various section thickness used 140

F Engineering Drawings **143**

List of Figures

2.1 Illustration of the different layers of skin [13] 6

2.2 Schematic representation of a typical stress-strain curve for skin with collagen fibre morphology [17] 7

2.3 Langer lines mapped on the human body [21] 8

2.4 Stress-strain response captured along and perpendicular to the fibre direction [22] 9

2.5 Stress-strain response captured at 0°(blue), 45°(green) and 90°(red) [23] . . 9

2.6 Uniaxial stress-strain curves on pig skin at different strain rates [29] 10

2.7 Illustration of a skin creep curved under a uniform load [32] 10

2.8 Structure of small intestine [34] 11

2.9 Photograph of porcine skin loaded on a uniaxial tensile test device with a jaw clamp [38] 13

2.10 Illustration of a Planar biaxial tensile testing [50] 14

2.11 Illustration of bulge test method [55] 15

2.12 Illustration of different gripping methods [59] 16

2.13 Photograph showing a clamped specimen [10] 16

2.14 Von Mises stress and deformation of a clamped specimen [52] 17

2.15 Photograph showing a sutured specimen [61] 17

2.16 Von Mises stress and deformation of a sutured specimen [52] 18

2.17 Illustration of CellScale BioTester rakes [64] 18

2.18 Preconditioning of a typical pig skin sample [65] 19

2.19 Illustration of DIC setup to capture sample inflation on a bulge tester [10] 28

2.20 Schematic showing spray method to speckle a sample [10] 29

3.1 Photograph of bulge testing device [9] 32

3.2 Sub-assembly of clamping configuration [10] 32

3.3 The rendered image of biaxial tensile testing machine [8] 33

3.4 Illustration of sample size and geometry 35

3.5 Image showing rake design 35

3.6 Image showing resin printed clip 36

3.7 Photograph of Glueing Jig with needles being bonded to their adapters . . 37

3.8 Photograph of needles seated in the bending jig 37

3.9 Photograph of needle bending operation 37

3.10 General assembly of rake attachment device 38

3.11 General assembly of Punch Mechanism 40

3.12 Images of hardened punch and cast rubber matt 41

a Model of hardened punch 41

b Photograph showing cast rubber base 41

3.13 Illustration of Lifting card fitted onto the rakes 42

3.14 Illustration of saline bath 43

3.15 Photograph of sleeve fitted on a biaxial arm 43

3.16 Photograph of the PBT DIC Calibration Card Seat 44

3.17 Photograph of pin alignment card locating the positions of the arms 45

4.1 Configuration for planar biaxial test 48

4.2 Configuration for inflation test [10] 48

4.3 Demonstration of a specimen under different exposure 49

a Underexposed 49

b Well exposed 49

4.4 Visualisation of how cross polarising filters interacts with light [82] 50

4.5 Demonstration of the effect of capturing images with polarised filters under the same lighting condition 50

a Image captured without polarised filters 50

b Image captured with polarised filters 50

4.6 Photographs showing new camera configurations 52

a New planar biaxial tensile test camera configuration 52

b New inflation test camera configuration 52

4.7 Opening SIS tissue to rectangular form [10] 53

4.8 Demonstration of calibration card seated in different orientations on the bulge tester 54

a Image of calibration card seated in plane 54

b Image of calibration card seated at an angle 54

4.9 Photographs of specimen undergoing a bulge test 56

a Image of specimen loaded onto device 56

b Image of specimen fully inflated 56

4.10 Screenshot of output from Algorithm 57

4.11 Photographs showing the final step of (a) lowering the tissue, (b) piercing it and (c) depositing it on the rubber base 57

a 57

b 57

c 57

4.12 Photograph of punching rig assembled and positioned under an arbor press 58

4.13 Photograph of punched sample 59

4.14 Removal of excess tissue post punch 59

a Image of side excision being made onto excess tissue 59

b Image of excess material being removed 59

4.15 Plan view of sample fitted on transportation card 59

4.16 Photographs displaying steps to load sample onto the PBT 60

a Image of card with sample seated 60

b Image of sample seated alone 60

4.17 Demonstration of calibration card seated in different orientations on the PBT 61

a Image of calibration card in plane 61

b Image of angled calibration card 61

4.18 Photograph displaying specimen seated in square mould 62

4.19 Photograph of filled mould placed in polystyrene box in preparation for freezing 62

4.20 Example of ImageJ processisng using prepared specimen 8 slide 64

a Image of sectioned tissue inserted as an input 64

b Processed image where tissue has been identified and isolated from background 64

c Output from macro tool, showing sampled sections and lengths measured 64

5.1 Images highlighting the displacement of the hooks to allow contra-lateral expansion of the tested tissue 65

a Image captured of sample in its rest position 65

b Image captured of sample under full extension 65

5.2 Photographs showing intermediate steps taken during the transportation of the sample 67

a Photograph of rubber matt being removed 67

b Photograph of lowering sample 67

5.3 Differences between images taken with and without CPL filters with the aid of HSB color charts 68

a Image captured with non-polarised filter 68

b Image captured with polarised filter 68

5.4 Comparison of Greyscale values obtained with and without CPL filters . . 69

a Greyscale chart of Specimen 2 69

b Greyscale chart of Specimen 8 69

5.5 Greyscale values seen on different colour schemes 70

5.6 Bar chart showing isotropic index determined from bulge tests 71

5.7 Bar chart showing thicknesses measured using cryo-histology 72

5.8 Bar chart comparing thickness measured between the two methods 73

5.9 Visual comparison of specimens prepared under cryo and wax-histology method 74

a Image captured of cryo-sectioned sample 74

b Image captured of a wax-sectioned sample [10] 74

5.10 Specimen 5 PBT test results 75

5.11 Compiled stress-strain response along the CFA axis 76

5.12 Compiled stress-strain response along the MFA axis 76

5.13 Image showing the principal strains recorded for Specimen 5 under maximum inflation 77

a Principle strain 1 77

b Principle strain 2 77

5.14 Compiled out of plane displacement observed for 1:1 extension ratio 78

5.15 Graphs showing curve fitting of material model onto experimental results . 79

a Specimen 3 79

b Specimen 5 79

A.1 Rendered image of the cutting tool 97

A.2 Rendered image of the cutting rig 98

A.3 Photographs showing the punch being tested and the result after punching 99

a Photograph of round punch being tested 99

b Photograph showing the results after punching 99

A.4 Photographs showing the square punch post test, the square sample produced and the wear on the die . . . 99
a Embedded sample . . . 99
b Punched material . . . 99
c Blunted die . . . 99
A.5 Photograph of rake attachment rig prototype . . . 100
A.6 Photographs showing sample lowered onto the platform and attached to the hooks . . . 101
a Sample lowered onto the platform . . . 101
b Sample attached to the hooks . . . 101
A.7 Illustration showing isometric and section views of the transportation tool 102
a Isometric View . . . 102
b Section View . . . 102
A.8 Diagram showing the configuration for the transportation to be switched off and on . . . 102
a Switched off . . . 102
b Switched on . . . 102

B.1 Illustration of the upper-half and lower-half of the mould . . . 104
a Upper-half . . . 104
b Lower-half . . . 104
B.2 Image of mould after overnight curing . . . 105
B.3 Image taken after removal of the upper-half mould . . . 106
B.4 Image of the cast rubber mats with excess material . . . 106
B.5 Diagram showing sleeve fitted onto arms . . . 106

C.1 Results obtained from Bulge tester for the first four specimens . . . 110
a Specimen 1 . . . 110
b Specimen 2 . . . 110

c Specimen 3 . . . 110
d Specimen 4 . . . 110
e Specimen 5 . . . 110
C.1 Results obtained from Bulge tester for the remaining three specimens . . . 111
f Specimen 6 . . . 111
g Specimen 7 . . . 111
h Specimen 8 . . . 111
i Specimen 9 . . . 111
C.2 Map showing the principle strain 1 values for the first four specimens . . . 122
a Specimen 1 . . . 122
b Specimen 2 . . . 122
c Specimen 3 . . . 122
d Specimen 4 . . . 122
e Specimen 5 . . . 122
C.2 Map showing the principle strain 1 values for the remaining three specimens 123
f Specimen 6 . . . 123
g Specimen 7 . . . 123
h Specimen 8 . . . 123
i Specimen 9 . . . 123
C.3 Map showing the principle strain 2 values for the first four specimens . . . 124
a Specimen 1 . . . 124
b Specimen 2 . . . 124
c Specimen 3 . . . 124
d Specimen 4 . . . 124
e Specimen 5 . . . 124
C.3 Map showing the principle strain 2 values for the first four specimens . . . 125
f Specimen 6 . . . 125

g Specimen 7 . . . 125
h Specimen 8 . . . 125
i Specimen 9 . . . 125
C.4 Greyscale values observed on Specimen 1 . . . 126
C.5 Greyscale values observed on Specimen 2 . . . 127
C.6 Greyscale values observed on Specimen 3 . . . 128
C.7 Greyscale values observed on Specimen 4 . . . 129
C.8 Greyscale values observed on Specimen 5 . . . 130
C.9 Greyscale values observed on Specimen 6 . . . 131
C.10 Greyscale values observed on Specimen 7 . . . 132
C.11 Greyscale values observed on Specimen 8 . . . 133
C.12 Greyscale values observed on Specimen 9 . . . 134

D.1 Experimental data curve-fitted using MCalibration for the first four specimens . . . 136
a Specimen 3 . . . 136
b Specimen 4 . . . 136
c Specimen 5 . . . 136
d Specimen 6 . . . 136
D.1 Experimental data curve-fitted using MCalibration for the remaining three specimens . . . 137
e Specimen 7 . . . 137
f Specimen 8 . . . 137
g Specimen 9 . . . 137

E.1 Images taken of Non-PFA fixed (top row) and PFA fixed (bottom row) samples . . . 140
E.2 Images showing tissue sectioned to 10 µm (top), 25 µm (middle) and 50 µm (bottom) thicknesses . . . 141

List of Tables

5.1 Description of colours used on samples 69

5.2 Isotropic index from bulge tester 71

5.3 Values obtained after curve fitting GOH model 80

5.4 Classification of anisotropy 80

5.5 Summary of ξ and κ values 81

B.1 Summary of sleeve heights associated with each arm 107

Abbreviations	Description
2D	2 Dimensional
3D	3 Dimensional
BISRU	Blast Impact and Survivability Research Unit
CFA	Cross Fiber Axis
CPL	Cross Polarising Line
DIC	Digital Image Correlation
FDM	Fused Deposition Modeling
FI model	Fully Integrated Distributed Fiber Model
GOH	Gasser-Ogden-Holzapfel
GP	General Polynomial
HSB	Hue-Saturation-Brightness
MFA	Mean Fiber Axis
OCT	Optimal Cutting Temperature
OD	Outer Diameter
PBT	Planar Biaxial Tensile
PFA	Paraformaldehyde
PLA	Polylactic Acid
RGB	Red-Green-Blue
ROI	Region Of Interest
SIS	Small Intestine Submucosa
SLA	Stereolithography
TBW	Tidal blue, flat black and linen white
TPCW	Tidal blue, blush pink, charcoal black and matt white
UCT	University of Cape Town
UV	Ultra-Violet
W	Matt white only

Chapter 1

Introduction

1.1 Background

Defining the mechanical properties of biological membrane tissue has always been a point of interest in the medical, cosmetology and biomechanical engineering fields. Examples of biological membrane tissues include skin, blood vessels, tendons and myocardium. In the medical field, better understanding of the mechanics of soft tissues helps improve the treatments of diseases or improves methods of tissue laceration and closure [1, 2]. Cosmetologists benefit by gaining insight on how to improve their product's emolliency, hydration and how they interact with skin [3, 4, 5]. Whilst in the biomechanical field better understanding of membrane tissue mechanics is vital in improving the design of medical devices and in the formulation of new computational models that can be used for simulations [6, 7].

Soft tissues are known to display complex mechanical behaviour because of their anisotropic, hyperelastic and non-linear stress-strain properties. Numerous invasive and non-invasive techniques have been developed to characterise the complex properties of biological membrane tissues. Of the invasive techniques, biaxial tensile testing best mimics the natural loading conditions for membrane tissues while providing appropriate data for developing constitutive models. The Blast Impact and Survivability Research Unit (BISRU) at the University of Cape Town (UCT) has been developing a biaxial tensile testing device capable of testing skin. BISRU's long term goal is to commission a locally available biaxial testing device capable of determining the mechanical properties of biological tissues. Past post-graduate students have designed and commissioned these devices which include a planar biaxial tensile tester by Caine [8] and inflation tester by Curry [9], where the commissioning trials were completed with samples made from silicon elastomers. Pons [10] furthered this research by developing a methodology that incorporated both devices to test a cruciform-shaped small intestinal tissue. The outcome of his research indicated

that a cruciform-shaped specimen was not optimal. This research builds on these testing platforms and seeks to implement one of the three most common gripping mechanisms used to attach a square test sample onto a planar biaxial tensile testing device.

1.2 Objectives

The primary objective of this project was to develop a clamping system that can be used to clamp membrane tissue on the existing biaxial tensile testing device at BISRU. The designed clamp shall cater for the specimen to be secured in a uniform and repeatable manner. If possible, the clamp shall allow for free contralateral motion of the sample under biaxial load. Lastly, stress-strain curves shall be generated, from which the parameters of a suitable constitutive model may be determined.

1.3 Scope

This research is restricted to the design and testing of a sample clamping system that will integrate with the existing biaxial tensile testing device at BISRU. All biological membrane samples used in this investigation were excised from lamb intestines, due to these being easily sourced as sausage casing and needing only food safety hygiene practice. As the experimental devices and methodology are still being refined, it was not prudent to pursue human tissue samples due to supply limitations and the increased bio-hazard concerns. The physiological condition of the tissue will be maintained during testing by suspending the sample in a saline bath. The introduction of additional physiological controls was beyond the scope of this project. Testing of samples is confined to the quasi-static domain, that is between $1\,\mu m\,s^{-1}$ to $100\,\mu m\,s^{-1}$, with the testing devices configured to a displacement control method.

This project included the use of constitutive material models to curve fit experimental data to extract model parameter. The implementation of these parameters in a finite element software to simulate test conditions was considered to fall outside the scope of this project.

1.4 Dissertation Outline

This dissertation consists of the following chapters:

- Chapter 2 presents a literature review on soft membrane tissues, their mechanical testing methodology and relevant constitutive material models developed to mimic their behaviour.

- Chapter 3 describes the design and fabrication of devices and tooling that were used in the experiments.
- Chapter 4 describes the experimental methodology, the specimen preparation process and the technique used to measure their thicknesses.
- Chapter 5 presents the results and their discussion as they became prevalent to the author.
- Chapter 6 gives the conclusions and recommendations based on the findings of this report.
- Appendix A documents the early concepts built and tested for this project.
- Appendix B describes the casting process and lists the sleeve heights used.
- Appendix C presents a comprehensive list of all experimental results.
- Appendix D shows the graphs generated from the curve-fitting exercise.
- Appendix E provides an investigation into a couple of aspects that were related to the Cryo-histology method.
- Appendix F presents sub-assembly drawings for the devices built in this project.

Chapter 2

Literature Review

2.1 Background on Biology Soft Tissue

Biological tissues are categorized into two groups: hard and soft tissues [11]. Hard tissues contain minerals, such as bones and teeth. Soft tissues do not contain minerals, which gives them their flexibility and soft mechanical properties [12]. Examples of soft tissue include tendons, blood vessels, ligaments, and skin. Soft tissues have complex composite structures that give them unique soft mechanical properties[12]. This section describes the structural composition and mechanical properties of soft tissues, with a specific emphasis on skin. A subsection will also be dedicated to a surrogate test tissue.

2.1.1 Structural Composition of Skin

Skin is most popularly described as a multi-layered complex thin membrane, comprised of three layers; the epidermis, dermis and hypodermis (also known as subcutaneous tissue), which are illustrated in Figure 2.1.3.

The outermost layer of skin is known as the epidermis, which is approximately 75 µm to 150 µm thick [14]. Within the epidermis there are four sub-layers, beginning from the surface there are the stratum corneum, stratum granulosum, stratum spinosum and stratum basale. The bottom three layers are collectively known as the viable epidermis layer. From this layer, cells migrate to the surface, whilst undergoing a process of mitosis and by the time they reach the stratum corneum they have turned into dead keratinocytes (non-viable cells). The stratum corneum is a 15 µm to 30 µm thick layer that also contains lipids, water and hydro-soluble matter [15].

Beneath the epidermis layer lies the dermis, where the bulk of the skin's load carrying capabilities are held. The dermis consists of a dense network of stiff collagen fibres that provide structural strength and elastin fibres that offer flexibility. These fibres are em-

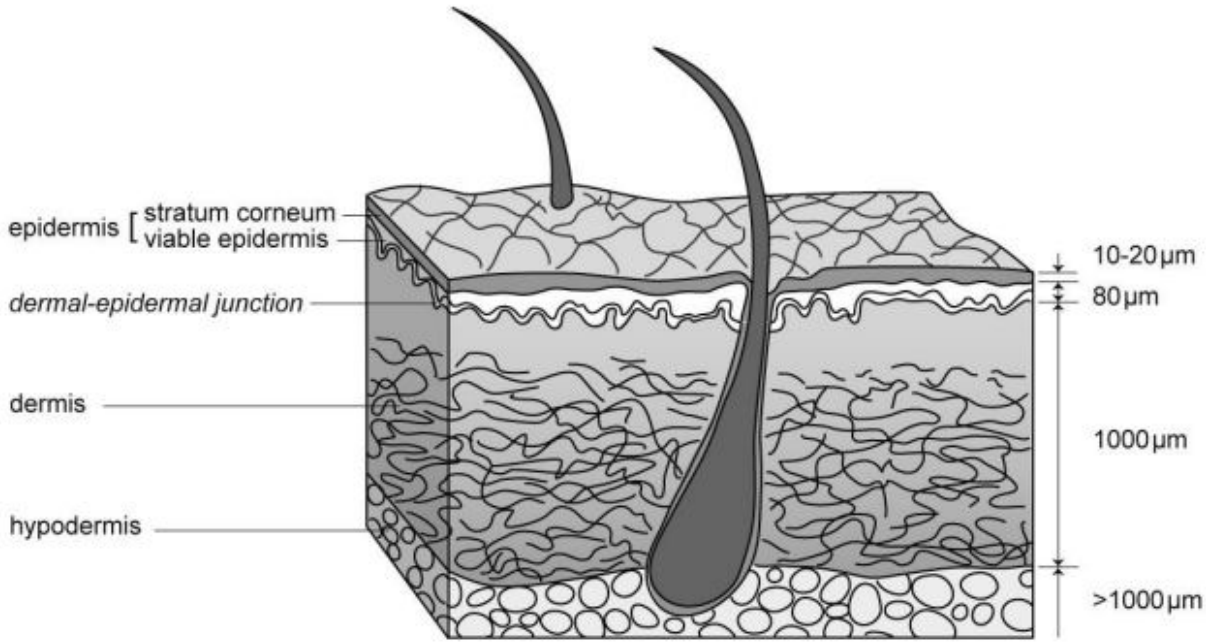

Figure 2.1 Illustration of the different layers of skin [13]

bedded in a matrix of hydrated proteoglycans [16]. The dermis may be broken into two divisions: the papillary and reticular dermis [15]. The papillary forms the top layer and occupies 10 % of the 1 µm to 4 µm thick dermis membrane [15]. Collagen fibres and elastin fibres are vertically orientated within the papillary layer to connect the epidermal layer to the dermis. The reticular layer has collagen fibres lying in the horizontal direction which when stretch can withstand extensions up to about 25 % [15].

The hypodermis (subcutaneous tissue) layer is found between the dermis and the fascia of the muscles [15], where it provides insulation, heat generation and flexibility enabling the skin above to move relative to the underlying fascia. Adipose tissue primarily builds this layer along with a network of collagen fibres. This layer is connected to the dermis via vascular networks and epidermal appendages (i.e hairs and nerve endings). The thickness of the layer is dependent on location on the body. Collagen fibres primarily bear most of the loads applied to soft tissues. They are a form of protein that exists in strands up to lengths of 280 nm [17]. A total of 28 different types of collagen fibres have been identified, where type I and II are the most common [18]. Networks of collagen fibres are formed through covalently bonded intra-molecular cross links provide soft tissue with structural strength [17].

Like collagen, elastic fibres are a protein found in membranes, that is load bearing but at much smaller loads. They exist as a network of long flexible molecules which when stretched may extend up to 2.5 times their length [17]. Elastin fibres have the unique ability to fully recover, even when stretched in excess of 100 % [19].

2.1.2 Mechanical Properties of Skin

The microstructure of skin allows for many variables to influence its mechanical response. Factors such as; concentration of fibres, arrangement of fibres, topography and hydration are some of the variables that have to be considered when studying skin mechanics [17].

Non-linear Stress Strain Relationship

Past studies have identified skin to observe a non-linear stress-strain relationship when subjected to tensile loading [17, 13]. Figure 2.2 displays the typical J-type stress-strain curve observed when skin experiences tensile loads [13].

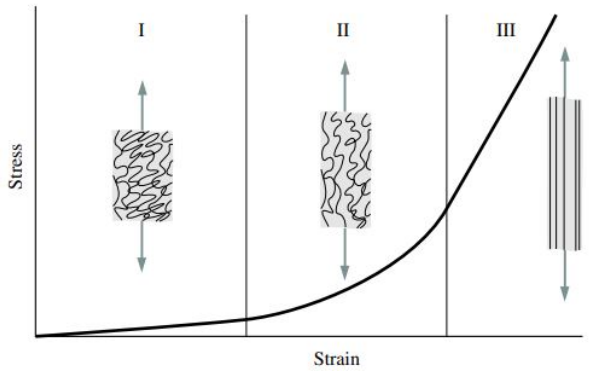

Figure 2.2 Schematic representation of a typical stress-strain curve for skin with collagen fibre morphology [17]

The curve is split into three phases. At the start of the curve, for a relatively small change in stress, large changes in strain are observed, which is similar to an elastomer like rubber. In this phase, elastin fibres are active in resisting the tensile while collagen fibres remain un-stretched and entangled. Holzapfel et al [17] approximated the elastic modulus of this region to be in the range of 0.1 MPa to 0.2 MPa.

In the second phase, the collagen fibres slowly begin to disentangle and elongate. These fibres align themselves in the load direction and subsequently resist the tensile loads. As the strain increases, the fibres further disentangle and reorient themselves at a much faster rate, thereby giving the tissue the ability to withstand increasingly higher loads. By the end of this phase, all the collagen fibres are no longer crimped and lie co-linear to the direction of the load.

Phase three is dominated by the behaviour of the straightened collagen fibres. During this phase, the tissue is at its stiffest and the stress-strain relation is observed to be linear. Within this stage the collagen fibres primarily carry all loads applied and any further extension is as a result of bond extension. Beyond this phase, the stiffness of skin decreases as a result of fibres slowly breaking in series [20].

Anisotropy

The anisotropic nature of skin can best be explained through the understanding of Langer lines and their relationship with collagen fibres. Langer lines are virtual lines that describes the principal direction of tension experienced on skin at a specific location on the human body. Langer observed this in 1861, when he punctured skin with a circular needle and noted that the wound formed took an elliptical shape, thereby showing that the skin is under pre-existing tension [21]. Langer proposed that the major axis of the elliptical cavity indicated the direction of maximum tension experienced at that location. A map illustrating these Langer lines on the human back is shown in Figure 2.3.

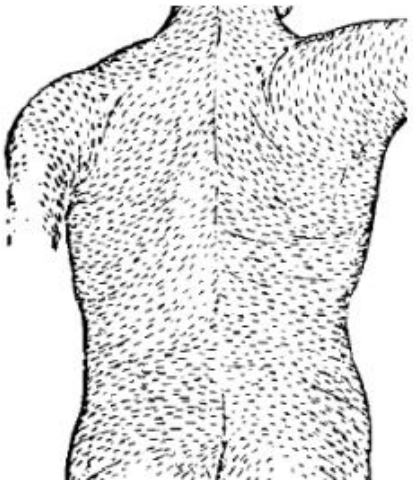

Figure 2.3 Langer lines mapped on the human body [21]

Tonge et al [22] investigated the anisotropic nature of skin using a bulge tester. Their study showed that collagen fibres are not evenly distributed at different directions but rather have a dominant fibre direction. Tonge et al [22] also reported that the dominant fibre direction lay parallel to the Langer Lines. As collagen fibres only provide significant resistance parallel to the fibres and they orient themselves predominantly in one direction, one expects skins to be anisotropic. Figure 2.4 depicts the stress-strain response along and perpendicular to the fibre direction [22].

Groves et al [23] tested murine skin sampled from the same anatomical location at three different orientations (0°, 45° and 90°) under uniaxial tension and also showed the stiffness parallel to the Langer lines were much higher than that perpendicular (see Figure 2.5). Similarly, Ni Anniadh et al [24] and Ottenio et al [25], tested human skin and showed that the orientation of their specimens affected the stress response measure.

Viscoelasticity

Skin is known to behave as a viscoelastic material, with characteristics such as strain rate sensitivity, creep, stress relaxation and hysteresis all been observed in experiments

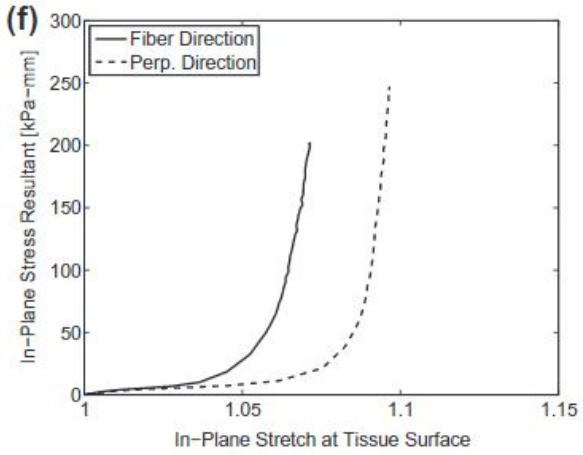

Figure 2.4 Stress-strain response captured along and perpendicular to the fibre direction [22]

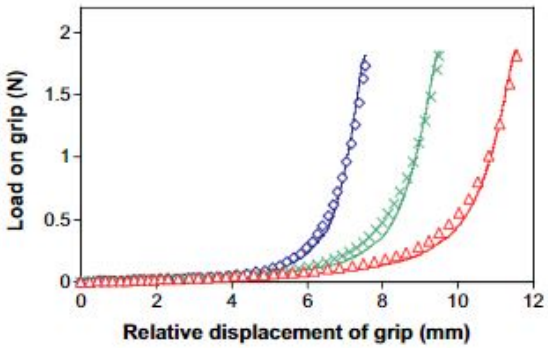

Figure 2.5 Stress-strain response captured at 0°(blue), 45°(green) and 90°(red) [23]

on skin. Haut et al [26] and Dombi et al [27], carried out uniaxial tests on murine skin at strain rates of $0.3\,s^{-1}$ to $60\,s^{-1}$ and found a prominent increase in ultimate tensile strength (UTS) with increasing strain rates. Shergold et al [28] found that the stiffness of pigskin increased when increasing strain rates from $0.004\,s^{-1}$ to $4000\,s^{-1}$. Similarly, Ottenio et al [25] reported human skin under uniaxial tension being sensitive to strain rates, showing an increase in UTS and elastic modulus with increasing strain rates. Figure 2.6 depicts the difference in stress-strain response at different strain rates [29].

Bose et al [30] investigated the mechanical response of collagen films (where samples were hydrated, submerged and dried) at different strain rates. Bose's [30] study showed that submerged and hydrated samples had a significant decrease mechanical strength and toughness, a much larger strain limit and different modulus when compared to the dried sample. The typical strain-rate sensitivity was also observed, but Bose et al [30] emphasized the importance of testing submerged samples to mimic physiological moisture conditions.

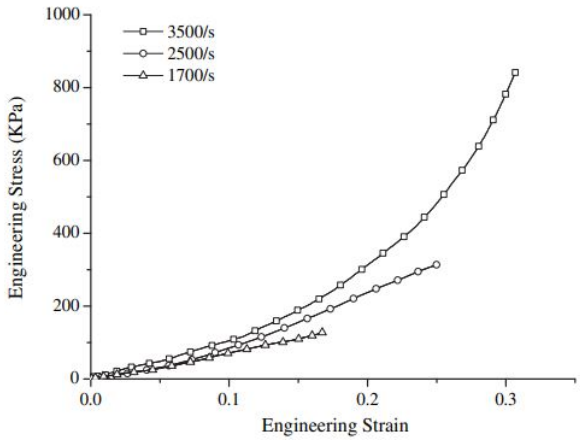

Figure 2.6 Uniaxial stress-strain curves on pig skin at different strain rates [29]

Creep tests performed by Khatyr et al [31], showed that when loading skin under a constant load that as time progressed, the tissue would deform to relieve the internal stresses. Figure 2.7 shows a creep curve observed by Agache et al [32], when pig skin was left under a uniform load for a period of time. The last characteristic of viscoelastic material is stress relaxation. Karimi et al [33] illustrated that under constant strain, the stress within skin decreases with time.

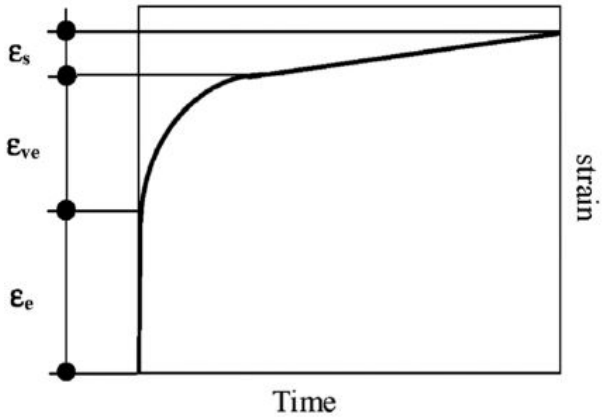

Figure 2.7 Illustration of a skin creep curved under a uniform load [32]

2.1.3 Surrogate Test Tissue

The scope of this research excluded the use of human skin for testing because of the bio-hazard concerns and supply limitations. Given that skin could not be used, a surrogate material had to be selected. Pons [10] introduced the use of small intestine submucosa (SIS) harvested from lamb as the biological surrogate to conduct experiments on. This decision was driven by the fact that the ovine SIS tissue was readily available at local abattoirs, ethically harvested and displayed similar structural characteristics to skin.

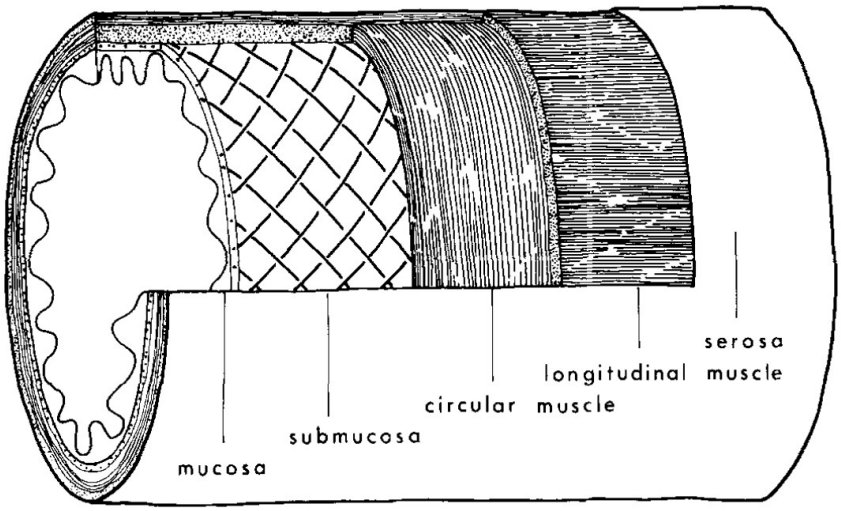

Figure 2.8 Structure of small intestine [34]

SIS tissue is one of the five sublayers that are present in the small intestines of mammals [34]. Figure 2.8 shows the location of the submucosa layer relative to the other four layers. Studies have shown that the SIS tissue consists mostly of collagen fibres, with elastic fibres also present to offer flexibility to the intestine walls [34, 35, 36]. Adipose tissue and blood vessels can also be found embedded in this layer [35]. Similar to the epidermis layer in skin, the submucosa holds most of the collagen fibres present in the small intestine and hence bears the majority of the loads that are imparted to the intestinal wall [34]. The submucosa is also characterised as an anisotropic material, with reports concluding that the collagen fibres exist in a lattice structure with two predominant directions. Gabella [34] described the arrangement as "two arrays of fibres running diagonally in a clockwise and an anticlockwise direction, and making an angle of 50°- 55° with the longitudinal axis of the intestine." Gabella [34] also reported that the anisotropic orientation would alter to cater for different loading conditions.

The submucosa tissue is sold at local abattoirs using the given name natural casing. The process of extracting this tissue to its packaging has been included for the author to appreciate the production cycle a said sample has experienced. The first process is to wash and scrape the harvested intestine to separate the submucosa from the other layers [35]. The blood is then removed by soaking the isolated tissue in ice water or brine [35]. Thereafter, it is packed with salt to extract the moisture and preserve the tissue before being put for sale.

2.2 Soft Tissue Mechanical Testing Methods

Mechanical testing methods of biological material may be split into two categories: in vivo and in vitro tests. In vivo refers to testing methods undertaken where the tissue is

in its natural form, on the living organism. In vitro tests refers to testing methods where the material has been excised from the donor. Both approaches have their advantages and disadvantages.

For the case of in vivo tests, its advantages lay in that the material does not require any preservation, and tests can consider both anatomical and physiological effects [37]. Its disadvantages are that the samples are limited to low strain rate tests, are not tested to failure and the mechanical response cannot be explicitly attributed to different sublayers [1].

In comparison, in vitro tests can conduct tests at high strain rates, are able to test skin to failure and are easier to model and evaluate the stress-strain relationship. An obvious disadvantage is that sample size is extremely limited unless the donor is deceased, or the sample was removed due to disease / disfigurement. Other disadvantages are attributed to the preservation and preparation of the excised sample. For example, factors such as material hydration and salinity do affect the tissues mechanical response as reported by Caro-Bretelle et al [38]. With regards to sample preparation, soft tissues are tedious to handle and axial loads may be imparted onto the specimen before testing which would affect its mechanical properties.

The mechanical properties of skin are experimentally tested using the following techniques; tensile tests, suction tests, indentation tests and torsion tests. In this section, emphasis will be placed on tensile testing methods as these are typically the simplest means of determining the material model parameters from in vitro testing, which is the focus of this project. As suction [4], indentation [39] and torsion [40] tests are typically in vivo methods and outside the scope of this project, the reader is pointed to Caine [8] for descriptions thereof.

2.2.1 Uniaxial Tensile Testing

This is the most common method of extracting material properties of metals, polymers, elastomers and their composites. Similar to testing engineering materials, the soft tissue has to be trimmed into dog-bone specimens, clamped onto the testing rig and loaded along one axis. For one to gauge the anisotropic properties separate specimens have to be prepared along different directions [41]. In recent years, digital image correlation (DIC) is used in conjunction to map the deformation and strain experienced. Uniaxial tests have been conducted on porcine, murine, bovine and human skin at both quasi-static and dynamic speeds [23, 24, 28, 41, 42, 43, 44]. Other soft tissues like arterial tissue and porcine bladder have also been tested using this method[45, 46].

Figure 2.9 shows an image of porcine skin being tested on an Instron machine. A main source of error when conducting uniaxial tests is material slippage at the clamped bound-

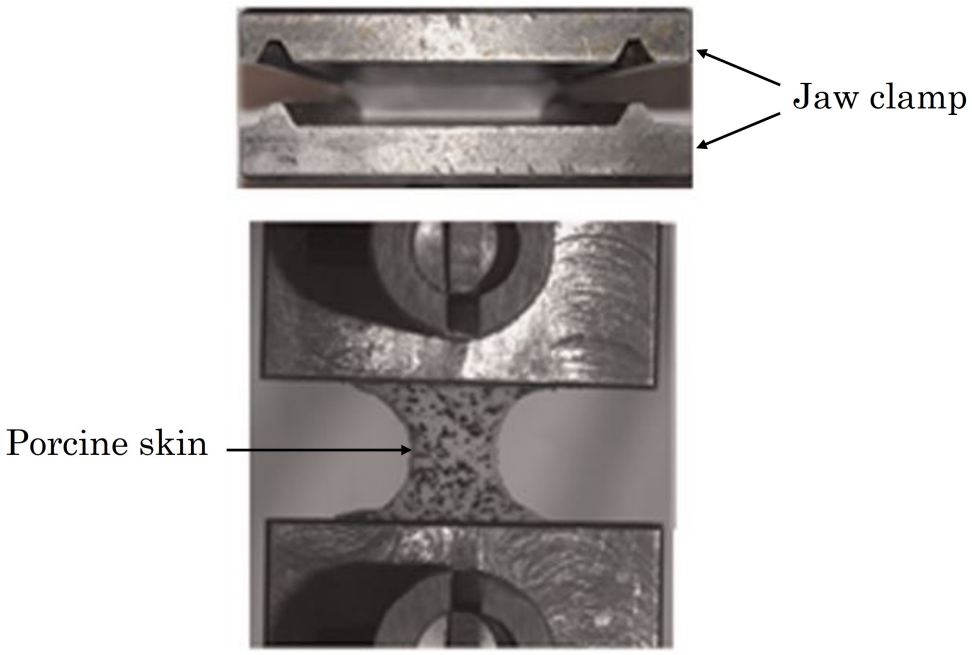

Figure 2.9 Photograph of porcine skin loaded on a uniaxial tensile test device with a jaw clamp [38]

aries. Different methods such as serrated jaws, freeze clamp and adding paper have been used to mitigate slippage [47, 48, 49].

2.2.2 Biaxial Tensile Testing

This methodology involves loading a sample in two perpendicular directions and recording its stress-strain response. Development of this technique began as the need to characterise anisotropic and orthotropic properties became more prevalent. Different designs and configurations have been developed to conduct a biaxial test. Two of the most successful biaxial testing methods are the planar biaxial tensile test and the bulge test.

Planar Biaxial Tensile Test

Planar biaxial testing is conducted by stretching a sample along two or more directions on the same plane. This method was first implemented by Lanir and Fung [50] to test the mechanical properties of rabbit skin. Figure 2.10 provides a sketch of a planar biaxial tensile testing rig [50].

The advantage of this method is that the specimen may be strained at different controlled rates along each axis which is useful for simulating different loading conditions in its natural state, and allows investigation of anisotropy at one location on a single specimen. Also since the sample being tested is under pure tension there are no bending effects to consider which would be an added layer of complexity. However, planar biaxial testing

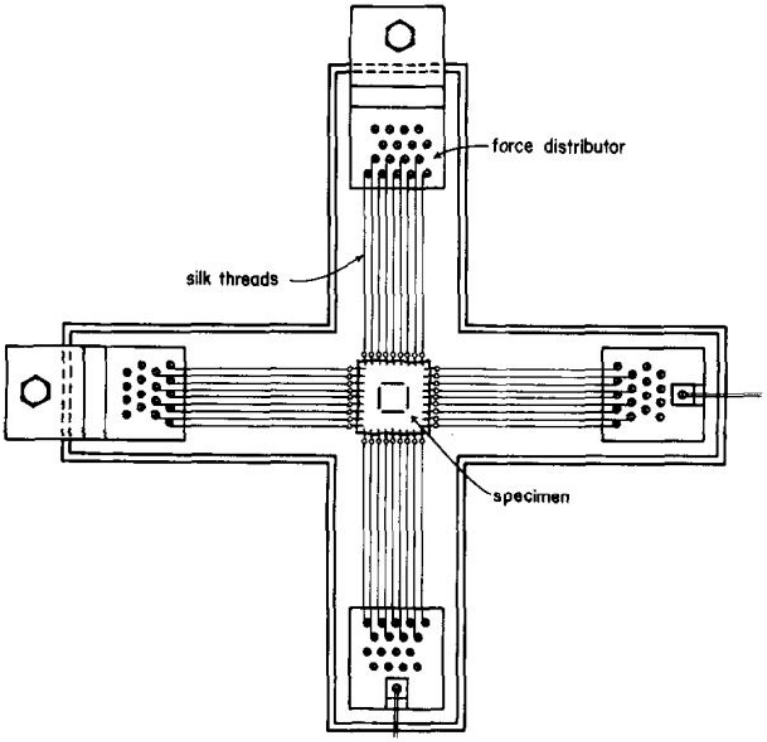

Figure 2.10 Illustration of a Planar biaxial tensile testing [50]

results are sensitive to sample geometry and clamping configuration. Avanzini et al [51] and Sun et al [52] have studied both these effects in depth and section 2.2.3 discusses this in more detail.

Bulge Test

Bulge testing involves applying a differential pressure to a sample that has been clamped between two disks with circular holes. The applied pressure inflates the sample into a dome from which principle stretches and stresses can be evaluated. The deformation experienced by the specimen during the test are recorded using instruments like DIC and edge detection. To calculate the principal stretches the following assumptions are made; the specimen deforms into a spherical dome [53], at its apex the sample is loaded equi-biaxially and that bending effects are negligible [54].

Figure 2.11 shows a model of an inflated dome where a, t, h, p denotes the radius of the hole, thickness of the sample, bulge height and differential pressure respectively. The stress and strain experienced by the membrane can then be evaluated using the following equations, defined by Sheng et al [55]:

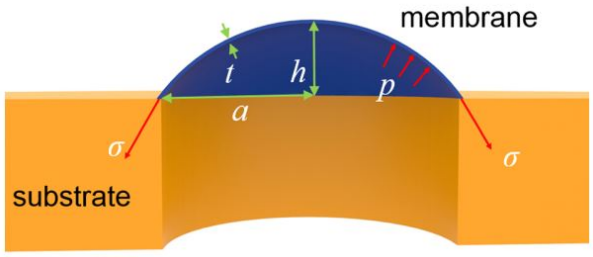

Figure 2.11 Illustration of bulge test method [55]

$$\sigma = \frac{p\,(a^2 + h^2)}{4ht} \tag{2.1}$$

$$\epsilon = \frac{a^2 + h^2}{2ah} \arcsin\left(\frac{2ah}{a^2 + h^2}\right) - 1 \tag{2.2}$$

$$when\ h << a \tag{2.3}$$

$$\sigma = \frac{pa^2}{4ht}, \epsilon = \frac{2h^2}{3a^2} \tag{2.4}$$

Bulge testers were designed to test isotropic material however in recent years testing methods have been improved to account for anisotropic properties. Tonge et al [56], tested human skin using a bulge tester at quasi-static strain rates to study the effects of preconditioning and humidity. In this study, the predominant fibre direction was identified from the deformed geometry and stresses were evaluated using ellipsoidal shells. It is worth noting that for thicker membranes bending stress can no longer be considered negligible and calculating the materials stress becomes increasingly difficult [56].

2.2.3 Gripping Methods

Normally when tensile testing materials it is generally assumed that St Venant's principle is obeyed under all gripping techniques used. This principle states that "gripping imposes local stresses at the grip-sample interface and the influence of these local stresses become negligible at some distance away from the grip" [57]. For homogeneous isotropic material Nielsen et al [58] showed that this principle holds within the central 25 % area of the sample. However for complex material such as soft tissues which are heterogeneous, anisotropic and non-linear, achieving a uniform stress state has been found to be non-trivial [57]. Prior investigations have observed that the choice of clamping mechanism and sample geometry affects the mechanical response of soft tissues under planar biaxial loads. Subsequently, different clamping configurations have been developed and the three most popular forms are clamping, suturing and rakes.

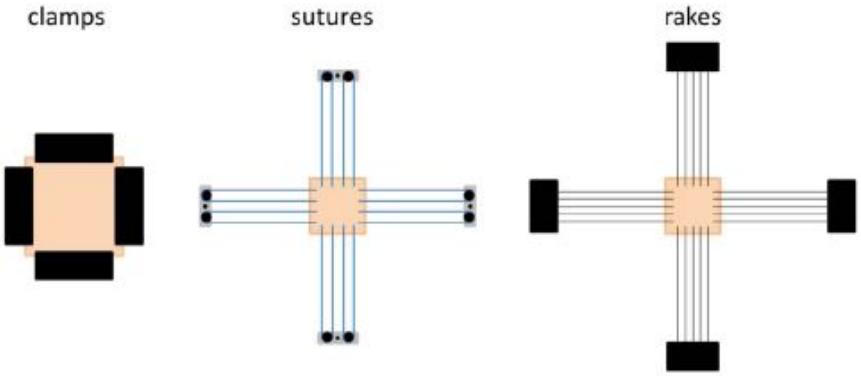

Figure 2.12 Illustration of different gripping methods [59]

Clamping

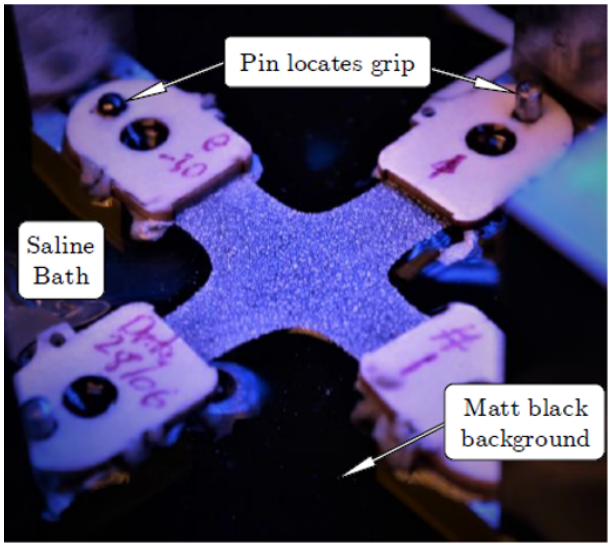

Figure 2.13 Photograph showing a clamped specimen [10]

Clamping entails securing a sample along each boundary by sandwiching it between two stiffer plates and applying a clamping pressure. Waldman et al [57] studied the effects of clamping, the result of which showed that clamping made the sample appear artificially stiffer. The same observation were corroborated by Sun et al [52] and Jacobs et al [60]. Sun et al [52] took a computational approach in his analysis of boundary effects and found out that the clamped configuration resulted in high-stress regions in the corners of the sample, as illustrated in Figure 2.14.

Having higher stress regions in the corners meant that less of the load was transmitted to the inner region, which led to lower strain measurements thereby giving a false representation of the stiffness of the material. In order to move away from the edge effects caused by a square clamped specimen, studies have been performed on cruciform shaped specimens [52, 57, 51]. Waldman et al [57] studied the behaviour of cruciform shaped specimens and

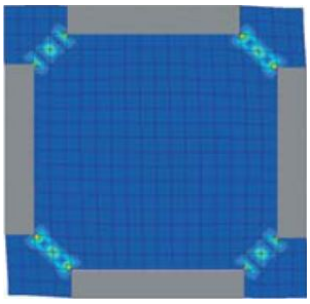

Figure 2.14 Von Mises stress and deformation of a clamped specimen [52]

noted the material response was dependent on the length of the arms, whereby shortened arms lead to "increased stiffness, reduced extensibility, reduced sample shearing and reduced rigid body rotation"[57]. Pons [10] also studied the behaviour of cruciform shaped specimens and reported that defining the cross-sectional area of a cruciform specimen for true stress calculations has uncertainties.

Suturing

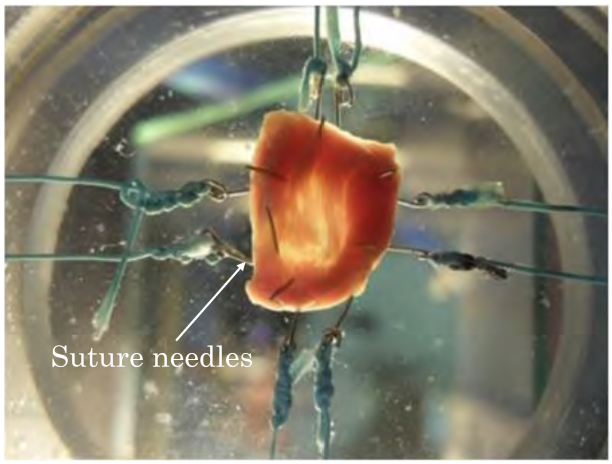

Figure 2.15 Photograph showing a sutured specimen [61]

Sutures may be defined as a thread that is used to secure itself to a material by means of forming loops or knots (see Figure 2.15). Past research has been conducted to understand the boundary effects that arise from suturing [57, 60, 62, 63]. Parameters such as number of sutures along each edge, spacing between each suture and effective sample area are some of the fields that are looked at. Unlike clamped samples, sutures transfer load at discrete points within the sample. This leads to highly localised stress concentrations at their point of incision [63]. The advantage of using sutures is that it allows for contra-lateral movement which leads to a more uniform distribution of the load throughout the specimen. Sun et al [52] study of boundary effects showed that sutured samples distributed majority of the load to the region of interest, leading to them concluding that sutures have a lower boundary effect than clamped samples.

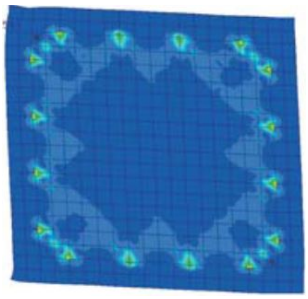

Figure 2.16 Von Mises stress and deformation of a sutured specimen [52]

Eilaghi et al [63] delved more into the effects on the number of sutures, spacing and size of the sample. Their research showed that the broader the spacing between each attachment, the more uniform the interior portion of the specimen is loaded. Eilaghi et al [63], emphasised that the size of the sample should be between 0.6 to 1 times the spacing lines to avoid the specimen from tearing when too small and from degrading the calculation of stress when it's too wide. Eilgahi [63] and Sun [52] proposed the use of five and four sutures per side respectively citing that further increases in the number of sutures does not significantly improve the uniformity of load distribution.

While suturing allows for better load distribution and doesn't impede contralateral deformation, it does require significant surgical skill and dexterity. Slight differences in location of the sutures lead to large changes in how the stress is distributed in the sample and are more prominent under biaxial loading [63]. Given that sutures are performed by hand, the ability to perform repeatable and uniform sutures at the right location are highly unlikely.

Rakes

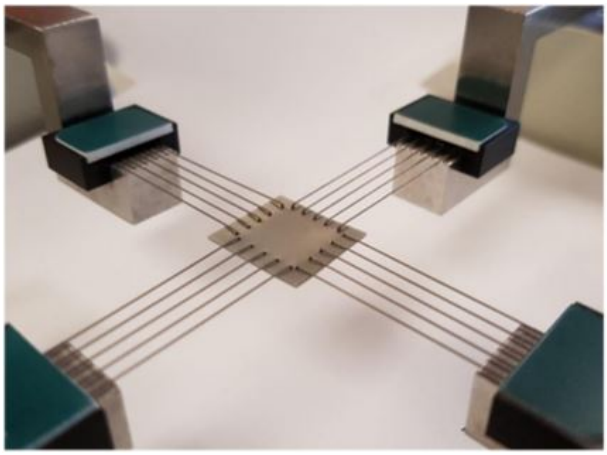

Figure 2.17 Illustration of CellScale BioTester rakes [64]

Rakes are thin metal arms with a sharp hook at the specimen end, as shown in Figure 2.17. Rakes are similar to sutures in that they apply localised point loads on the test

samples. However, rakes have non-negligible lateral bending stiffness in comparison to sutures, which increases restrain to contral lateral movement, which can be seen as negative feature. The advantage with implementing rakes are that they are more suited to repeated experimental work, given that they easier to attach and the hooks mounting position is fixed, which allows repeatability of boundary constraints [59]. This makes rakes the most practical form of clamping soft tissue on biaxial tensile test rigs, though the lateral bending stiffness does pose a challenge.

2.3 Preconditioning

Soft tissue by nature are viscoelastic due to the presence of water with dissolved compounds. Similar to other viscoelastic materials, soft tissues also display load-history dependent behaviour [42, 65]. Preconditioning is a technique used on a sample to remove this dependency. In the context of tensile testing, preconditioning is performed by subjecting the specimen to cyclic loading, where loads are kept within the elastic regime. During this process the elastin and collagen fibres realign themselves gradually into their natural state and adapt to the loading. The gain from applying this method are that it ensures repeatable results and that material is in its natural state. Figure 2.18 shows the stress strain curve of a porcine sample being cyclically loaded under uniaxial tension [65]. With each subsequent cycle, the loop bounded by the loading and unloading curve shifts to the right until it converges onto a single loop. Once this stage has been reached the material has been preconditioned.

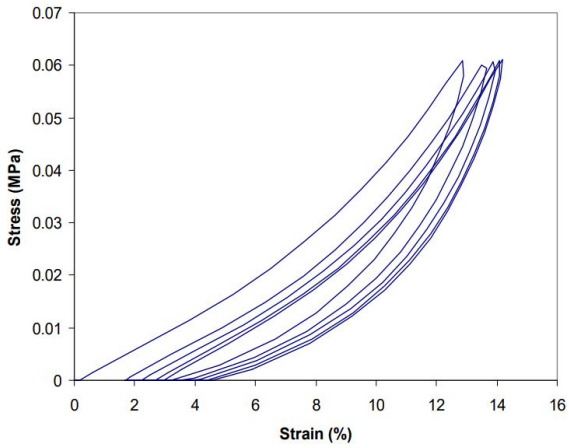

Figure 2.18 Preconditioning of a typical pig skin sample [65]

Although preconditioning is well accepted in this field of study, no standardised method have been established and subsequently different studies indicate different numbers of cyclic loadings required to fully precondition. Liu et al [65] reported that the preconditioning of porcine skin can be performed within 4 to 6 loading cycles for samples orientated parallel and 8 to 12 for those tested perpendicular to their Langer lines. Karimi et al [33]

similarly reported that murine skin is preconditioned after 10 cycles. Both of these authors were performing uniaxial tensile tests of their respective tissue. With regards to biaxial testing, Sack et al [66] reported that after two biaxial cyclic loadings no further changes in load-history was observed. It is interesting to note that Tonge's et al [22] observed that preconditioning skin before bulge testing had negligible effects. Tonge et al [22] reasons that because viscoelastic effects, fibre re-arrangement with loading and microstructural damages are all avoided there is no gain in preconditioning for a bulge test.

2.4 Constitutive Models of Skin

A good constitutive model should represent the non-linear, anisotropic and hyper-elastic behaviour of skin. Almost all existing skin models can be characterised into three main categories; phenomenological, structural and structurally-based phenomenological models [15].

Phenomenological models refer to constitutive models that picture skin as a single homogeneous material. The idea is to encapsulate the entire macroscopic behaviour of the material without considering the role of each substrate material [67]. Models such as Mooney-Rivlin and Fung fall into this category. Although simpler to model, the main disadvantage of these models is in their inability to produce constitutive parameters that have physical interpretation and hence offers no insight into the study of structural effects [15].

Some structural models are built by treating skin as a composite material, where the elastin fibres, collagen fibres and proteoglycans can be incorporated into the model explicitly [15]. For example, factors related to collagen fibres like orientation, degree of crimp, density and dispersion are found in these models [15]. The advantage this approach has over phenomenological models is that they are capable of accounting for thermal, mechanical and geometrical interactions [15]. However, this approach depends on accurate information for the stipulated parameters. Parameters such as fibre orientation and fibre dispersion are difficult to quantify experimentally which hinders the certainty of these models. Also, structural models are computationally more expensive than phenomenological models because they have more criteria to satisfy to achieve convergence.

Structurally-based phenomenological models are a hybrid of the two afore mentioned models. Lanir's model and Veronda and Westmann model are a good examples of these hybrid model. Included in the section below is a library of isotropic and anisotropic material models that have been used to describe biological materials. The variables and their meanings were taken from Limbert [15].

2.4.1 Isotropic Models

These models have been acknowledged as unsuitable for anisotropic materials such as skin, but have been included due to implementation in early literature and the more complex models build on these.

Mooney-Rivlin and Neo-Hookean Models

Both the Mooney-Rivlin and Neo-Hookean models were initially formulated to describe hyperelastic materials such as rubber. The Neo-Hookean model can be expressed as incompressible or compressible, where assuming $C_2 = 0$ enforces the incompressibility constraint. This incompressible Neo-Hookean model is defined as:

$$\psi = C_1 (I_1 - 3) \tag{2.5}$$

The Mooney-Rivlin model has its strain energy function composed of two invariants formed from the left Cauchy-Green deformation tensor $\mathbf{B}$ and is expressed as follows;

$$\psi = C_1 (I_1 - 3) - C_2 (I_2 - 3) + f (I_3) \tag{2.6}$$

Where C_1 and C_2 are material constants and I_i are the principal stretch invariants. Both models presented fail to produce the "J-type" stress-strain curve, which signifies increasing stiffness commonly exhibited by polymers [68].

Polynomial Strain Energy Models

The general strain energy function of this model is a simplification of the Mooney-Rivlin strain equation and is expressed as:

$$\psi = \left(\sum_{i+j=1}^{N} c_{ij} (I_1 - 3)^i (I_2 - 3)^j \right) - \frac{p}{2} (I_3 - 1) \tag{2.7}$$

where c_{ij} are material parameters, p is the hydrostatic pressure and I_i are the corresponding principal invariants. Polynomial strain energy models can cater for incompressible materials by assuming I_3 is 0. A further simplification can be made under certain con-

ditions whereby j can be taken as 0. Here the strain function is known as the reduced polymer formulation or Yeoh's material [69] and is defined as:

$$\psi = \left(\sum_{i=1}^{N} c_i (I_1 - 3)^i \right) - \frac{p}{2} (I_3 - 1) \tag{2.8}$$

Lapeer et al [70] conducted uniaxial tensile tests on female human abdominal skin where they used Yeoh's, Ogden and general polynomial (GP) models to curve fit their stress-strain data. The study showed that there are stability issues with the GP model which were caused by the chosen values for the constitutive parameters. Lapeer et al [70] implemented Yeoh's model, from first-order to the sixth-order, and found it to be unconditionally stable for all positive constitutive parameters. Limber et al [15] recommended that polynomial strain energy models should not be used for skin modelling because of their material stability issues.

Ogden Model

First developed in 1972 by Ogden [71], this model aimed to represent the non-linear, isotropic and hyper-elastic nature of soft tissues and polymers. Its strain function is based on principal stretches λ_i of the deformation gradient $\mathbf{F}$, in a three-dimensional space.

$$\psi = \sum_{i=1}^{n} 2 \frac{\mu_i}{\alpha_i^2} (\lambda_1^{\alpha_i} + \lambda_2^{\alpha_i} + \lambda_3^{\alpha_i} - 3) \tag{2.9}$$

where α_i are dimensional parameters, μ_i is a parameter related to shear moduli and n is the order of the Ogden series. First-order, second-order and third-order Ogden models have been used to curve fit uni-axial stress-strain data performed on porcine, murine and human skin[28, 29, 43]. The study carried out by Lyon et al [43] attempted to represent the fibres by adding on a volumetric component ($U(J)$) and was based of the bulk modulus.

$$U(J) = \frac{\xi}{\alpha\beta} \left(e^{\alpha (I_n - 1)^\beta} - 1 \right) \tag{2.10}$$

$$\psi = \sum_{i=1}^{n} 2 \frac{\mu_i}{\alpha_i^2} (\lambda_1^{\alpha_i} + \lambda_2^{\alpha_i} + \lambda_3^{\alpha_i} - 3) + U(J) \tag{2.11}$$

Referring to 2.10, ξ is the measure of the fibre modulus and I_n is the fibre stretch squared and β is a material constant. Lyon et al [43] used both a first-order Ogden model and an exponential power-law model and found that both correlated well with uniaxial test data, but not for biaxial test data. Although managing to indicate the change in stiffness across the two directions, Lyon did acknowledge that a more complex model is necessary [43].

2.4.2 Anisotropic Models

More recent models have started incorporating functions to display the anisotropic behaviour of skin, some of which are listed below:

Fung's Model

Fung [72] built this model to represent hyperelastic material using a pseudo strain potential function ($\rho_0 W$) and is described as follows:

$$\rho_0 W = f(\alpha, e) + ce^{F(\alpha,e)} \tag{2.12}$$

where ρ, W and c represent the material's density, strain energy per unit mass and a material constant respectively. $F(\alpha, e)$ and $f(\alpha, e)$ can be expanded to:

$$f(\alpha, e) = \alpha_1 {e_{11}}^2 + \alpha_2 {e_{22}}^2 + \alpha_3 {e_{12}}^2 + 2\alpha_4 e_{11} e_{22} \tag{2.13}$$

$$F(\alpha, e) = \alpha_1 {e_{11}}^2 + \alpha_2 {e_{22}}^2 + \alpha_3 {e_{12}}^2 + 2\alpha_4 e_1 e_2 + \gamma_1 {e_1}^3 + \gamma_2 {e_2}^3 + \gamma_4 {e_1}^2 e_2 + \gamma_5 e_1 {e_2}^2 \tag{2.14}$$

where α_i and γ_j are constants. Taking the partial derivative of strain potential function with respect to Green's strain tensor (e_{ij}) will give an expression that describes the materials stress. Sun et al [73] implemented this model to curve fit and simulate bovine tissue being loaded equi-biaxially and Tonge et al [22] did the same on rabbit skin. In both studies anisotropic behaviour was displayed in their stress-strain curves.

Lanir's Model

In 1983, Lanir developed a constitutive model which described skin as a composite material built of embedded fibres in a mesh of an isotropic material [74]. Lanir's total strain energy function was defined as:

$$\psi = (1 - V_c - V_e)\frac{\mu}{2}(I_1 - 3) + \sum_k V_k \sum_\theta R_k(\theta)\frac{K_k}{2}(\lambda - 1)^2 \tag{2.15}$$

where V_k, K_k and R_k are the volume fraction, fibre stiffness and the fibre orientation probability density function of each fibrous phase k be it collagen (c) or elastin (e). With this model collagen and elastin fibres are assumed to be linear elastic and cannot resist compression along their axis. The collagen fibres are also accounted for their degree of crimping, a factor described by the direction (θ) and a Gaussian distribution. This Gaussian function quantifies the different amounts of stretching required to uncrimp the fibres present.

Veronda and Westmann Model

Veronda and Westmann formulated a phenomenological-structural model, which classes the fibres in soft tissue into three categories and explicitly incorporates them in their strain energy function [67]. This strain energy function is described as follows:

$$\psi = C_1\left[e^{C_2(I_1-3)} - 1\right] - \frac{C_1 C_2}{2}(I_2 - 3) + f(I_3) \tag{2.16}$$

where C_1 and C_2 are material parameters, and $f(I_3)$ characterises the degree of incompressibility and volumetric deformation [15].

Weiss Model

Weiss' model is a transversely isotropic, hyperelastic and incompressible model that has a strain energy function as follows:

$$\psi = F_1(I_1, I_2) + F_2(I_4) + F_3(I_1, I_2, I_4) \tag{2.17}$$

F_1 marks the material response of the isotropic matrix, F_2 shows the contribution from the collagen fibres and F_3 describes the matrix-fibre interaction [75]. Groves et al [23] combined both this model and the Veronda-Westmann model to produce an anisotropic material model, with the intention to describe the behaviour of human and murine skin. This anisotropic model was described as follows:

$$\psi = C_1 \left[e^{C_2(I_1-3)} - 1\right] - \frac{C_1 C_2}{2}(I_2 - 3) + F_2(\lambda) + \frac{K}{2}\left[ln(J)\right]^2 \tag{2.18}$$

$$\lambda \frac{\partial F_2}{\partial \lambda} = \begin{cases} 0 & \text{if } \lambda < 1 \\ C_3\left(e^{C_4(\lambda-1)} - 1\right) & \text{if } 1 < \lambda < \lambda_m \\ C_5 + C_6\lambda, & \text{if } \lambda \geq \lambda_m \end{cases} \tag{2.19}$$

where C_1 and C_2 are material parameters, C_3 is a scaling factor that affects the exponential stresses, C_4 factors the rate of uncrimping of fibres and C_5 is the elastic modulus of the straightened fibres [23]. C_5 was characterised as function of C_3 and C_4 to maintain continuity of the strain energy function and is described as follows:

$$C_5 = C_3 C_4 \lambda \left(e^{C_4(\lambda-1)}\right) \tag{2.20}$$

Fibre-distribution Models

Fibre distribution models all work under the assumption that collagen fibres are distributed in an isotropic and incompressible mass consisting of elastin and proteoglycans. The collagen fibres are orientated in all directions, but with the added feature that accounts for the dominant fibre direction. The general strain energy function is expressed as a sum of a Neo-Hookean model and an anisotropic function.

$$\psi = C_1(I_1 - 3) - \frac{C_2}{2}(I_3 - 1) + \psi_{aniso} \tag{2.21}$$

where C_1 and C_2 are material parameters, I_i denotes the principal invariants of deformation and ψ_{aniso} represents the respective anisotropic fibre model. The fully integrated distributed fibre model, the 3-D Gasser-Ogden-Holzapfel (GOH) model and the 2-D GOH model are discussed below.

Fully integrated distributed fibre model (FI model) consists of one governing equation and three constitutive equations and can be described as follows:

$$\psi_{aniso} = \int_{-\pi}^{\pi} \psi_{fibre}\left(\lambda\left(\theta\right)\right)\rho\left(\theta\right)d\theta \tag{2.22}$$

$$\psi_{fibre}\left(\lambda\left(\theta\right)\right) = \frac{k_1}{2k_2}\left(e^{k_2\left(\lambda^2(\theta)-1\right)^2} - 1\right) \tag{2.23}$$

$$\rho\left(\theta\right) = \frac{e^{b\cos(2\theta)}}{2\pi I_0\left(b\right)} \tag{2.24}$$

$$\lambda^2\left(\theta\right) = {\lambda_f}^2\cos^2\theta + {\lambda_p}^2\sin^2\theta \tag{2.25}$$

The governing equation is an integral across a 2-D domain that relates the fibre distribution (2.24) to the respective stiffening response of the fibres (2.23) [76]. A semi-circular von Mises distribution function is used to describe the spread of the fibres, where θ is the angle of the fibre relative to the dominant fibre direction [76]. In Equation 2.24, b may be thought of as a weighting factor used to quantify the percentage of fibres aligned along the dominant fibre axes. I_0 is a modified Bessel function.

Equation 2.23 adds the anisotropic stiffening response of the fibres, where k_1, k_2 and λ^2 describe the tensile properties, degree of non-linearity and relative fibre stretch respectively. Note that λ_f and λ_p are the principal stretches parallel and perpendicular to the dominant fibre direction.

3-D GOH model implements a normalised von-Mises fibre distribution function (D(θ)) spread across a unit sphere and is expressed as follows:

$$D\left(\theta\right) = \frac{2\rho\left(\theta\right)}{\int_0^{\pi}\rho\left(\theta\right)\sin\theta d\theta} \tag{2.26}$$

where θ is the angle relative to the dominant fibre direction [77, 78]. Using this distribution function, a generalised structured tensor **A** is formed (see Equation 2.27) which emulates the anisotropic stress response and the dominant fibre direction [78].

$$A = \kappa I + \left(1 - 3\kappa\right)e_f \otimes e_f \tag{2.27}$$

$$\kappa = \frac{1}{4}\int_0^{\pi} D\left(\theta\right)\sin^3\theta d\theta \tag{2.28}$$

κ is a dispersion parameter used to define the ratio of anisotropic to isotropic contributions to the fibre distribution [78]. The anisotropic strain function (see Equation 2.30), proposed by Holzapfel et al [77], can now be expressed in terms of a pseudo-invariant (I_α) and κ:

$$I_\alpha = \kappa I_1 + (1 - 3\kappa) {\lambda_f}^2 \tag{2.29}$$

$$\psi_{aniso} = \frac{k_1}{2k_2} \left(e^{k_2 (I_\alpha - 1)^2} - 1 \right) \tag{2.30}$$

2-D GOH model works by assuming the fibres are limited to 2D plane, but distributed therein. The equations used to describe this model are one layer of complexity less than the 3D-GOH model and is defined as follows:

$$A = \kappa_{2D} \left(e_f \otimes e_f + e_p \otimes e_p \right) + (1 - 2\kappa_{2D}) \, e_f \otimes e_f \tag{2.31}$$

$$\kappa_{2D} = \frac{1}{2\pi} \int_{-\pi}^{\pi} \rho \left(\theta \right) \sin^2 \theta d\theta \tag{2.32}$$

$$I_\alpha = \kappa_{2D} {\lambda_p}^2 + (1 - 2\kappa_{2D}) {\lambda_f}^2 \tag{2.33}$$

Tonge et al [76] used these three models to simulate a planar anisotropic tissue under conditions experienced on a bulge tester. Tonge et al [76] concluded that the FI model performed the best in reproducing the anisotropy measured by the bulge test, whereas the GOH models could not capture the same extent of anisotropy.

2.5 Digital Image Correlation

2.5.1 Background

Digital image correlation (DIC) is a non-contact optical tool that is used for near full-field surface displacement measurements. The digital cameras capture images of the deforming sample at a set frequency, which are then analysed to track the deformation of the sample. This form of displacement measurement can be applied in both 2D and 3D fields, with multiple cameras or views needed for out of plane measurements. Figure 2.19 provides a representation of the arrangement of 3D-DIC apparatus positioned on a bulge tester.

For the DIC algorithm to produce full field measurements, the sample surface must have markings that can uniquely identify its location, which is achieved with random speckling. A good speckle marking will produce a random speckle pattern with high contrasts and high-frequency variations in light intensity when illuminated by a light source [79]. Due

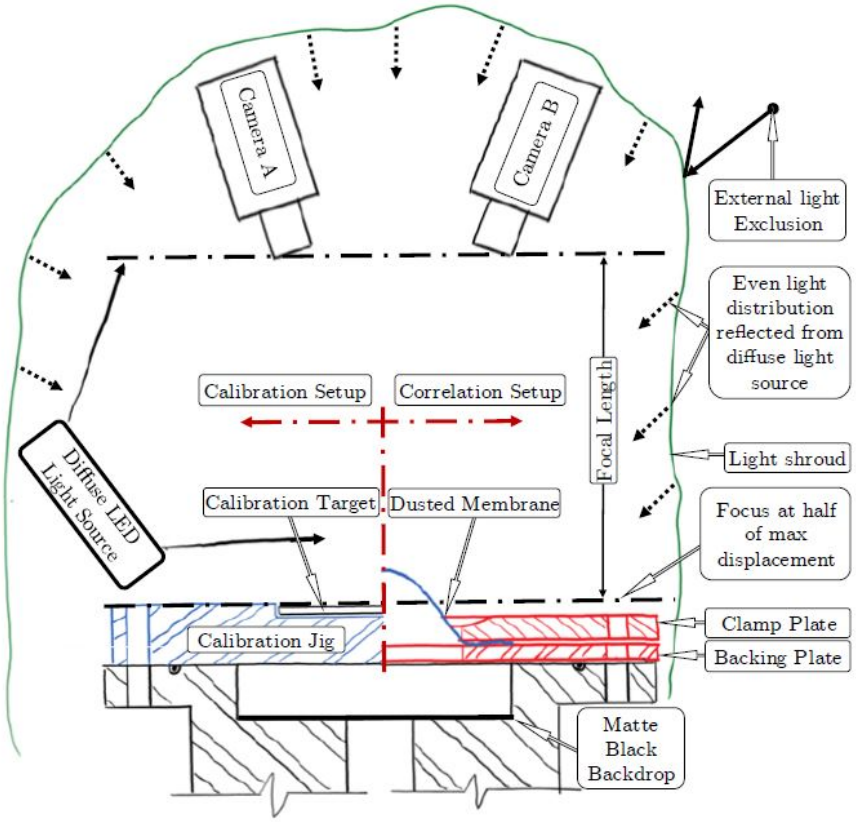

Figure 2.19 Illustration of DIC setup to capture sample inflation on a bulge tester [10]

to the random nature of the speckle, the light distribution at each point on the surface is unique. A greyscale intensity distribution function is then used to quantify these unique light distributions. This feature provides the ability to track the motion of a single point by locating its signature light distribution value through each subsequent image taken [79]. Hence, on the global scale, a full field displacement measurement of the sample can thus be produced at high accuracies. This contrasts DIC to older methods using repetitive grid markers, which are non-unique and inherently limit spatial resolution.

2.5.2 Speckling

A speckled sample that produces good results must consist of two main attributes which are good speckle size and broad grey-scale variation [79]. The choice of speckling method is always informed by the type of material that the sample is made from.

Looking specifically at biological tissues, the most effective method to create a good, speckled pattern has been identified as the spray method [10, 79, 80]. This method entails the use of an aerosol spray to discharge a mist of paint above the sample and then allow this mist to settle on it. Figure 2.20 provides a schematic of the spray method.

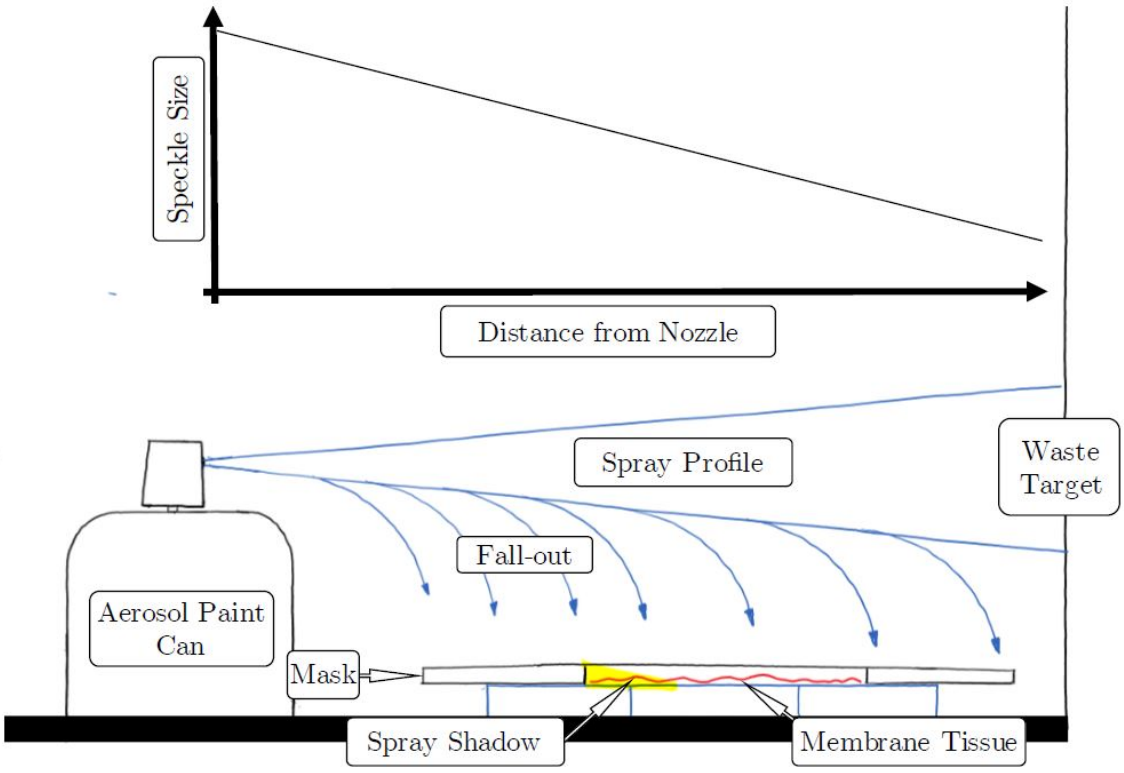

Figure 2.20 Schematic showing spray method to speckle a sample [10]

The size of the speckles can be controlled by adjusting the distance between the aerosol can and the sample. For larger speckle sizes the sample should be moved closer to the can and vice versa. Pons [10] study used multiple discharges of paint to achieve a fine high-density speckled pattern and also rotated the specimen to mitigate shadows that were produced because of using a masked specimen.

2.5.3 Optics and Lighting

Optics and lighting are important fields to consider when using DIC. With regards to lighting, factors such as "overexposure, underexposure, blurring, temporal light artifacts and contrasts" all have the effect of diminishing the greyscale variation [10]. A decrease in the greyscale distribution would result in issues with identifying correlation points because the unique light distribution would be harder to discern among similarly lit points. Overexposure, due to excessive lighting and reflection, results in camera pixels identifying with the same, non-distinct, maximum value. As the greyscale distribution is no longer distinct, overexposed regions can no longer be tracked by the DIC algorithm, leading to gaps in the full field displacement data.

When using DIC to document the inflation of tissue under bulge testing, additional factors need to be considered. Documenting the inflated membrane requires the DIC to

capture 3D measurements, which requires an additional camera. Now not only does the illumination need to expose the sample surface adequately, but the light sources must also be positioned in such a way that both cameras "see" similarly bright images. Failure to do so results in different greyscale signatures for the same region viewed by different cameras. This prevents cross-correlation of the same target feature the respective images, resulting in failure to map 3D deformation. Regarding the setup of the optics, care must be taken to ensure that the sample remains in focus through its inflation.

In this research, the process adopted by Pons [10] will be used to assemble, calibrate, capture and process the data using DIC. This decision was made because the same equipment shall be used to test and record strain measurements of the biological sample.

Chapter 3

Design of Experimental Apparatus

This chapter provides an insight into the design process taken to build a rake-based clamping system that can be used to hold membrane tissues on a biaxial tensile test device. Along with the design of the rakes, this chapter also goes on to discuss the mechanical tooling and jigs that were constructed to fabricate the rakes, mount the rakes onto the specimens and secure the hooked sample onto the testing device. The existing biaxial tensile and bulge testing devices are briefly described to identify design constraints and limitations.

3.1 Overview of Current Devices

Blast Impact and Survivability Research Unit (BISRU) over the past few years has dedicated resources to the development of their biaxial testing device capable of testing soft tissue material. As a result, they are now in possession of their own in-house bulge testing device and planar biaxial tensile (PBT) testing device. Recently a new testing methodology was developed at BISRU that combined the use of both these devices to carry out a single biaxial tensile test [10]. In this method the bulge testing device was first used to identify the orientation of maximum stiffness (Mean Fibre Axis) and then the sample was transferred to the PBT machine aligned such that the MFA lay along one of the PBT axes.

3.1.1 Bulge Testing Device

An image of the bulge testing device designed by Curry [9] is given in Figure 3.1. This device consisted of an inflation chamber and a fluid pump connected via a high-pressure pipe. The pump was built from a 60 mL syringe, driven by a translating carriage powered using a stepper motor producing an inflation rate from $0.05\,\mathrm{mL\,s^{-1}}$ to $5\,\mathrm{mL\,s^{-1}}$. The inflation chamber was designed to hold a sample with diameters ranging from 10 mm to

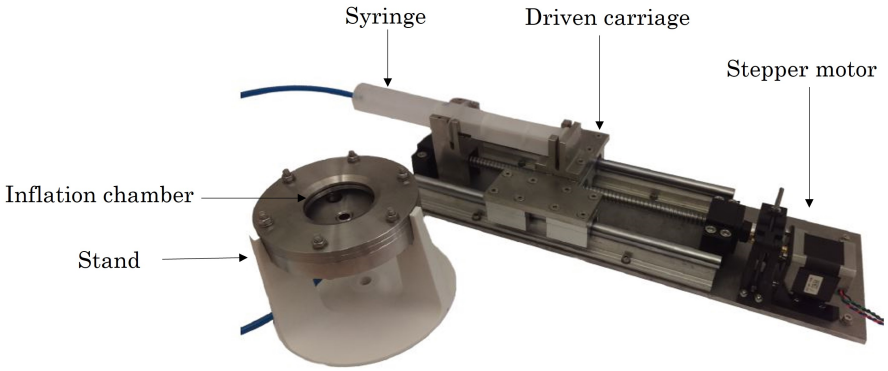

Figure 3.1 Photograph of bulge testing device [9]

50 mm. Within the inflation chamber, a 100 mbar pressure transducer was used to record the pressure history during testing. Microcontrollers are linked with this device to control the electrical instrumentations such as limit switches, Digital Image Correlation (DIC) trigger and stepper motor as well as storing data from the sensors. The inflation chamber

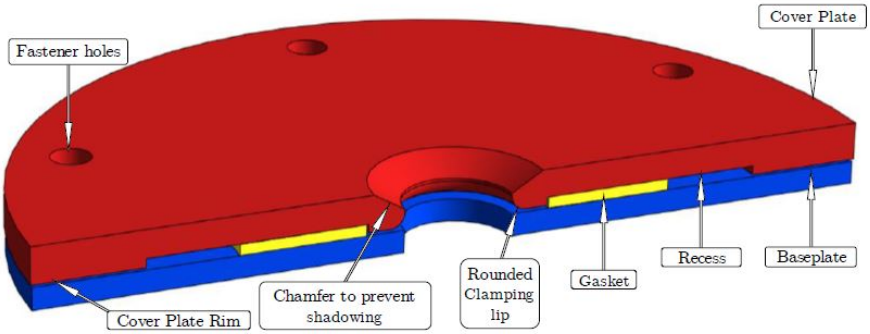

Figure 3.2 Sub-assembly of clamping configuration [10]

was modified by Pons [10], to be more suitable for membrane tissue. The modifications included adding a recess, including a rubber gasket and protruding lip in the upper clamping surface (refer to Figure 3.2). These changes allowed the membrane tissue to be held more securely onto the base plate. For this research, the bulge tester was used to identify the mean fibre axis (MFA) and cross fibre axis (CFA) so that the specimen may be cut in the correct orientation.

3.1.2 Planar Biaxial Tensile Testing Device

Figure 3.3 shows the planar biaxial tensile (PBT) machine design built by Caine [8]. It features four arms connected in pairs, where each pair had a single stepper motor that translates the two arms in opposite directions at the same speed. These stepper motors were run in open-loop, displacement control. Mounted on this device were two load cells

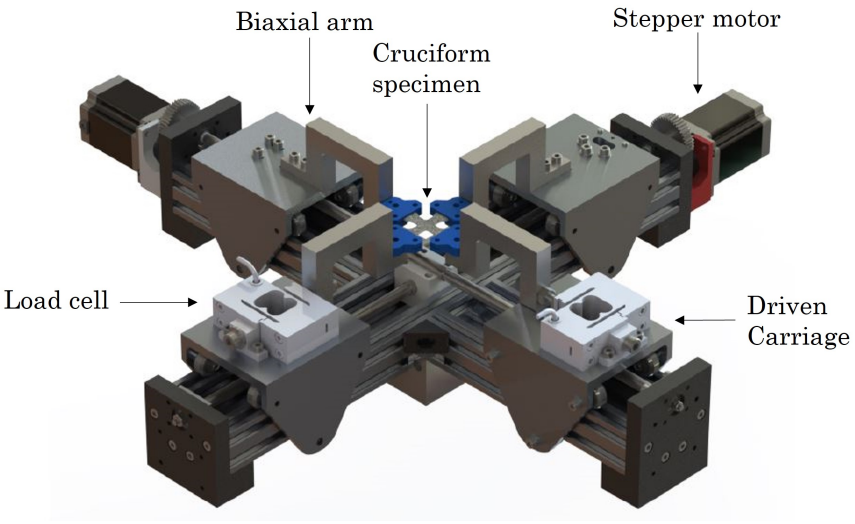

Figure 3.3 The rendered image of biaxial tensile testing machine [8]

capable of recording up to 50 N of axial load. Each of them was mounted as shown in Figure 3.3.

Although during commissioning the device was tested using an elastomeric sample, Caine [8] designed the device bearing in mind that it should also cater for soft membrane tissue. Subsequently, design choices were made such that various gripping mechanisms could be seated on it. The arm's unusual "N" type shape was chosen to accommodate a saline bath if deemed required. Similar to the bulge tester, this device also has a control box controlling the instrumentation, storing the load cell data and an interface to programme the motion of the arms. It also required DIC to capture the deformation of the specimen during testing and these cameras are positioned overlooking the specimen.

3.2 Selection of Clamping Configuration

The decision on the clamping technique used was chosen based on the findings in section 2.2.3. The fully clamped technique was discarded because of the reports stating that the clamped boundary conditions artificially stiffens the clamped sample [52, 57, 60]. Furthermore, Pons [10], who worked previously on this project, had already conducted PBT tests on clamped Small Intestine Submucosa (SIS) tissue and recommended the use of a different gripping method to be used. Section 2.2.3, showed that rakes were the most practical form of clamping soft tissue, but also showed that sutures best performed in transmitting the load uniformly across the specimen because of the allowance of contra-lateral motion. Based on this, the decision was made that a novel rake gripping system would be designed, that could match the practicality of the rakes whilst also cater for contra-lateral motion of the sample under deformation.

3.3 Design Constraints and Specification

From the outset of this project, any devices built were to be designed such that they would integrate with the existing biaxial and bulge testing device. This meant that the design had to abide by these constraints whilst still matching its design requirements. The list below illustrates the design constraints and specifications:

1. Design Constraints
    - Sample geometry shall be excised from a disk with an aperture of 35 mm in diameter as this is the largest inflation aperture diameter usable with the available SIS tissue.
    - Mounted sample and arms shall fit within the boundaries of carriage walls of the PBT machine built by Caine [8].
2. Design Specifications
    - Rakes shall allow contra-lateral motion with minimum restraint.
    - Rakes shall attach in a uniform, repeatable manner.
    - Specimen mounted on rakes shall be easy to transport to biaxial test device, without deforming specimen during transport.
    - Specimen shall have a square geometry.
    - Design of all equipment shall be less than 10 kg, for movement without special lifting equipment.

3.4 Design of Specimen Geometry

The overall design of the rakes and their auxiliary components all hinged on the size and dimension of the sample to be tested. Features such as the number of mounting hooks, location of hooks and sample boundary all informed the design choices of the other parts associated with the design. Therefore, it was necessary to size the sample before detailed design of the other components. Four factors were considered when sizing the specimen which were: sample shape, location of hooks, number of hooks and cutting allowance.

Regarding the shape of the sample, a square-shaped specimen was chosen because previous work on rake based systems used square specimens in their research. When selecting the size of the specimen the dimensions of the bulge testers' sample plate had to be considered. Given that its aperture was 35 mm in diameter meant that the square sample and any cutting apparatus had to fit inside a 35 mm diameter circle.

The number of hooks to be used per side was chosen to be four. This decision was informed by the study performed by Sun et al [52], who proposed four to be the ideal number of

hooks per side that should be used on a specimen. The location of the hooks was made at the author's discretion, but with the emphasis that the sets of hooks on one side of the specimen were parallel to the other set and that each pair of hooks on either side were co-linear with each other. Figure 3.4 provides a sketch detailing the final specification of the sample that is to be prepared from the bulge testes sample plate

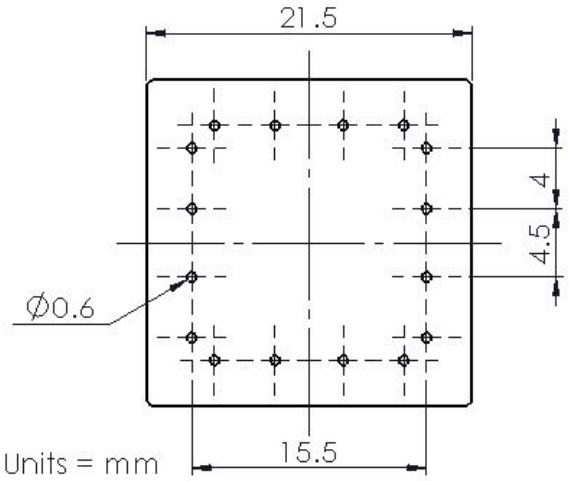

Figure 3.4 Illustration of sample size and geometry

3.5 Rake Design

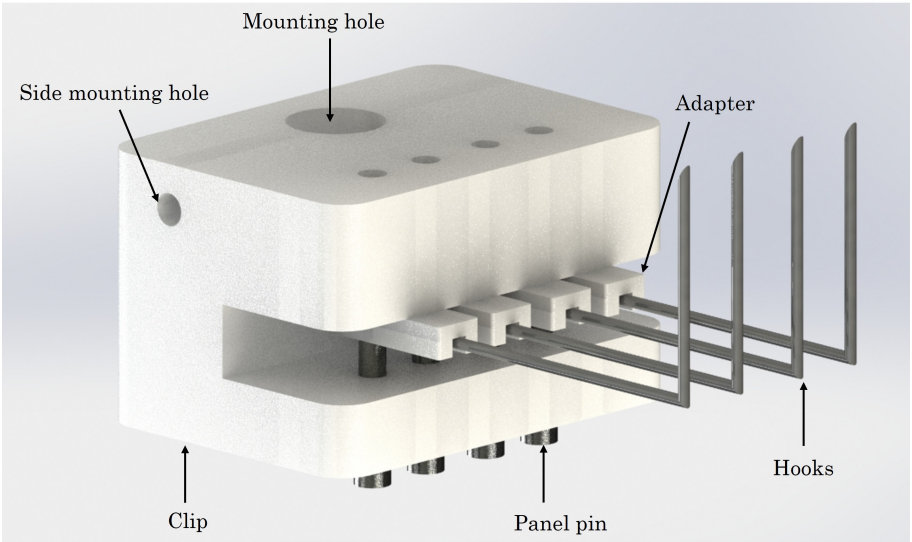

Figure 3.5 Image showing rake design

Figure 3.5 provides an isometric view of the designed rake. The device is assembled from a clip, four pins and four hooks. Each hook was secured to the clip using a steel pin as shown in Figure 3.5. The benefit of using pins as an attachment tool was that it catered for the hooks to freely rotate, subsequently allowing contra-lateral motion of the sample

during testing. The two vacant holes shown in Figure 3.5 are mounting features, where the larger and smaller hole were used to attach the rake onto the testing device and onto the transportation card respectively.

3.5.1 Fabrication and Assembly of Rakes

With the complex geometry and sub 2 mm hole sizes used in this design, conventional machining or casting would be expensive options for manufacturing these rakes. Rapid prototyping methods such as resin SLA 3D printing and FDM 3D printing provided alternative methods to manufacture both the clips and hook adapters to the required dimensions and tolerances at relatively low cost. Figure 3.6 provides a photograph of the clip prior to removal from the print adhesion raft.

Figure 3.6 Image showing resin printed clip

The hooks were made from 23 Gauge (0.6 mm OD) sized hypodermic needles and resin printed hook adapters. The needles were first prepared by shearing off the plastic ends. Thereafter, the sheared end of the needles was bonded to the hook adapters using an epoxy adhesive. A glueing jig was printed to provide a bed for multiple needles and adapters to be glued at once. The jig also helped in ensuring that the two bonding parts were positioned correctly and that the needles lay parallel to the base of the adapter, as shown in Figure 3.7.

Once bonded, the needles had to be bent to form their hook-like form. To do so a manual sheet metal bending machine was used to bend the needles to the correct angle. A bending jig was made to allow multiple needles to be bent under a single action, ensuring the same length from bend to pin. A photograph of the bending jig with the needles is shown in Figure 3.8 and it positioned on the bending machine post bending is also shown in Figure 3.9.

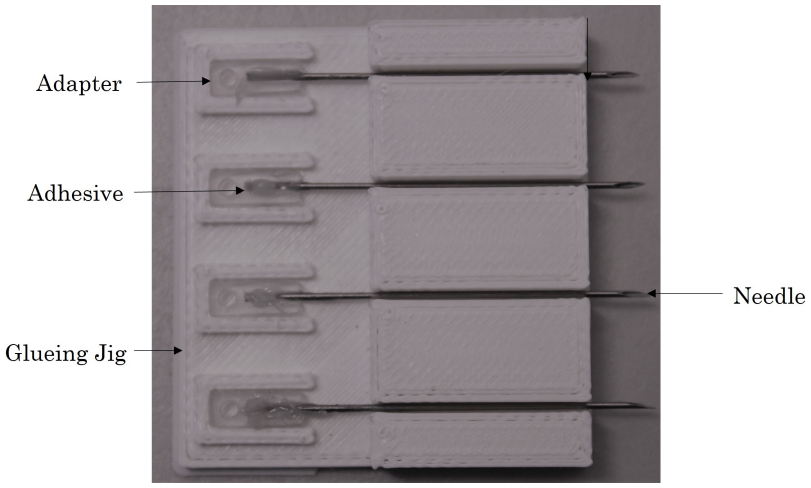

Figure 3.7 Photograph of Glueing Jig with needles being bonded to their adapters

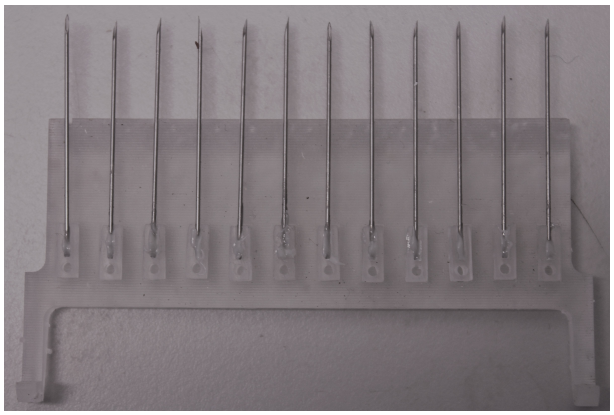

Figure 3.8 Photograph of needles seated in the bending jig

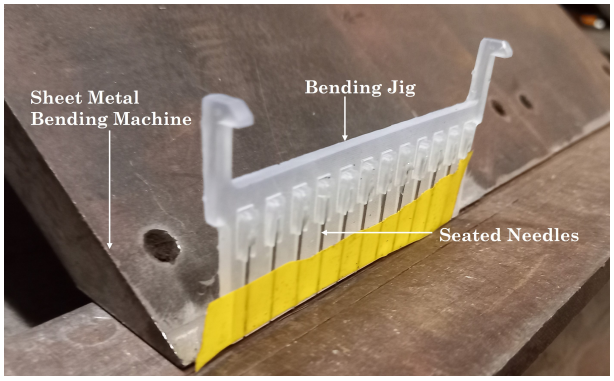

Figure 3.9 Photograph of needle bending operation

Assembling all the components was done using a rubber mallet. The tolerances of the holes on the clips were such that a mallet was required to guide the steel pins through their respective holes on the clips. Once the pins exposed themselves in the gap of the clip the fabricated hooks were inserted, aligning the hole with the pin. After ensuring that the pins had passed through the hooks the pins were then hammered up until the head of the pin touched the top face of the clip.

3.6 Design of Specimen Preparation Rigs

This section focuses on the tooling designed to prepare the sample for planar biaxial testing. The preparation encompasses; orienting the sample, attaching the rakes onto the specimens, excising a square-shaped specimen and transferring the specimen onto the PBT. This section is broken into four subsections to cater for these different exercises.

3.6.1 Rake Attachment Rig

An illustration of this device is presented in Figure 3.10. The purpose of this tooling was to devise a way to hook the test sample onto the rakes at its designated location and orientation. Its notable features are discussed in the subsections below.

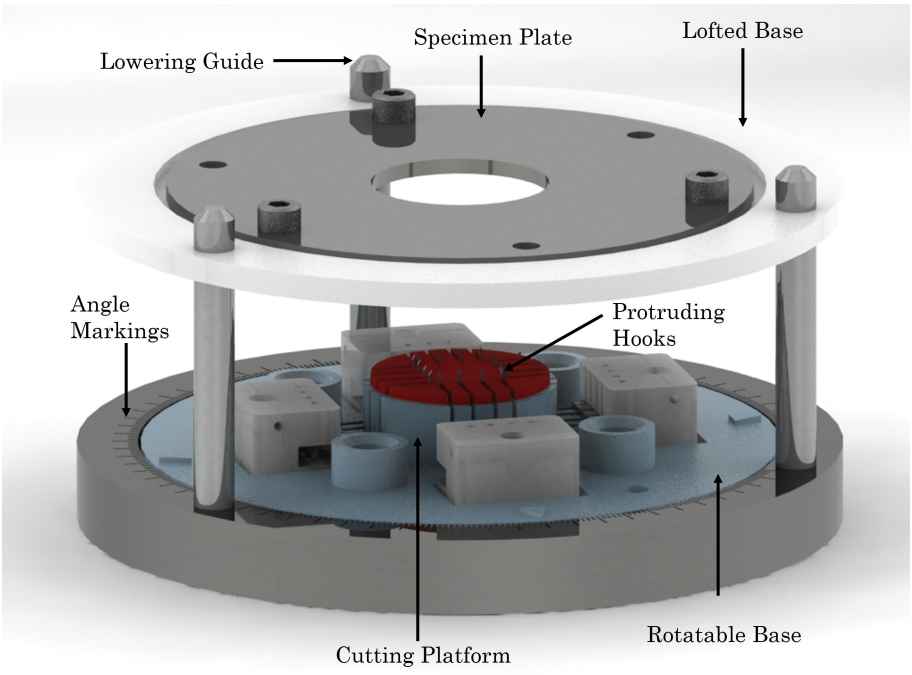

Figure 3.10 General assembly of rake attachment device

Lowering Guides

There was a need to lower the sample onto the exposed hooks in a controlled manner. To provide a means to achieve these three guides were fitted on the metal base onto which a lofted base would slide up and down on it whilst carrying the sample. The lofted base was fabricated with an ingress to seat the specimen plate which holds the speckled sample from the bulge tester. Six alignment holes have been placed on the lofted base to consistently seat the specimen plate in the same orientation relative to the metal base. This was of particular importance as the experiment was sensitive to the orientation of the mean fibre axis (MFA) on the specimens.

Rotatable Base

The rotatable base has the freedom to rotate about its locating key. This allows the user to rotate the rakes such that the axes lie along with the sample major and minor axis before it is lowered onto the cutting base. The metal base has angle markings machined on it to measure the angle of rotation. The shorter markings signify increments of a single degree and the larger showing five-degree intervals. For uniformity, the guides were located along the same planes as the holes of the base plate so that the only rotation that can occur was base. Also designed on the base are four embedded seats which are used to hold the rakes in position throughout the sample preparation process.

Cutting Platform

This provides a platform for seating the sample during the cutting action. The component features slits running through it, which were used to align the hooks parallel to one another, locate them in the correct orientation and hold them stationary. The height of the base was kept such that the hooks could protrude 10 mm above it. Once the sample has been lowered onto the cutting base the hooks would have pierced through the tissue and hence attaching the sample to the rakes.

The journey to the presented design was an iterative process, with many prototypes of different configurations being investigated. Appendix A.2 provides a description of a discarded prototype and what lessons were learned from it.

3.6.2 Specimen Punching Device

This subsection describes the tooling developed to cut the sample into its square geometry. Different approaches were designed and tested to assess how best to cut the membrane tissue. The hyper-elastic nature of skin made it difficult to get a clean square slice. Appendix A.1 provides a description of an alternative failed methods taken to cut a

square specimen and the insights obtained through the process. Figure 3.11 illustrates the general arrangement of the chosen mechanism.

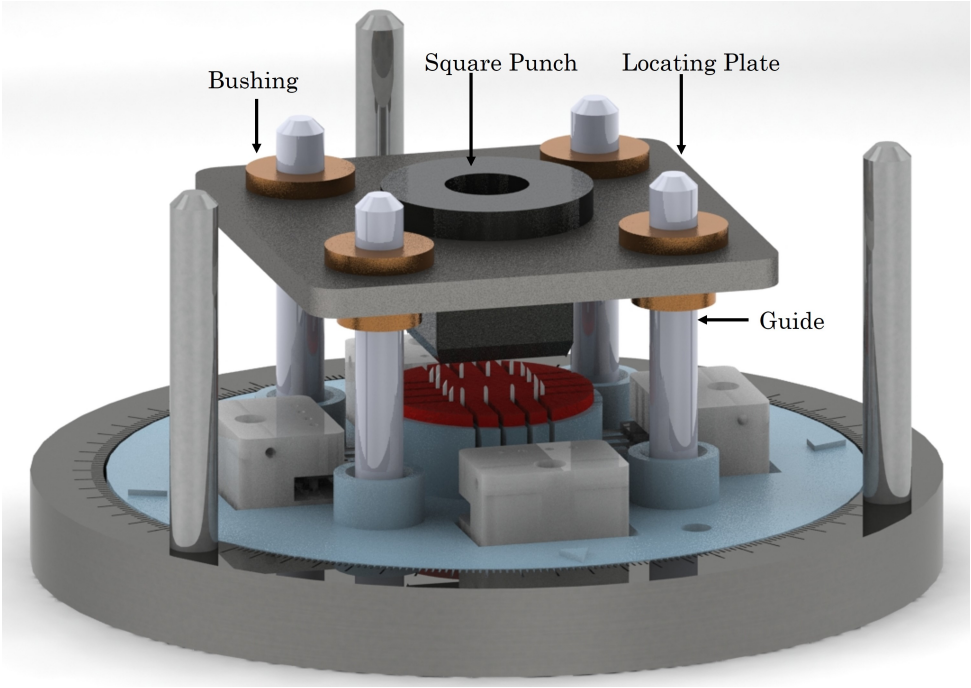

Figure 3.11 General assembly of Punch Mechanism

This device consists of a square punch, a locating plate and four guides. The square punch is fastened onto the locating plate such that the two pieces translate as a unit up and down the four guides. Once in position, the punch is subjected to an impact load which forces the punch to cut through the specimen and the rubber platform. The impact load is provided by a hand operated arbor press providing up to 2 ton of force that can impact the punch more than once if the specimen is not cut cleanly. Having the guides ensures that the same perimeter of the tissue is being cut through each iterative impact.

Fabrication of Components

Of the four main components of this device, only the rubber base and square punch were slightly more complex to fabricate. A brief discussion of the fabrication process is included below:

The square punch was machined from an M300 round bar and heat-treated to improve the hardness of the bladed end. Not hardening the punch would cause the sharpened end to roll and chip during the punching process. The heat treatment involved placing the punch into a furnace preheated to 700 °C and holding it there for an hour after which it is quenched in oil and allowed to cool at room temperature. Lastly, the bladed ends were sharpened by running the cutting edge against polishing paper until the desired level of sharpness was achieved. A rendered model of this part is displayed in Figure 3.12a.

(a) Model of hardened punch

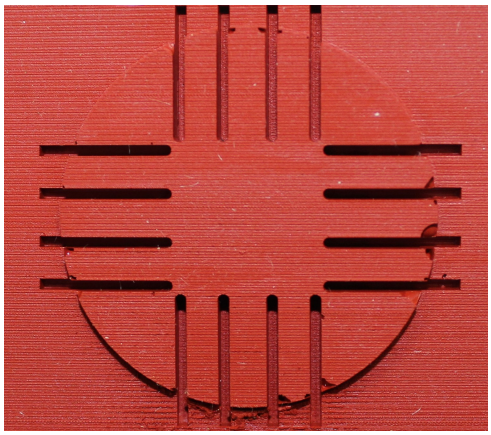

(b) Photograph showing cast rubber base

Figure 3.12 Images of hardened punch and cast rubber matt

The rubber base had to be cast to the required shape. Casting was found to be the only method available where the dimensions and shape of the slits could be controlled. Other conventional methods like cutting a rubber mat into the desired shape were not practical given that the slits had dimensions below one millimetre. The reason why the slits had to be shaped accurately was to ensure that the hooks could pass through it easily during lifting whilst still providing enough base material for the punch to drive and cut the specimen through. During preliminary testing, it was observed that larger gaps would allow the specimen to deform into the gap. This resulted in the specimen remaining intact in regions while the rubber base was cut.

The moulds were manufactured using Resin SLA 3D printing. The base was cast from SmoothOn MoldMax60 silicon elastomer, that has a hardness of 60 on the Shore A scale once cured. A guide showing the process of casting and mould preparation has been included in Appendix B.1. An image of the casted parts can be seen in Figure 3.12b.

3.6.3 Lifting and Transportation Card

Once the sample was hooked onto the rakes and punched to excise a square-shaped geometry, there was now a need to find a suitable means to transfer the prepared sample onto the PBT. To ensure that the geometry of the sample and the loading conditions would not be compromised during transfer, the tool had to meet the following criterion:

1. The specimen shall not be stretched during transportation
2. The hooks shall remain parallel and not pivot during transportation
3. The four rakes shall move in unison and remain in plane,
4. The tool shall be easily detachable
5. Shall be able to seat rakes securely on the PBT device.

After considering these requirements, a lifting card was designed and is displayed in Figure 3.13. The card provides a rigid structure that seats onto the four rakes and secures the specimen from being stretched during transportation. Holes included on the side walls allow slotted pins to be turned through and pressed against the wall of the rakes. Pins provide enough frictional restraint such that it holds the rake in position and hence the card may be lifted in unison with the rakes. An additional benefit of using this rigid card was that it made it easier to mount the rakes onto the PBT device.

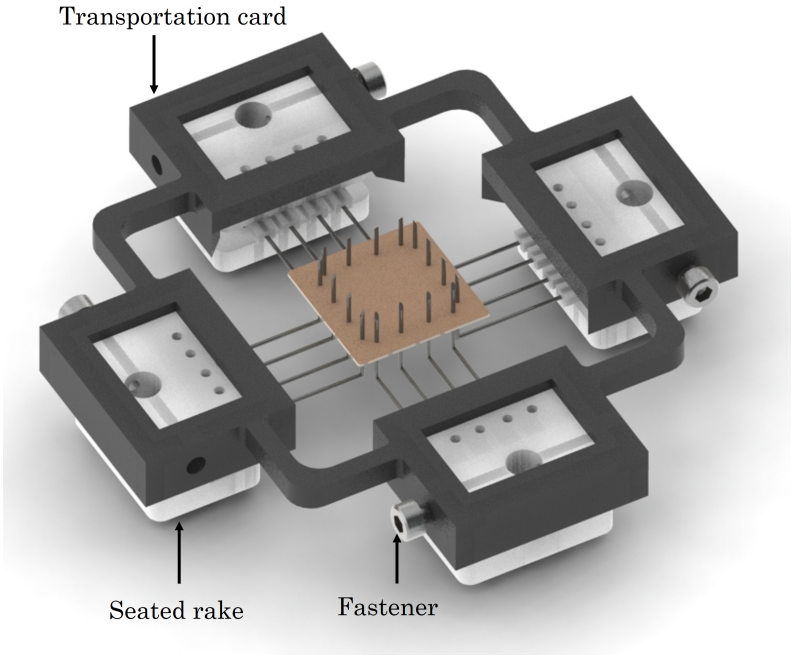

Figure 3.13 Illustration of Lifting card fitted onto the rakes

3.7 General Modification

Alterations had to be made to the PBT and bulge testing device to accommodate the new gripping system. The biaxial arms and saline bath were some of the components that had to be redesigned and fitted. A brief description of the different components is given below.

3.7.1 Biaxial Arms

The biaxial arms had to be redesigned with their dimensions altered to suit the designed rakes. These arms had shortened arms and the seat where rake clips were lower. With the old set of arms and clamping system the carriages had an allowance to travel 15 mm away from the centre. Shortening the arms prevented the need to relocate the carriages further apart and thus maintained the same range of motion. Also lowering the seat ensured that

the specimen lay in plane with the load cells, which minimised any bending loads being transferred to the load cell.

3.7.2 Saline Bath

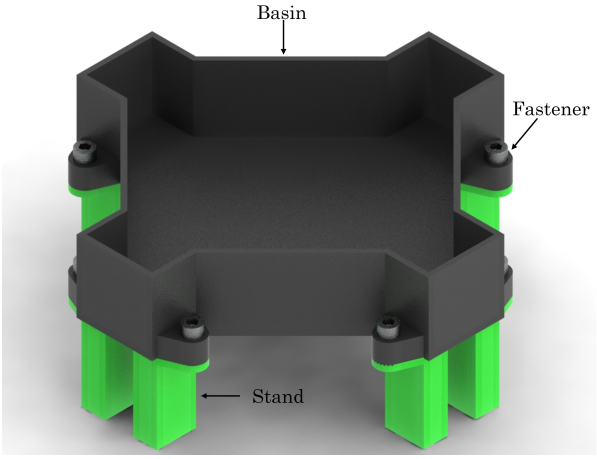

Figure 3.14 Illustration of saline bath

Figure 3.14 shows the redesigned saline bath which is composed of a FDM printed PLA basin and four stands secured together using M5 screws. The main feature of the new design was that the bath can be seated into the C beams without interfering with the carriages and driving threads. As a drain port posed risks for leakage onto electrical components, the bath was only filled and emptied using a syringe.

3.7.3 Sleeves

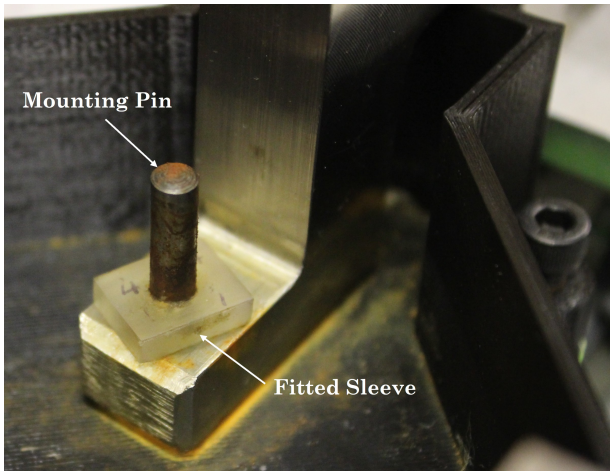

Figure 3.15 Photograph of sleeve fitted on a biaxial arm

After fitting the new arms onto the PBT, it was visually observed that the seat of all the arms did not lie on the same plane. Hence, for each arm a sleeve (see Figure 3.15) of a

specific thickness was resin printed to bring the seats up to a single plane. All adjustments were made so that the specimen would sit in plane with the load cell. The reason behind this was to minimise any bending stress being applied to the load cell, since the intended stress state for these experiments were to be axial only. In Appendix B.2 the heights of each arm relative to the base and heights of their respective sleeves are given.

3.7.4 PBT DIC Calibration Card Seat

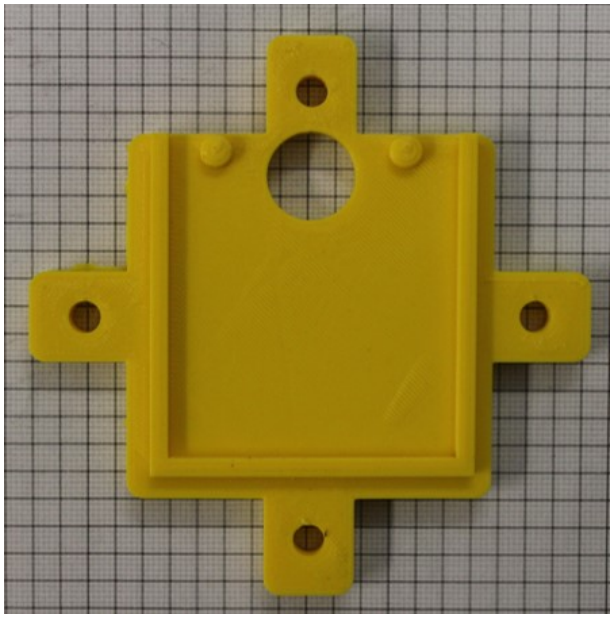

Figure 3.16 Photograph of the PBT DIC Calibration Card Seat

Both the planar biaxial and the bulge test make use of DIC to measure the deformation of the tested sample. When configuring the cameras a calibration card is usually held at the same position where the sample would be located during testing. The bulge tester already had a suitable calibration card holder designed by Pons [10]. It was necessary to fabricate a new PBT calibration card holder to suit the revised specimen and grip geometry(see Figure 3.16). This card hosts the same features as that of the bulge tester's card holder but with different mounting features which caters for the pins on the biaxial arms. The height of the card holder was designed such that it would lie in plane as the test specimen.

3.7.5 Pin Alignment Tool

The purpose of this part was to check that the biaxial arms and their pins were aligned and located the correct distance apart following any maintenance and re-assembly. The arms in each pair had to lie parallel to each other and each pair had to be perpendicular to the other set. The aim of this exercise was to minimise any bending stresses that

would be transferred to the load cell if one of the arms were misaligned. With the pins and arms aligned, the risk of any interference when lowering a specimen onto the arm was also reduced. A photograph of this tool seated on the arms is given in Figure 3.17.

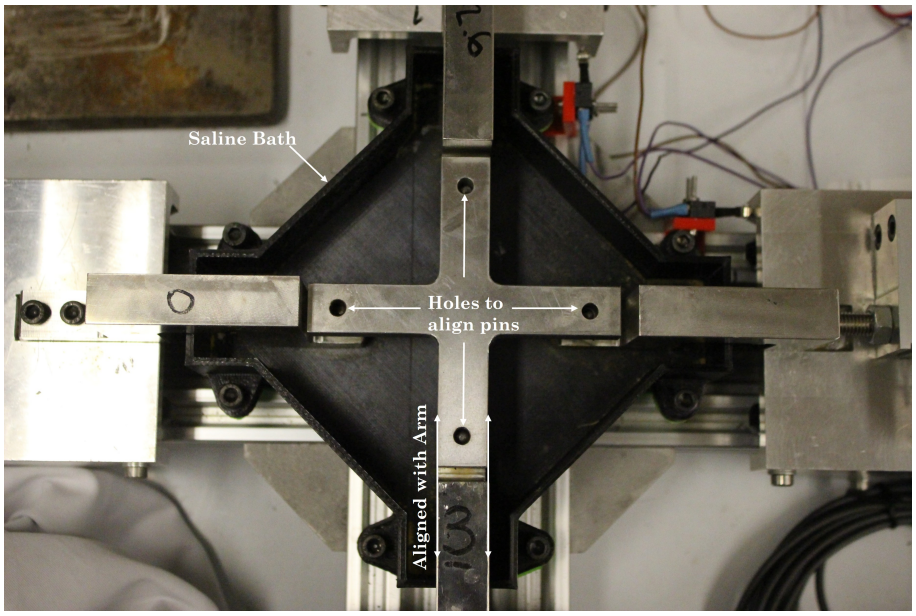

Figure 3.17 Photograph of pin alignment card locating the positions of the arms

The component was machined from stainless steel to achieve high rigidity and fine tolerances. The alignment tool arms were kept at the same width as the PBT arms to make it easier to visually identify any misalignments.

Chapter 4

Experimental Methodology

This chapter describes the methodology used to conduct a planar biaxial tensile test. The methodology is not novel but rather an iteration of the process developed by Pons [10], where the major difference stems from the use of the rake-based attaching system and not the previously used clamping configuration. This section first describes the DIC deformation measurement technique used when conducting both inflation and PBT tests. Thereafter the sequence of steps for complete bulge and PBT testing for a sample is described.

4.1 Strain Measurement Technique

Present in both experiments was the need to measure the strain profile across the specimen. This had to be achieved accurately and repeatedly using the available DIC equipment. Using the DIC to capture strain data was more challenging than expected as several prevalent issues had to be addressed to get meaningful information.

4.1.1 Optics and Lighting Condition

An objective of this project was to test the tissue as close to in situ as possible, requiring that the specimen had to be kept moist and hydrated. Having a wet membrane tissue meant that the surface was highly reflective and any light shone directly onto the specimen would cause a substantial reflection to be captured by the cameras. The DIC technique relies on greyscale values to track the movement of speckles across an ROI and significant reflection results in a saturated pixel. Facets containing saturated pixels cannot be tracked using the DIC method; hence, the software fails to correlate facets that undergo significant reflection at any point during testing.

Related use of DIC by Curry, Caine and Pons [8, 9, 10] avoided reflections by directing the light away from the specimen. A shroud reflected the light towards the specimen in a diffuse manner. Several attempts were made to imitate this setup. However, because there was no direct control over how the sheet would sit and reflect the light source, the reflections could not all be avoided. The configuration of the cameras and lighting used by Pons [10] on the bulge and planar biaxial test can be seen in Figure 4.1 and Figure 4.2. These 8-bit cameras had a resolution of 5 MP.

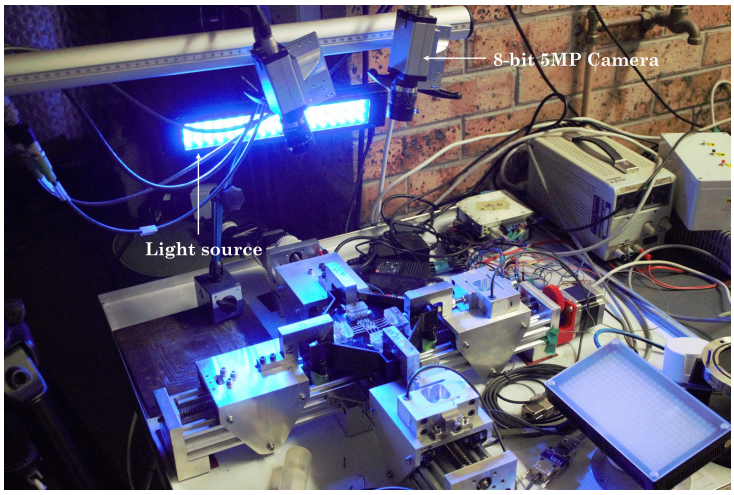

Figure 4.1 Configuration for planar biaxial test

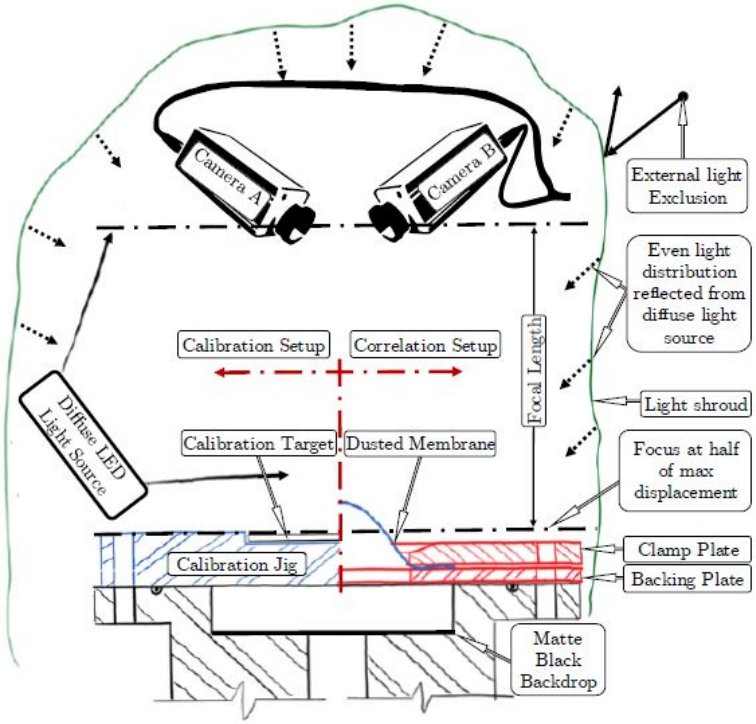

Figure 4.2 Configuration for inflation test [10]

Other methods were also used to reduce the harshness of the reflections such as dimming the light source as much as possible, positioning and angling the light source as far as possible to provide an even distribution of light, closing the aperture of the cameras as much as possible while increasing exposure time to compensate. The problem with these measures was that the changes reduced the amount of light being shone onto the specimen and being captured by the cameras, to such an extent that most of the specimen was relatively dark and only a limited range of greyscale values was captured for these regions. The facet size was increased to ensure tracking, which resulted in fewer points at which displacement was evaluated. Subsequently, a poorer estimation of the strain behaviour across the specimen was captured. Figure 4.3 gives a visual demonstration of samples loaded on the bulge tester under these lighting conditions in Dantec's Istra View. This view has its own unique RGB colour scheme, where on one extreme regions coloured magenta are classified as overexposed areas and in the other extreme deep blue-purple areas are classified as underexposed, both of which should be avoided to achieve good correlation and tracking of deformation across the ROI. Figure 4.3a, shows an underexposed region, where the majority of the area is coloured deep blue-purple (underexposed areas), with very few brightly coloured speckles (that the software could track). For comparison Figure 4.3b presents an image of a well exposed region, with a lot more coverage of brightly coloured speckles and regions coloured in a lighter blue colour, which the DIC software as able to correlate well.

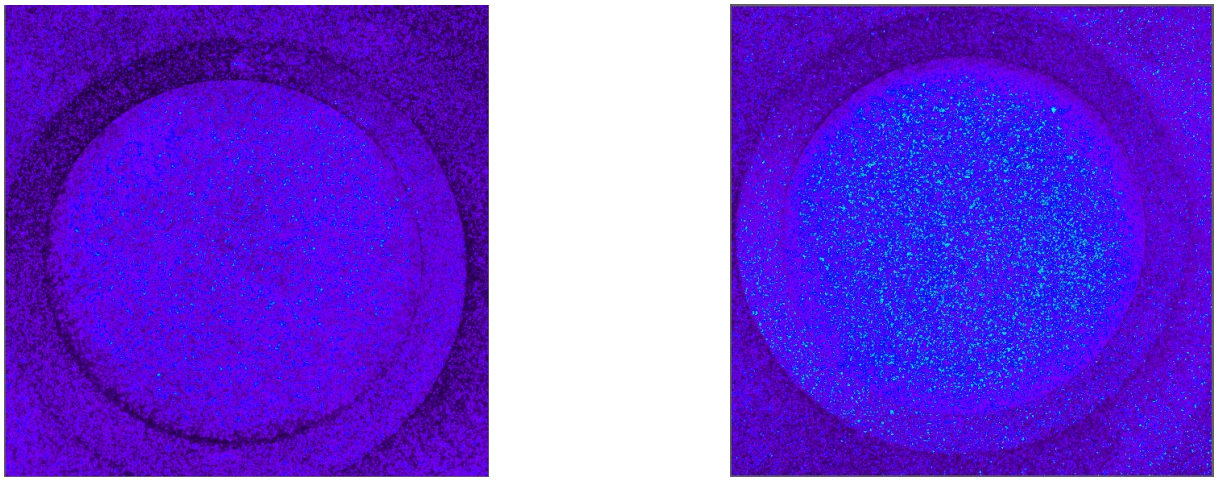

(a) Underexposed **(b)** Well exposed

Figure 4.3 Demonstration of a specimen under different exposure

An alternative means to illuminate the specimen had to be found to capture meaningful data. Vos, a colleague also using DIC, suggested the use of cross-polarising filters to eliminate harsh reflections, which was also described by Le Page et al [81]. The principle of cross polarising filters is illustrated in Figure 4.4. Unpolarised light from a source is shone onto a vertical polarising filter that only allows light oscillating along a specific

plane to pass through. The rays passing through are limited to vertically polarised light. If a horizontally aligned polarising filter is placed further ahead, then vertically polarised light will fail to pass through [82].

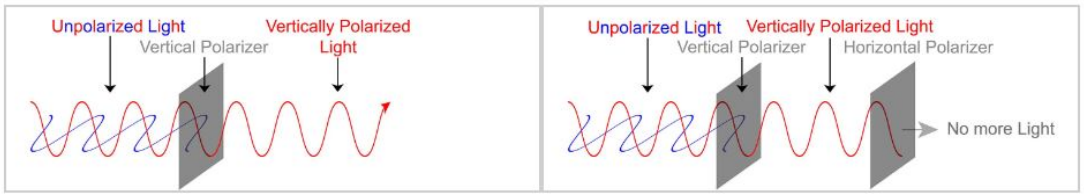

Figure 4.4 Visualisation of how cross polarising filters interacts with light [82]

Adopting this same principle, a polarising filter was placed in front of the light source such that the specimen was now illuminated under a polarised light. When this light bounces off the specimen, strong reflections are light with the same polarisation (specular reflections). However, diffuse reflections will have oscillations on different planes. Placing the second pair of filters on the cameras and rotating them such that they aligned perpendicular to the filter on the light source, meant that these pure reflections (i.e polarised light) would fail to pass through. Hence only the diffused light is captured by the cameras.

This effect is illustrated in Figure 4.5, where Figure 4.5a was captured without polarising filters, and the large magenta patch denotes overexposed pixels. Figure 4.5b shows the same specimen captured with aligned polarising filters. After aligning the filters correctly, the area previously covered in magenta (overexposed regions) now showed an evenly illuminated region with numerous speckles being highlighted. This allowed the DIC software

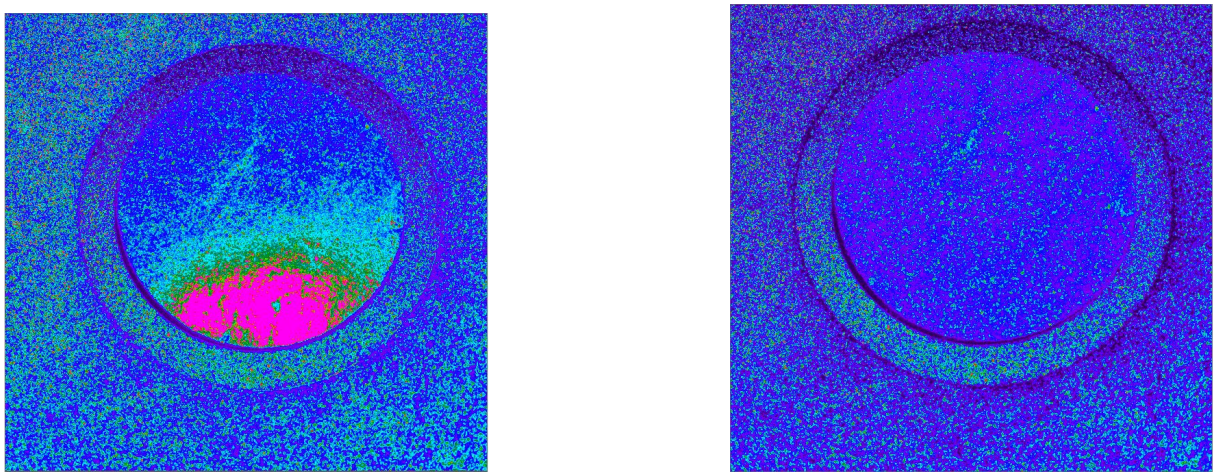

(a) Image captured without polarised filters

(b) Image captured with polarised filters

Figure 4.5 Demonstration of the effect of capturing images with polarised filters under the same lighting condition

to track the speckles on the specimen in previously overexposed regions. The incorporation of Cross Polarising Light (CPL) filters brought an additional benefit. There no longer was the need to have the light source facing away from the specimen and onto a cover sheet to reflect light in a dispersed manner towards the specimen. A single light source could now be mounted onto the camera frames and shone directly onto the specimen. This significantly reduced the time taken to set up the lighting conditions when testing. The apertures could be opened even further allowing more light to enter the camera improving the camera's ability to capture a wider spectrum of greyscale values. However, care was taken to ensure that the speckled samples remained in focus since increasing the aperture reduces the cameras depth of field, which would also result in loss in correlation. The new arrangement of the cameras and lighting are presented in Figure 4.6.

4.1.2 Speckling Technique

As described in Section 2.5.2 the fall-out technique was used to speckle the ROI of the tissue. To ensure an even distribution of the speckles, after the first pass the tissue would be rotated and sprayed again. Previously when speckling membrane tissue, a matt-white paint was used to speckle on the translucent specimen. The intent was that the DIC cameras would track the white speckles on an evenly coloured dark background. However, this method opposes how DIC tracks points as the programme relies on picking up different greyscale values. Using pure white speckles against a largely black background meant that only the extreme upper and lower values of the greyscale spectrum were being used, with little use of the spectrum in between. Only the extreme right and left of the greyscale index were being tracked with fewer values in between. This was particularly problematic if the initial spray wasn't satisfactory, as it's not possible to wipe paint from a tissue specimen. Dr Govender, who is the project supervisor, suggested the use of different coloured matt spray paints to use a larger range of the greyscale spectrum, particularly when re-speckling.

After testing different colours the following paint combination was chosen: tidal blue, blush pink and charcoal black. To speckle, the specimen was placed in a fume box and a cardboard stencil covering everything but the ROI was placed over it. First, a single pass of charcoal-black paint was sprayed and then a single pass of tidal blue paint. The disk that the tissue layer was on was then rotated 180° and a final pass of blush pink paint was sprayed on it. At this stage, the sample was ready to be clamped onto the bulge tester but to mitigate the time taken to speckle the sample for the PBT, the plated sample was flipped, and the process was repeated. When necessary talcum powder was then dusted on to further increase the contrast of grey values.

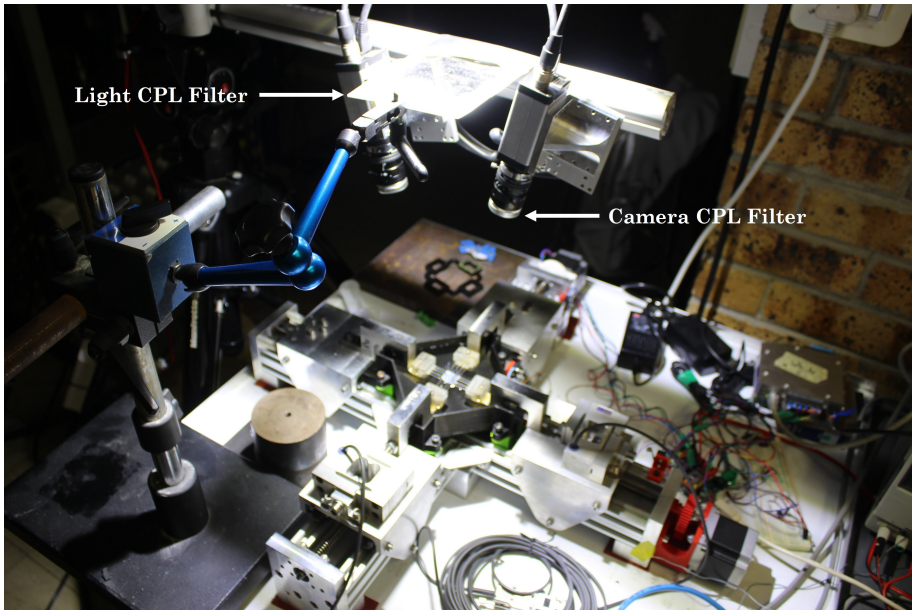

(a) New planar biaxial tensile test camera configuration

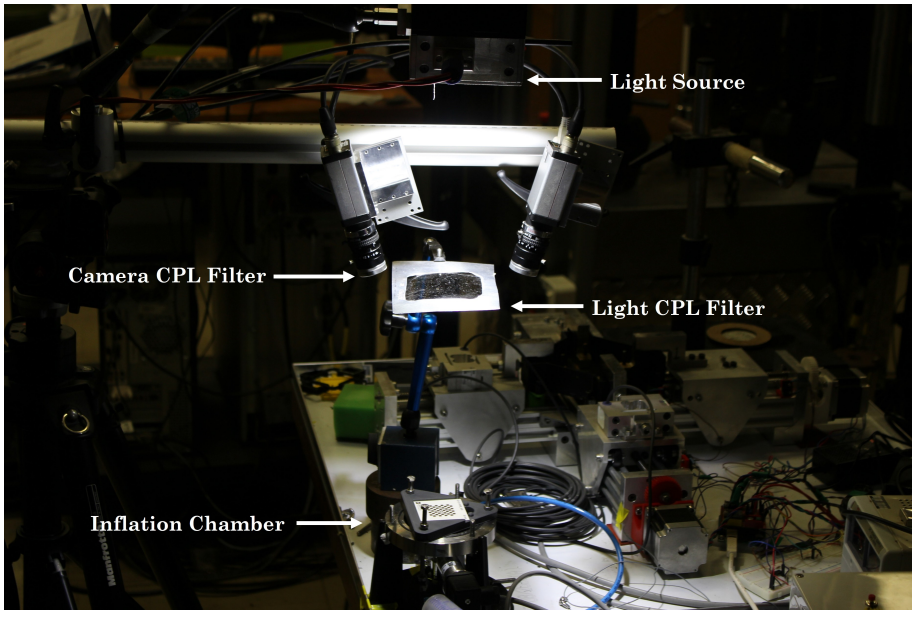

(b) New inflation test camera configuration

Figure 4.6 Photographs showing new camera configurations

4.2 Sample Preparation for Bulge Test

The SIS tissue was sourced from a local abattoir, and sealed in a bag containing enough salt to preserve it. For ease of use and to ensure that the tissue did not degrade, the casing was sectioned into tubes of length 150 mm and sealed in bags containing a maximum of ten tubes. Each bag was also filled with excess salt to facilitate preservation.

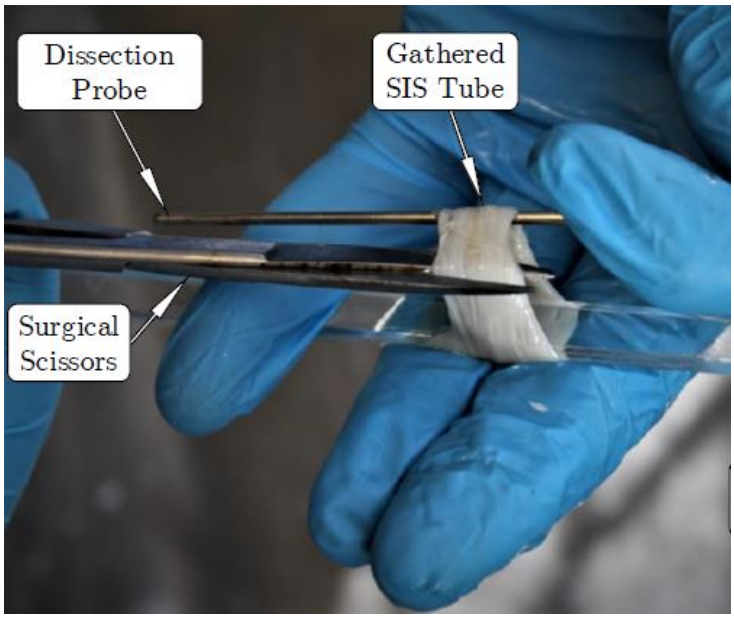

Figure 4.7 Opening SIS tissue to rectangular form [10]

In preparation for the test, a shortened tube had to first be rehydrated by soaking overnight in normal saline solution. Once rehydrated, the tube was carefully threaded over a Perspex rod under running water. With the aid of a smaller steel rod, that was passed between the glass rod and the covering tissue, the sample was gently stretched to allow insertion of scissors and excise the tube lengthwise (refer to Figure 4.7). The now rectangular sample was then spread onto the bulge tester's sample plate. Care was taken not to excessively stretch the sample across the 35 mm aperture and any excess material infringing over the mounting holes was trimmed. The specimen was visually inspected for any holes in the ROI or any other defects. If there were any holes present the sample was discarded and a new sample was loaded onto the plate. The final preparation for the bulge test was to speckle the plated sample which was performed as described in Section 4.1.2.

4.3 Bulge Test Methodology

4.3.1 Calibration of DIC Equipment

Before recording a test, the cameras had to be calibrated using Dantec's calibration target. A cardholder was fabricated specifically to seat the calibration target on the bulge tester rested at the same height as the loaded sample. When calibrating the cameras, the instructions were to alter the orientation and angle of the target for each of the ten images taken, an example of which is shown in Figure 4.8.

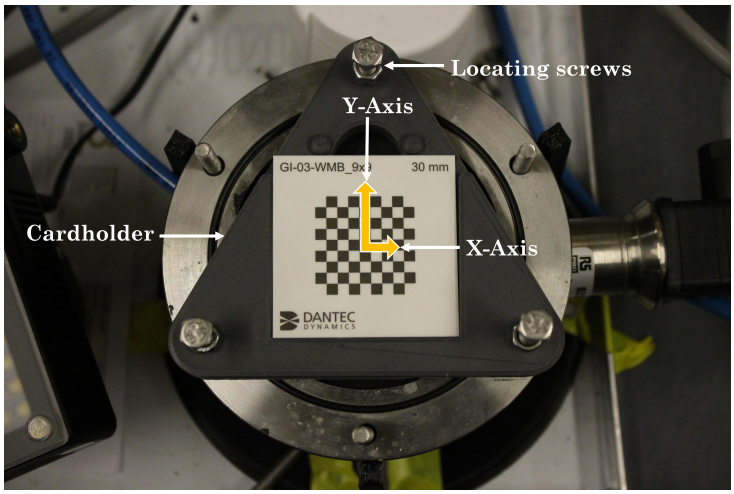

(a) Image of calibration card seated in plane

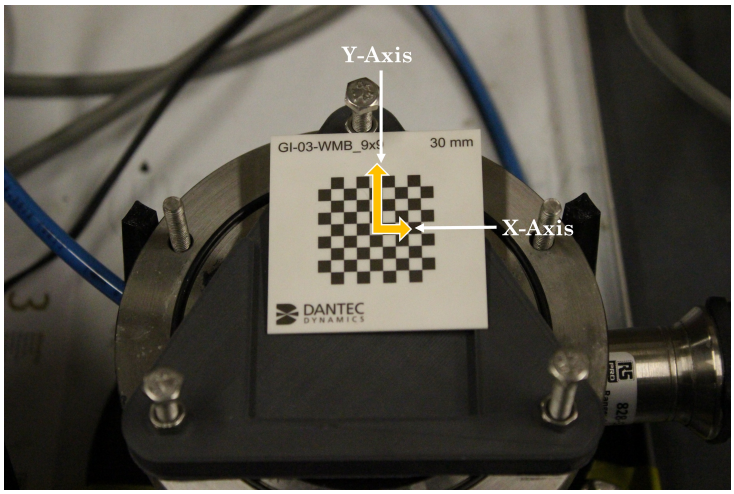

(b) Image of calibration card seated at an angle

Figure 4.8 Demonstration of calibration card seated in different orientations on the bulge tester

4.3.2 Loading and Inflating Sample

To begin testing, the plated speckled specimen was mounted onto the inflation chamber with the surface that held the specimen facing up. A rubber gasket and a steel cover were placed and secured on top of the sample using six fasteners. The rubber gasket provided a seal that allowed the membrane tissue to be sufficiently pressurised.

Before inflating the sample, final checks were performed to ensure the lighting conditions were suitable, that the CPL filters were correctly aligned and that the speckles were being captured by the cameras. The DIC software provides a viewing mode called Istra View, which informs the user of the variation of grey values across the specimen. A large colour variation spread across the sample would result in good correlation and tracking of the individual speckles. Overexposed regions were highlighted in bright magenta and underexposed regions were coloured in deep blue-purple tone. Areas highlighted in either colour would result in a loss of displacement data. If necessary, the CPL lenses on each camera would be rotated to reduce the harsh reflection. For all tests using the DIC the software was programmed to capture images at a frequency of 10 Hz.

The procedure used to inflate the specimen was followed as stipulated by Pons [10]. The membrane tissue was inflated quasi-statically up to a pressure of 0.5 kPa, held at that pressure for a few seconds and then deflated. As a means to reduce the dehydration of the sample, the syringe that pumps air into the inflation chamber was filled with a small volume of hot water to create a humid air environment. After completing an inflation cycle a cover was placed over the sample to reduce further loss in moisture. Given that the processing of the data did not take long, short of enclosing the entire device in a humid environment, this was the most practical means of avoiding drying.

4.3.3 Mean Fibre Axes Identification

An algorithm was used to identify the angle at which the mean fibre axis (MFA) and cross fibre axis (CFA) lay relative to the y-axis. This algorithm required three inputs to identify the MFA of a specimen which were:

1. Evaluation XYZ displacement data from the Bulge Test in text file format.
2. Reference frame at which the specimen lay at its origin.
3. Frame at which the specimen reached its maximum apex under inflation.

After inserting the required inputs, a typical output of the algorithm is shown in Figure 4.10. In this instance the MFA and CFA were identified to lie 6° and 96° clockwise from the positive y-axis.

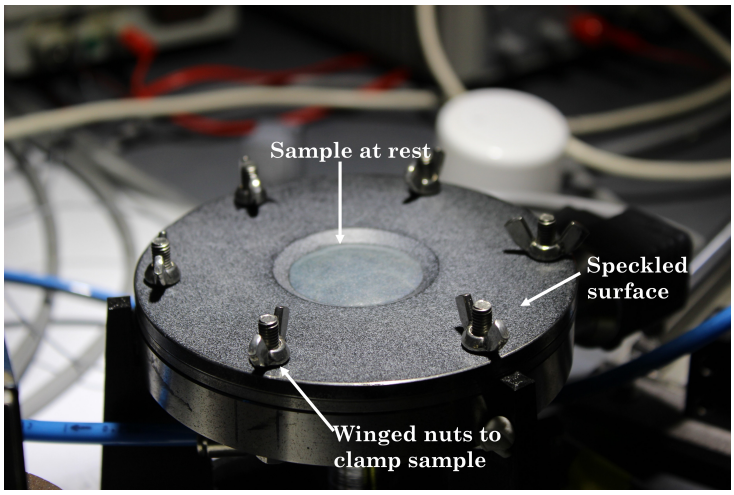

(a) Image of specimen loaded onto device

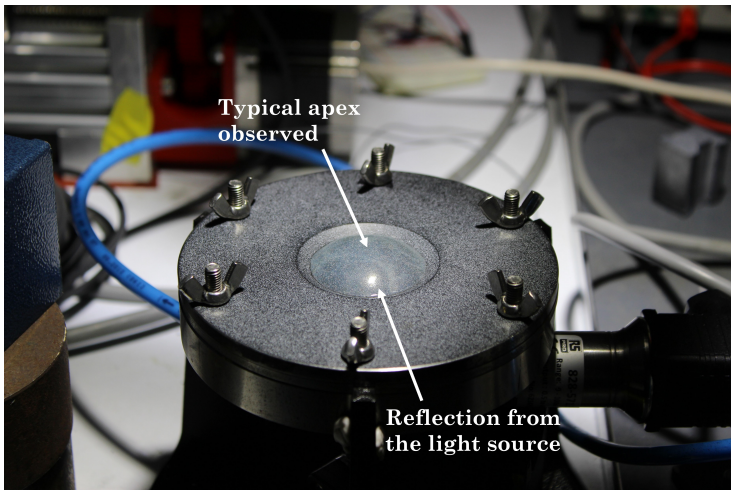

(b) Image of specimen fully inflated

Figure 4.9 Photographs of specimen undergoing a bulge test

4.4 Sample Preparation for PBT test

4.4.1 Rake Attachment Process

Now that the angle along which the MFA was identified, the rake attachment jig was then used to rotate the rakes to match the respective axis and to attach the samples to the hooks. It was critical to match the x-y axis of the plated specimen and the rotating base to prevent the sample from being mounted on the hooks in the incorrect orientation. Identifying marks were placed on one of the fasteners on the sample plate, on the lowering guides and the rotating base to identify the positive y-direction.

For a said sample if the MFA lay 60° counter-clockwise from the y-axis the base was first rotated to 60° clockwise. Next, the plated sample was dismounted from the bulge tester

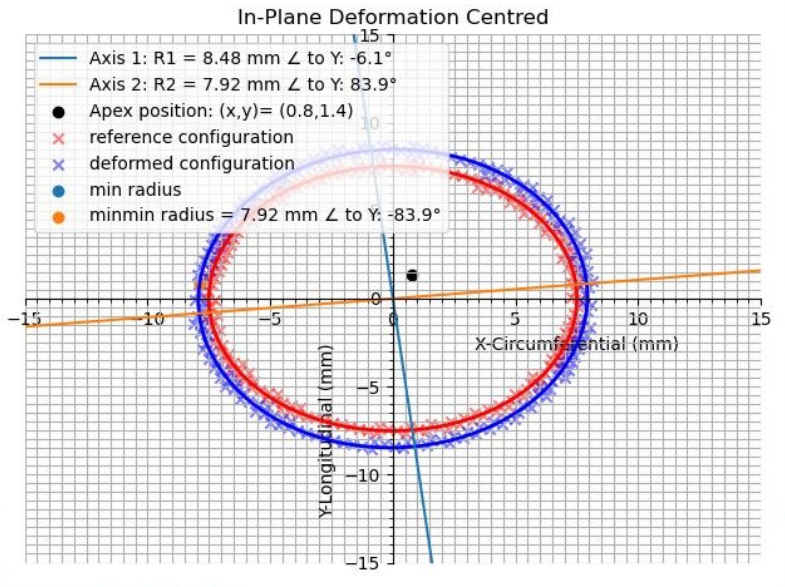

Figure 4.10 Screenshot of output from Algorithm

and secured onto the lofted base using three M5 bolts. The lofted base was then flipped over such that the specimen faced the ground and guided onto the cutting platform using the lowering guides (see Figure 4.11a). It was necessary to flip the lofted base over when lowering the sample, as it accommodated ease of transfer of the specimen onto the cutting platform without any interferences. The flipping of the specimen meant the rotation of the base also had to change direction.

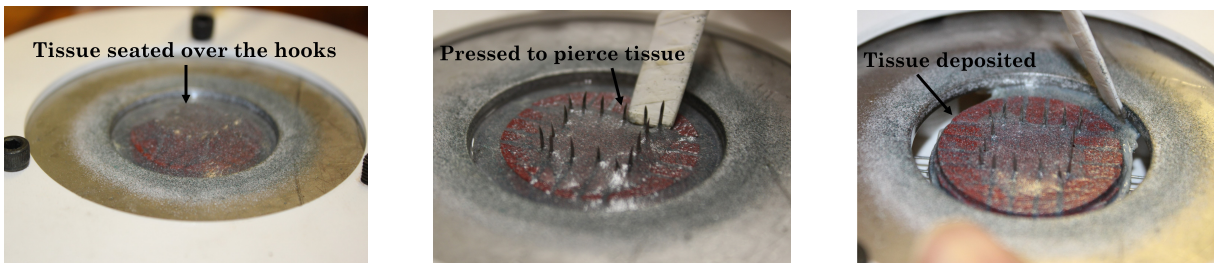

(a) **(b)** **(c)**

Figure 4.11 Photographs showing the final step of (a) lowering the tissue, (b) piercing it and (c) depositing it on the rubber base

Using a Teflon-wrapped spatula the membrane was then pressed between the protruding hooks to pierce the specimen and lower them onto the cutting platform (see Figure 4.11b). The lofted base was thereafter lifted off leaving the specimen seated on the rubber base attached to the rakes in the correct orientation. When needed the Teflon spatula was used to detach the areas of the specimen that stuck to the metal disk, as shown in Figure 4.11c.

4.4.2 Punching Square Shape

Figure 4.12 Photograph of punching rig assembled and positioned under an arbor press

Cutting the square shape required the use of the square punch and the arbour press. The arbour press was to impart an impact load onto the square punch which would then drive itself through the sample and the rubber base producing a clean square cut of the sample. To assemble the punching rig, the square punch along with the four punching guides were sub-assembled and carefully slotted onto the rotating base using the respective mounting holes as illustrated in Figure 4.12. When assembled correctly the punch would slide down the guides and sit on top of the specimen. Enough clearance was allocated if the jig was not correctly fitted to be reassembled without adjusting the specimen and hooks.

The now assembled rig was then transferred onto the workspace of the arbour press and aligned with the driving head of the press and punched. Figure 4.13 provides a photograph of a punched sample removed from the press. The edges of the cuts were inspected and if necessary, scissors were used to cut any remaining connective tissue. All excess tissue outside of the square was then removed and discarded (see Figure 4.14).

4.4.3 Loading Sample

Lifting the four rakes from the rig and onto the PBT machine was done using a transportation card. The card was designed to host locking pins along its side which would be passed through the card and into the rakes securing the components to one another as shown in Figure 4.15. After lifting the specimen with the card off the rig, a Teflon wrapped spatula was used to gently move the specimen down to the base of the hooks. In

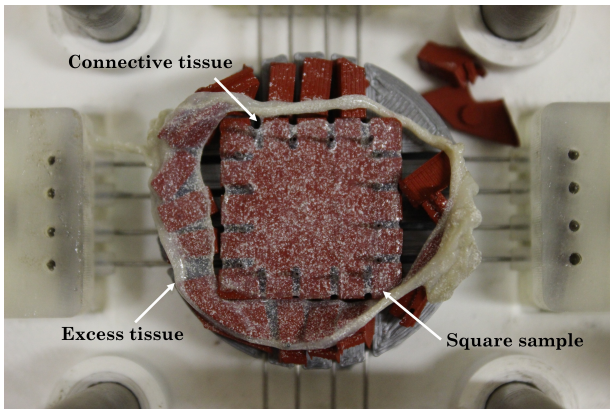

Figure 4.13 Photograph of punched sample

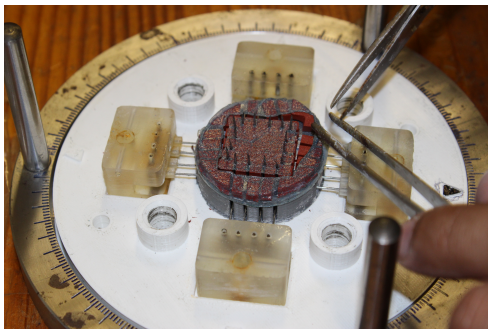

(a) Image of side excision being made onto excess tissue

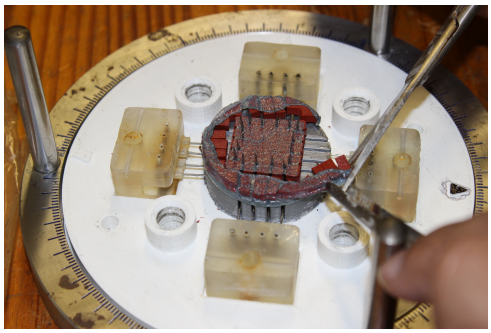

(b) Image of excess material being removed

Figure 4.14 Removal of excess tissue post punch

doing so, the square rubber base attached to the underside of the specimen was removed and discarded.

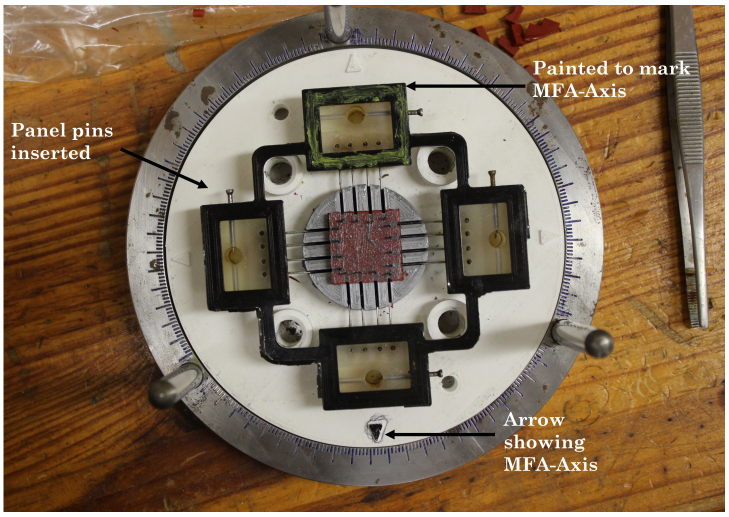

Figure 4.15 Plan view of sample fitted on transportation card

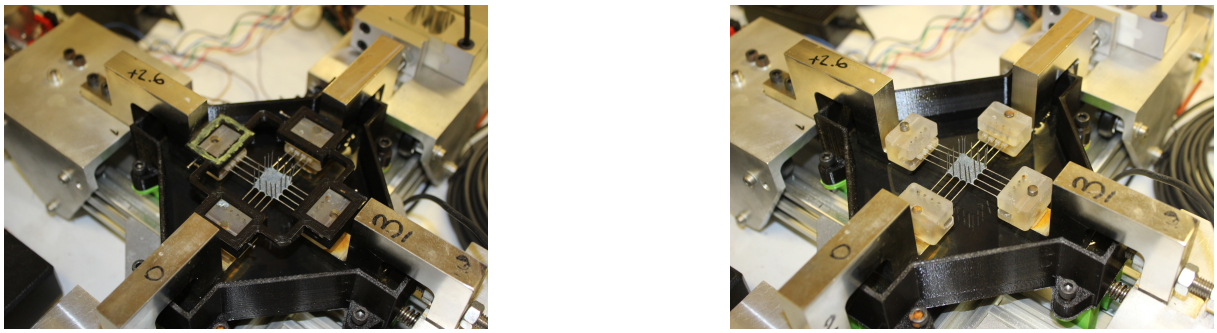

(a) Image of card with sample seated **(b)** Image of sample seated alone

Figure 4.16 Photographs displaying steps to load sample onto the PBT

The now fully prepared specimen was then lowered and fitted onto the PBT machine (see Figure 4.16). Before testing the pins on the arms were aligned and located to fit the rakes with minimal interference. To detach the transportation card the pins were removed, and the card was removed gently without disturbing and rotating the rakes. In the case that the hooks were disturbed, a spatula was then used to readjust the position of the hooks to their original positions. The last step included filling the bath with normal saline solution until it meets the underside of the sample. A syringe was used to control the feed rate of saline solution in the bath.

4.5 PBT Test Methodology

4.5.1 Configuration and Calibration of DIC equipment

Once the square sample was ready to be loaded onto the PBT machine, the camera frame hosting the light source and the two cameras were shifted from the inflation test to the PBT. The same process for calibrating the DIC as described in Sec 4.3.1 was applied, with the DIC coordinated aligned to the tensile axes (see Figure 4.17

4.5.2 PBT Extension Protocol

Consistent with past literature, specimens were subjected to quasi-static preconditioning before testing. A typical preconditioning cycle meant that the sample was stretched equibiaxially five times at the same rate to the maximum extension the actual test was conducted at [10]. Preliminary tests were carried out to identify the maximum permissible extension at which the specimen should be tested. An extension of 3.5 mm was found to be a suitable distance to stretch the specimen without tearing the tissue. As proposed by Pons [10], specimens were tested at five extension ratios; 1:1, 1:0.5, 1:0.75, 0.5:1 and 0.75:1 [10].

(a) Image of calibration card in plane **(b)** Image of angled calibration card

Figure 4.17 Demonstration of calibration card seated in different orientations on the PBT

4.6 Specimen Thickness Measurement

Given that the primary purpose of conducting these experiments was to generate stress-strain curves, it was important to gain accurate measurements of the thicknesses of each sample to estimate their cross-sectional area and hence determine a true stress response. Pons [10] fixed the specimens in formalin then embedded these in paraffin wax. The wax-mounted specimen was sectioned using a microtome, with each section stained and mounted on microscope slides. The stained tissue was photographed under a calibrated microscope and ImageJ used to post-process the images to measure specimen thickness. Following guidance from histology technicians at Groote Schuur hospital, Pons [10] noted that the formalin and paraffin wax treatment could alter the specimen dimensions due to dehydration, and subsequently recommended the use of cryogenic sectioning histology (cryo-sectioning) instead. The driving factor is that cryo-sectioning rapidly freezes the tissue, thus preserving structure and minimising changes in dimensions.

4.6.1 Cryo-section Histology Methodology

External assistance from the UCT Faculty of Health Sciences was sought to stipulate the specific methodology to follow. Like other histology techniques, this process can be broken into three main categories; preservation, operation of the cryogenic microtome and staining of samples were performed by staff at the Histology Laboratory in the Department of Human Biology. The responsibility of preserving the specimen, capturing images of the slides and processing images lay with the author. A brief of the methodology is given below. It is important to mention that two techniques were considered when preparing the tissue- a Paraformaldehyde (PFA) fixed method and a Non-PFA fixed method. Appendix E, has a brief containing a qualitative assessment that showed the Non-PFA fixed method better held the tissue structure and thus was chosen as the method to follow.

Preservation of Tissue

Once testing is complete, and both load and strain data have been checked, the specimen was then offloaded from the machine in preparation to be preserved. Lifting the specimen of the PBT was done by holding a pair of rakes on one axis and lifting them off the arms. The remaining pair of rakes remained in their seats as whilst lifting the tissue would slip off those respective hooks with ease. To detach the last two connected rakes, the sample was lowered onto a Petri-dish and the rakes were tilted in a manner that allowed the hooks to slip out of the specimen. Any excess water was padded out to mitigate water crystal structures forming when preserving the tissue. The crystal structures are known to damage and alter the dimensions of said tissue when preserving.

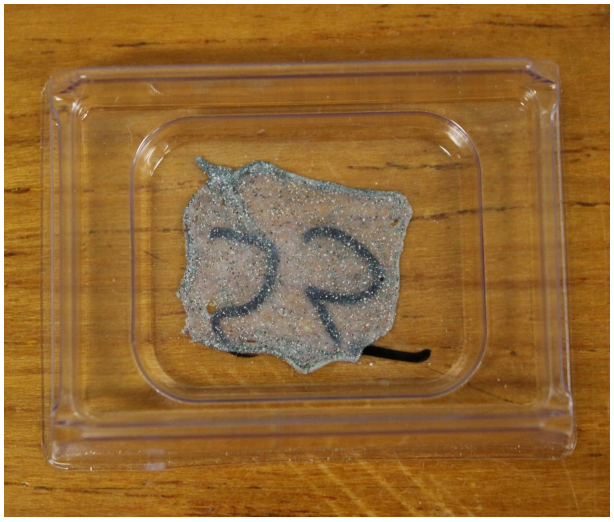

Figure 4.18 Photograph displaying specimen seated in square mould

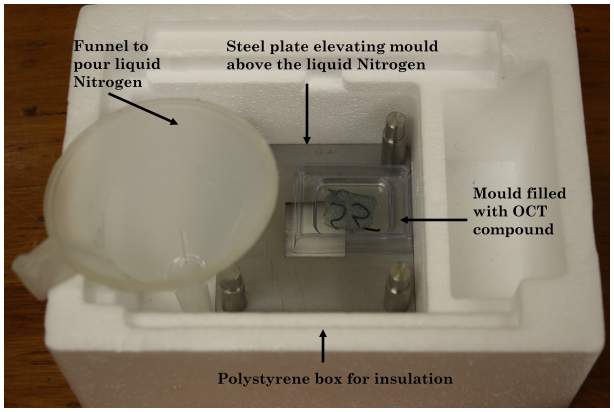

Figure 4.19 Photograph of filled mould placed in polystyrene box in preparation for freezing

The specimen was transferred from the Petri dish to a square acrylic mould for cryogenic fixing. A spatula was used to spread the specimen out as best as the author can to one layer thick. Thereafter, an optimal cutting temperature (OCT) compound was slowly

poured to fill the mould. Once filled, the mould was placed on an elevated steel plate in a polystyrene box. Liquid Nitrogen was then poured into the container to indirectly freeze the specimen rapidly thereby preserving the tissue structure of the specimen. Care was taken when pouring to ensure the liquid level did not rise above the steel plate. The intent behind this practice was to prevent the liquid from coming into direct contact with the specimen which would flash freeze and damage the specimen. Once frozen the now hardened mould was stored at $-30\,^{\circ}\mathrm{C}$.

Sectioning and Staining Tissue

The now frozen tissue was sectioned using a cryostat machine to expose the cross-sectional area and placed onto a slide. A haematoxylin and eosin (H&E) stain was then added to make the tissue visible under a microscope and thereafter an adhesive was poured over to preserve and fix the sections on the slides.

Mock samples sectioned to 10 µm, 25 µm and 50 µm thick to gauge and understand which thickness produced the best images when captured under a microscope. It was found that 50 µm produced the clearest pictures with easy-to-follow tissue boundaries and low intermediate tears along the length of the section samples.

4.6.2 Image Processing

Although the option was available to directly measure the thickness of the sample when viewed under a microscope, an imaging ThicknessTool macro was used instead. The benefit of using this tool was that the programme would identify the membrane and measure the thickness at multiple locations along the length, minimising user bias. Fiji ImageJ was the software used to run this ThicknessTool macro [83]. Figure 4.20 has been included to give a visual description of how the tool worked.

There were occurrences where the tool would record thickness outside of the tissue boundaries. These values were much lower than the expected thickness values and were filtered out using a python code. From the filtered results, the mean, variance, maximum and minimum thickness values were calculated.

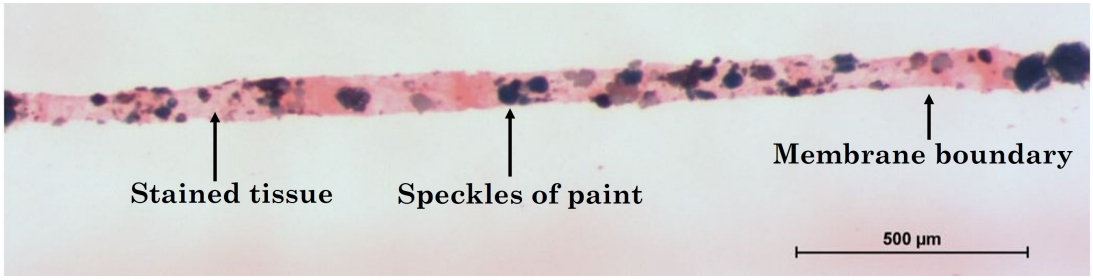

(a) Image of sectioned tissue inserted as an input

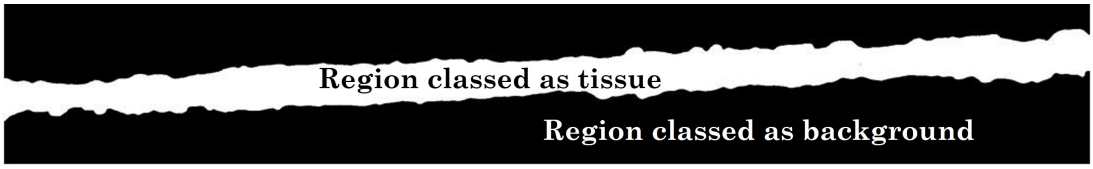

(b) Processed image where tissue has been identified and isolated from background

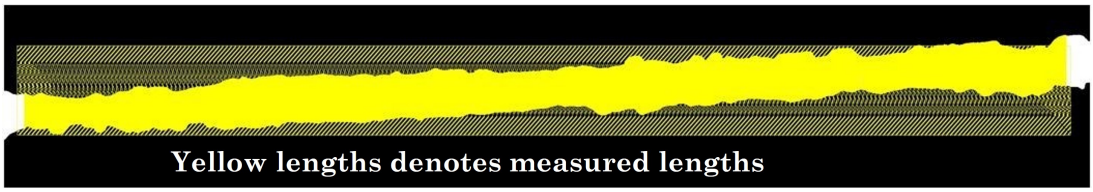

(c) Output from macro tool, showing sampled sections and lengths measured

Figure 4.20 Example of ImageJ processisng using prepared specimen 8 slide

Chapter 5

Results and Discussions

5.1 Assessment of Designed Components

5.1.1 Rakes

The primary design feature of these rakes was to facilitate the tissue deforming freely between the attached hooks, which exert only an axial force. This was observed in every sample that was tested, with the hooks swinging apart as the tissue expanded and coming back together as it contracts. In certain instances, when the rakes were not correctly seated the rake clips would rotate about the arms pins to realign themselves. Figure 5.1 gives two images showing how the specimen expands under biaxial tension.

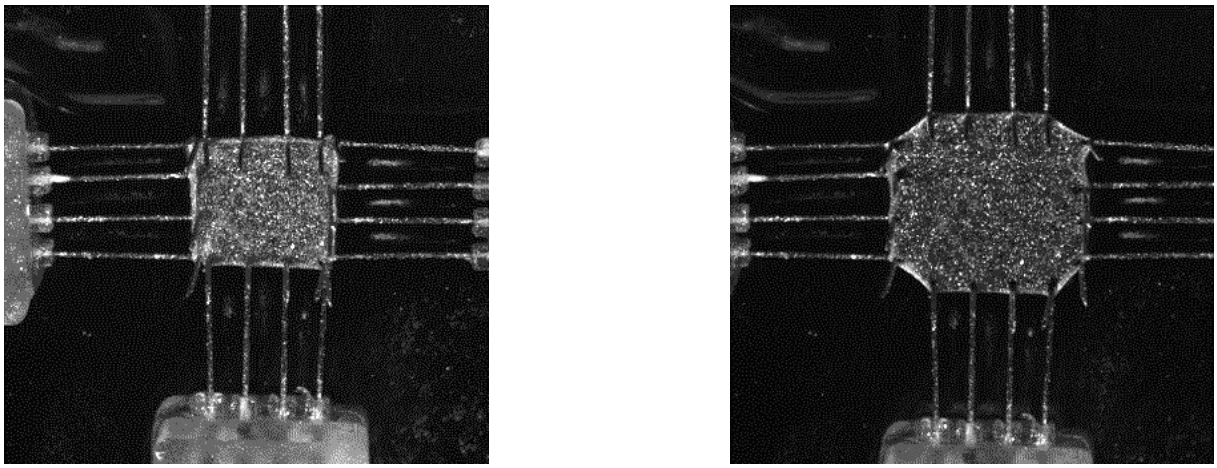

(a) Image captured of sample in its rest position

(b) Image captured of sample under full extension

Figure 5.1 Images highlighting the displacement of the hooks to allow contra-lateral expansion of the tested tissue

Regarding the rakes' structural integrity, the same set of rakes was used to test all prepared samples. The assembled hooks did not deform permanently nor detach during testing. Occasionally one or two pins had to be replaced, but that was due to the user dropping the clip from waist height. There was noticeable play seen on the stainless-steel hooks, as they would flex under tension. Over the course of testing because of this play, some hooks lay slightly higher than others.

5.1.2 Rake Attachment Rig

The designed rig worked well in seating and holding the clips in position. The rotating base could be freely rotated and the specimens lowered onto the hooks, without fear of moving the hooks out of position. The process of attaching the membrane tissue onto the hooks has been well described in Section 4.4.1. The only difficulty involved was lowering the lofted bases with the sample onto the rakes. This was due to the poor choice of tolerance on the lofted base to fasten the specimen plate to it. Every time a sample was lowered onto the rakes the user had to hold the specimen plate and the lofted base together or else the two would separate and the correct orientation of the sample would be lost. Maintaining the MFA axis was critical to the experimental process which meant that this step of lowering the sample was performed slower than the other methods.

5.1.3 Specimen Punching Rig

The punching mechanism worked well in providing a true and square cut for every specimen cut. Features like uncut edges, tearing of samples around the hooks and irregularly shaped specimens were not observed in the final design, using a rubber cutting pad on the 3D printed base. These can be attributed to the hardened punch holding its edge and sharpness over the course of testing. There was the need to cut strands of tissue connecting between the excess and the square sample but that was done with ease.

The only shortcoming in the punching mechanism was in its assembly. Simply placing the guides into the lowering base and sliding down the punch did not work. There was misalignment of the guides and the punch locating plate that would prevent the punch from freely travelling up and down the guide. Pre-assembling the guides with the punch and then lowering the build onto its seats worked much better as the punch was able to freely slide.

Disassembling the mechanism was a trivial matter, whereas lifting the punch head off the cut sample had to be done with care. The user had to visually check when lifting the sample and the underlying rubber base was not being lifted also. The cut sample did tend to stick to the punch when required a steel spatula was passed through the head of the

punch and unto the prepared specimen to hold its position. The minimal force was used in this process as the punch would just slip out leaving the punch sample in position.

5.1.4 Transportation Card

The transportation card made what would be a tedious process to lift the specimen off the rake attachment jig onto the PBT into a simple process. The PLA polymer used provided more than enough stiffness and structural strength to prevent the loaded sample from being deformed or displaced during transportation. A brief of the transportation process is included in section 4.4.3, with images showing the card fitted onto the rakes and loaded onto the testing machine. What was not shown in that section was the intermediate step. When lifting the specimen of the cutting base, the square rubber matt would remain attached to the membrane tissue. A spatula had to be used to detach the rubber matt from the tissue. This usually left the sample elevated above the base of the hooks and out of the plane, which had to be lowered using the same Teflon wrapped spatula. Figure 5.2 was included to show the detachment of the rubber matt and the lowering of the specimen to the base of the hooks.

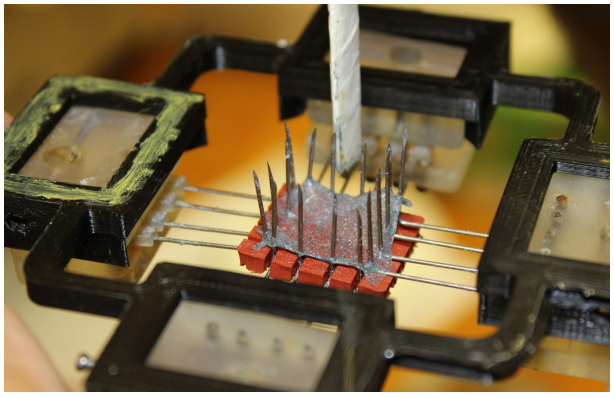

(a) Photograph of rubber matt being removed

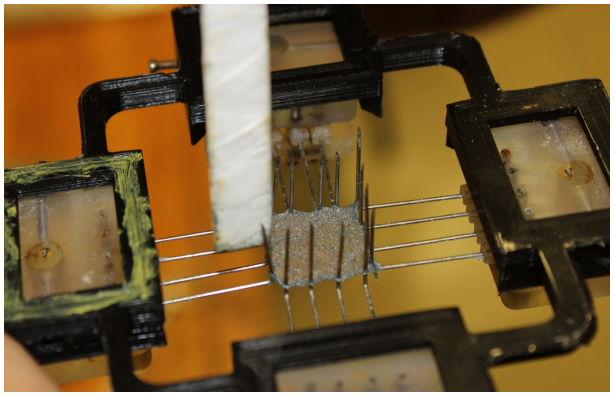

(b) Photograph of lowering sample

Figure 5.2 Photographs showing intermediate steps taken during the transportation of the sample

Overall the transportation card performed as designed, attaching onto the four rakes easily, holding these rakes securely in position and detaching from the rakes without disturbing the position of the hooks and the sample attached.

5.2 Assessment of Optical Measuring Technique

5.2.1 CPL Effect on Image Quality

Although the effect of the polarising effect has been discussed in chapter 4.1.1, this section aims to dive deeper by quantifying these changes. The images from Figure 4.5 were passed into an ImageJ processing tool, from which Hue-Saturation-Brightness (HSB) charts were plotted. These charts have been provided with their respective images in Figure 5.3. The most noticeable feature displayed in this figure was the removal of the secondary peak in the histogram. That peak shows the pixels that were exposed to saturated light and would result in a loss in correlation. Without the application of the CPL filters, the oversaturated region would travel across the ROI as the sample was inflated, preventing the DIC software from evaluating facet displacement.

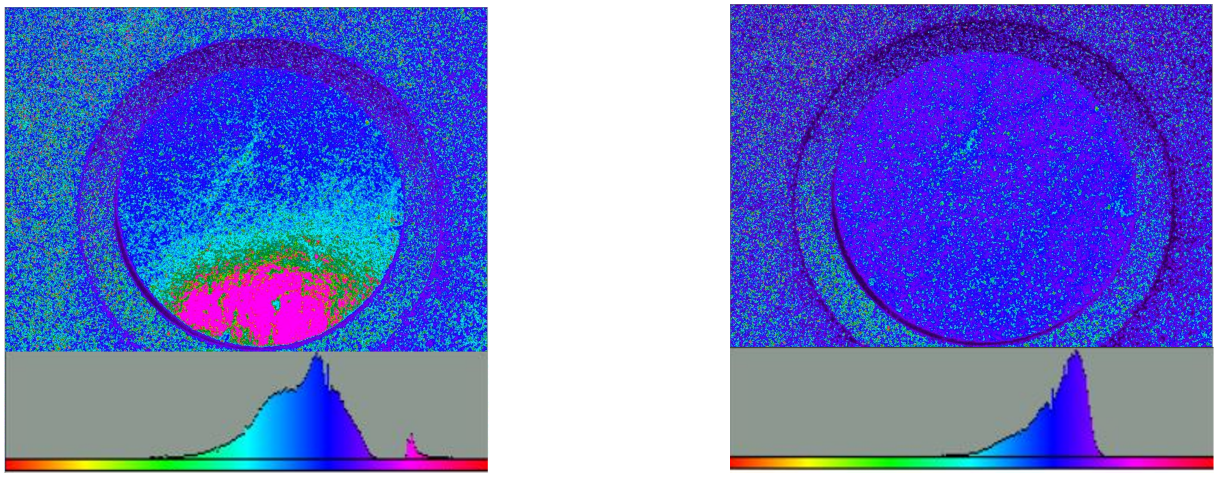

(a) Image captured with non-polarised filter

(b) Image captured with polarised filter

Figure 5.3 Differences between images taken with and without CPL filters with the aid of HSB color charts

To further emphasise the improvement the CPL filters had on the DIC equipment, Figure 5.4 has been included. Specimen 2 was tested before the decision was made to incorporate the CPL filters, providing a basis to compare the remaining samples. When comparing the two charts, Specimen 2 had pixels registered at the greyscale index of 255, indicating pixel overexposure whereas Specimen 8 did not have any pixels near that range. This quantitatively shows the polarising filters' effectiveness and ability to prevent harsh re-

flections from being picked up by the DIC cameras. The greyscale charts for the other tested specimens can be found in Appendix C.5.

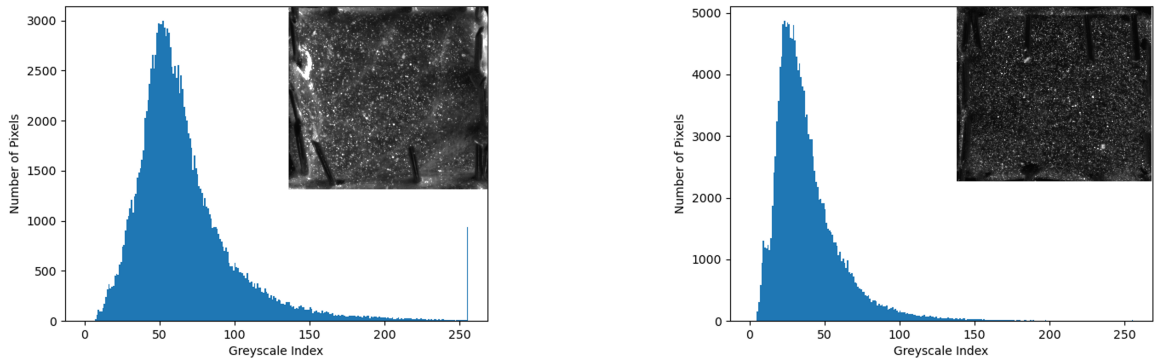

(a) Greyscale chart of Specimen 2 **(b)** Greyscale chart of Specimen 8

Figure 5.4 Comparison of Greyscale values obtained with and without CPL filters

5.2.2 Speckling with Multi-coloured Paints

Knowing that a shift was made away from using a single white paint to multiple different coloured paints, it was useful to try to analyse their differences, both qualitatively and quantitatively. To that extent, three samples were sprayed with different colour choices tabulated in Table 5.1. These specimens were then viewed under the DIC cameras, from which greyscale histograms were generated. In Figure 5.5 the three histograms were plotted on a single chart where the y-axis displays the distribution as a probability. The definitions of the legends are indicated in Table 5.1.

Table 5.1 *Description of colours used on samples*

Sample Key	**Paints used**
W	Matt white only
TPCW	Tidal blue, blush pink, charcoal black and matt white
TBW	Tidal blue, flat black and linen white

It was seen that both multicoloured samples were based in the lower band of the greyscale index, between 0 and 150 with a narrow and sharp distribution. This was unlike the single white paint, which had a much shallower and wider distribution of greyscale values. One of the findings in Pons [10] study was that a narrow distribution of greyscale values situated on the lower end of the spectrum performed better under DIC.

Discussing on a more qualitative note, when the experiments were performed multi-coloured specimens were easy to correlate and were completed with a 3D residuum value

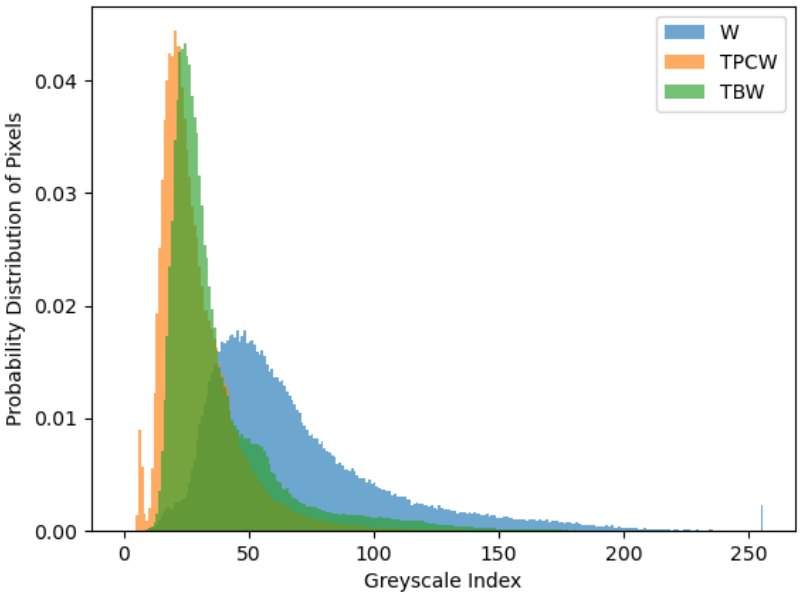

Figure 5.5 Greyscale values seen on different colour schemes

less than 0.04. The term 3D residuum is defined as the error in identifying a given facet in a series of pictures. According to the Dantec DIC training guide, a residuum value of less than 0.4 is a good target for acceptable accuracy. In contrast, when the white-speckled sample was tested the software would only be correlated with a residuum value of 0.99 which was very poor in comparison. This demonstrates that it was easier to achieve good DIC correlations when speckling with multiple colour paints, than staying with a single foreground colour (white).

5.3 Discussion of Experimental Results

5.3.1 MFA Identification and Isotropic Index

The main purpose of bulge testing the specimens was to identify the orientation of the MFA and CFA axis in preparation for the PBT testing. However, with the data that was captured an estimation of the sample's isotropy could be made. Figure 4.10 shows that the algorithm determines the radii of the minor and major axis from a reference configuration which was then used with Equation 5.1 to calculate the sample's isotropy index, as defined by Pons[10]:

$$\xi = \frac{r_{min} - r_{roi}}{r_{max} - r_{roi}} \tag{5.1}$$

where (r_{min}) and (r_{max}) refer to the minor and major radii and (r_{roi}) is the radius of the region of interest. Table 5.2 has the parameters for these variables tabulated with the evaluated (ξ) included for each sample as well.

Table 5.2 *Isotropic index from bulge tester*

Specimen No	r_{roi}	r_{min}	r_{max}	ξ
1	7.5	8.48	7.92	0.43
2	7.5	8.03	8.29	0.67
3	7.5	8.52	8.22	0.71
4	7.5	8.27	8.6	0.70
5	7.5	8.8	8.03	0.41
6	7.5	8.08	8.44	0.62
7	7.5	8.2	7.99	0.70
8	7.5	8.82	8.05	0.42
9	7.5	8.01	8.76	0.40

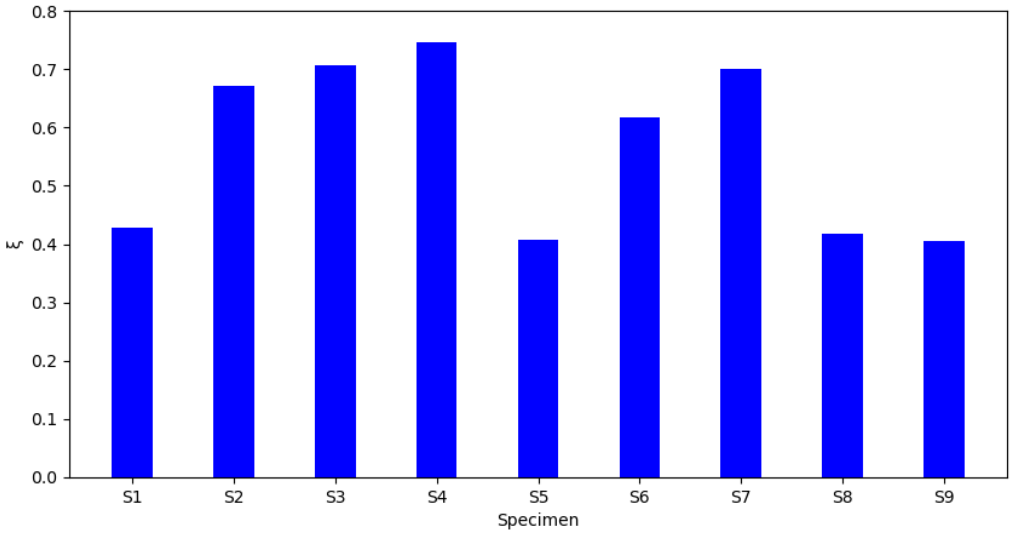

Figure 5.6 Bar chart showing isotropic index determined from bulge tests

Figure 5.6 provides a bar chart to visualise the variation in anisotropy across the different samples. S1, S5, S8 and S9 can be grouped together as "mildly anisotropic", while S2, S3, S4, S6 and S7 can be grouped as "mildly isotropic". The mean index value was found to be 0.56 ± 0.14. In Pons [10] isotropy study of SIS tissue, the average isotropy index for those samples was 0.55 ± 0.18, which matches what was found in this study.

5.3.2 Results From Cryo-histology

Thicknesses Measured

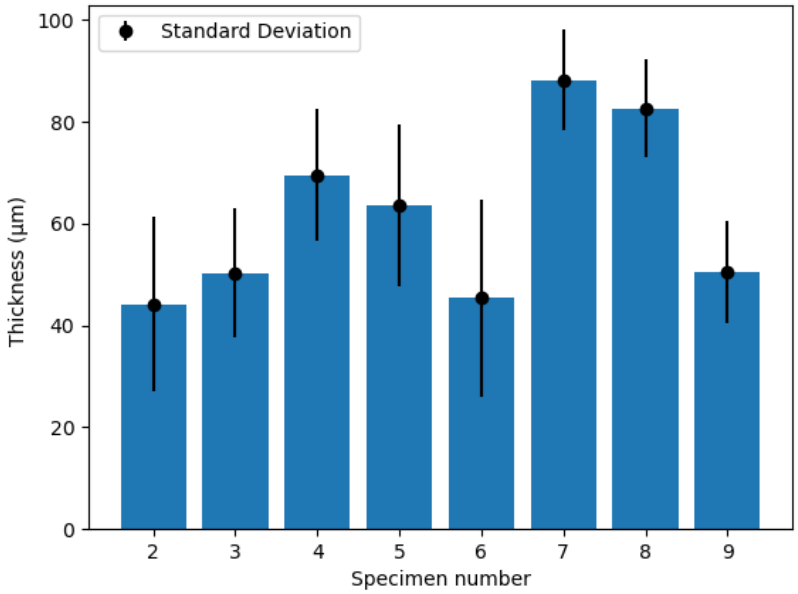

Figure 5.7 Bar chart showing thicknesses measured using cryo-histology

Of the 9 samples tested, only 8 were frozen to undergo a cryo-histology study where the thickness measured from these 8 specimens are shown in Figure 5.7. Using ImageJ as the processing tool, proved to be successful in identifying the boundaries of the cross-sectioned membrane and in taking a large volume of thickness measurements along its length. The error bars plotted in Figure 5.7 display the variation in thicknesses measured for each sample. Generally, the thickness of the sample ranged from 40 µm to 90 µm with a mean thickness of 61.7 µm.

Comparison between Wax-histology and Cryo-histology

Prior to this research, wax histology was the most recently used technique to preserve and measure the true thickness of the sample. Figure 5.8 presents a bar chart with the measurements taken using cryo-histology and wax-histology marked in blue and red respectively, to help evaluate which technique should be pursued in future.

It was noted that the thicknesses measured were vastly different between the cryo and wax techniques, where the largest thickness obtained for the cryo method (90 µm) did not overlap with the smallest value from the wax method (150 µm). While the SIS tissue for Pons' study was from a different batch to that used in this investigation, the difference in

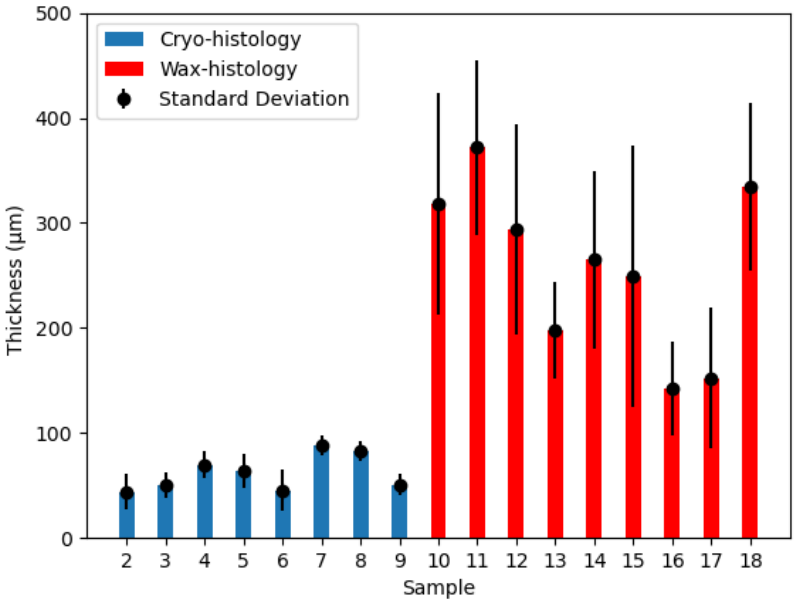

Figure 5.8 Bar chart comparing thickness measured between the two methods

mean thickness and spread of the data is substantial and merits further investigation. To better understand where the disparity stems from, tissue sections from Pons'[10] study were compared to those produced in this study in Figure 5.9.

The cryo-sectioned samples were found to be more compact with the fibres lying close to one another, whereas the wax-sampled tissue seemed to be a lot more frayed, with empty gaps between fibres. This indicated that the wax-preserved specimen may have dilated during the preserving technique thereby not preserving the in situ structure of the specimen. This leads to inaccuracy and uncertainty in measurement of sample thickness. This correlates with the large error bars in Figure 5.8 which indicated large variations in the extent to which these samples dilated. After studying both sets of thickness data and section images, it was clear that the cryo-histology technique better preserved the tissue structure and produced a more realistic representation of the true thickness of the membrane tissue.

5.3.3 Overview of Stress-strain Curves From PBT

For each specimen tested, two stress-strain curves were generated where one described the response along the MFA axis and the other the CFA axis. Data from the two load cells were used to infer the stress response along each direction and the DIC provided the strain measurements. Note that for these cases a mean strain response, averaging strain for all facets within the ROI, was used to define the strain response. As mentioned earlier,

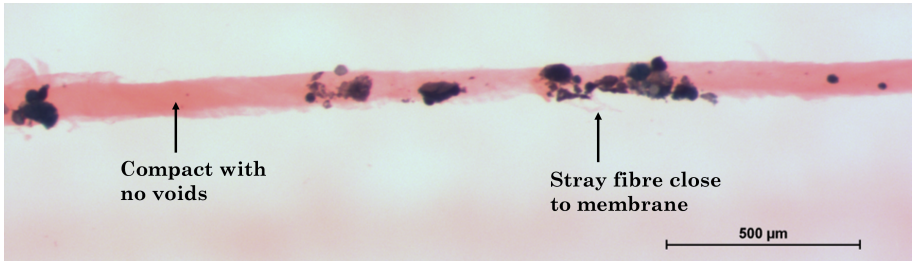

(a) Image captured of cryo-sectioned sample

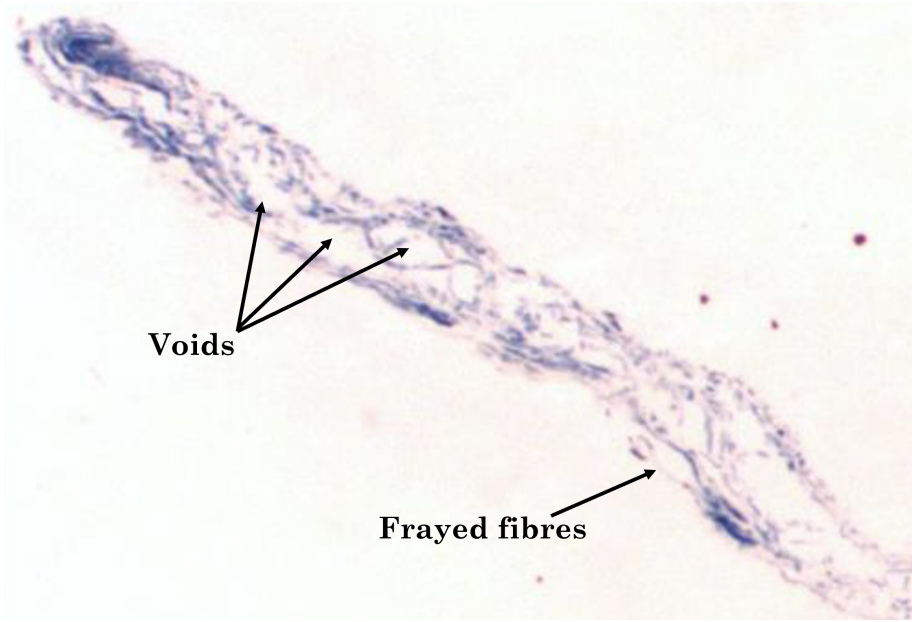

(b) Image captured of a wax-sectioned sample [10]

Figure 5.9 Visual comparison of specimens prepared under cryo and wax-histology method

the specimens were extended to 5 different ratios which were 1:1, 1:0.5, 1:0.75, 0.5:1 and 0.75:1.

The results obtained from Specimen 5 is displayed in Figure 5.10, where the MFA and CFA response are drawn in blue and green respectively. The first thing to note, was the behaviour of the MFA and CFA axis. Under the same extension, the stress recorded for the MFA was higher than that of the CFA which matched what was expected, as more fibres lay in the direction of MFA thus to achieve a given strain more load was required to extend those fibres. The other noticeable feature was the very low-stress response observed on at least one of the axis in the 1:0.5, 1:0.75, 0.5:1 and 0.75:1 extension ratios. This type of response was seen across all specimens tested and could not be used to draw any insights into the mechanical properties of the tissue. As such going forward only the 1:1 ratio was used to assess and evaluate the mechanical response of the samples. A library of the stress-strain responses for all the specimens is displayed in Appendix C.3.

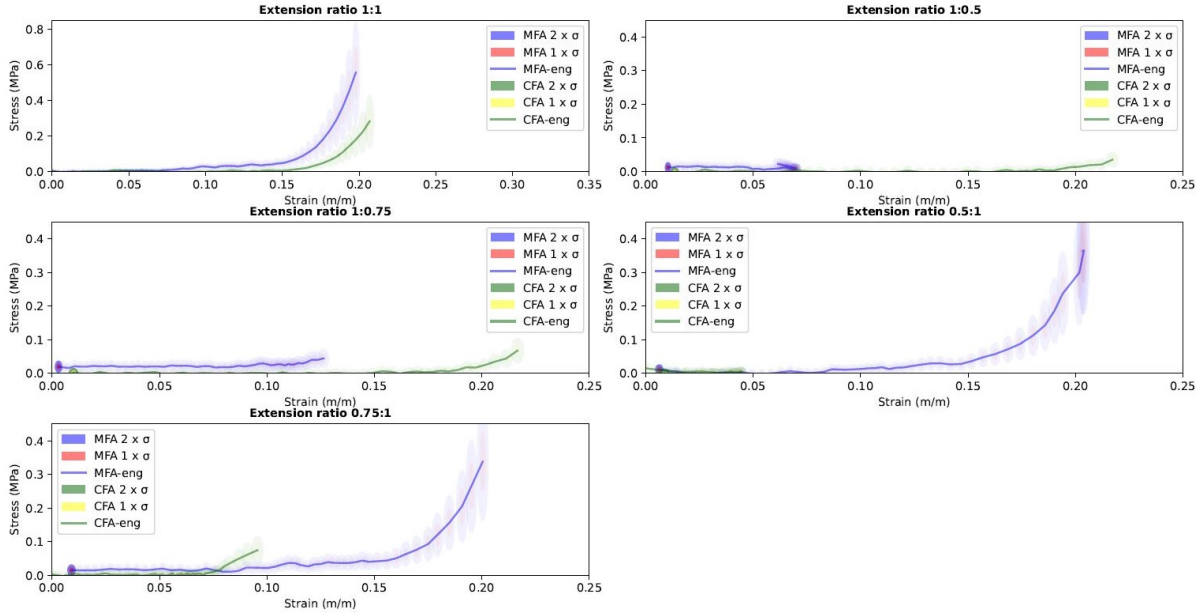

Figure 5.10 Specimen 5 PBT test results

From the set of samples tested and evaluated, two samples had to be disregarded for different reasons. Specimen 1 had to be excluded because it was part of the preliminary tests to see whether a successful test could be completed with the designed apparatus, and it was prior to the decision to use histology to measure sample thicknesses. During the PBT test for Specimen 2, the rakes swung erratically about the locating pins. This in turn affected the DIC measurements, yielding inconsistent strain data, leading to Specimen 2 being disregarded. Specimens 4 and 8, although not excluded, had their MFA and CFA axis misidentified. This may have been as a result of human error in the preparation step or the wrong angle of cut presented by the MFA algorithm. A check was performed by running the algorithm again and it was observed that the angle of cut was 90° off from the true angle of cut. Hence as part of their post-processing, the MFA and CFA data were swapped to account for this error.

To provide a more holistic view of the response of the SIS tissue, the CFA and MFA responses were compiled and plotted in separate graphs (see Figures 5.11 and 5.12). Looking at the CFA, the responses were closely grouped with only Specimens 3 and 9 appearing as outliers. In terms of their maximum stress achieved, all specimens aside from Specimen 4 rested between 0.5 MPa to 0.9 MPa.

The responses along the MFA were more spread out than those of the CFA, with Specimen 7 being a clear outlier. The typical "J" type shape occurred at strains ranging from 0.06 to 0.16 along the MFA, as compared to the 0.12 to 0.22 seen when looking at the CFA. This behaviour again correlates with that what is expected as the more fibre-dominant orientation should see faster increases in stress due to the increased stiffness.

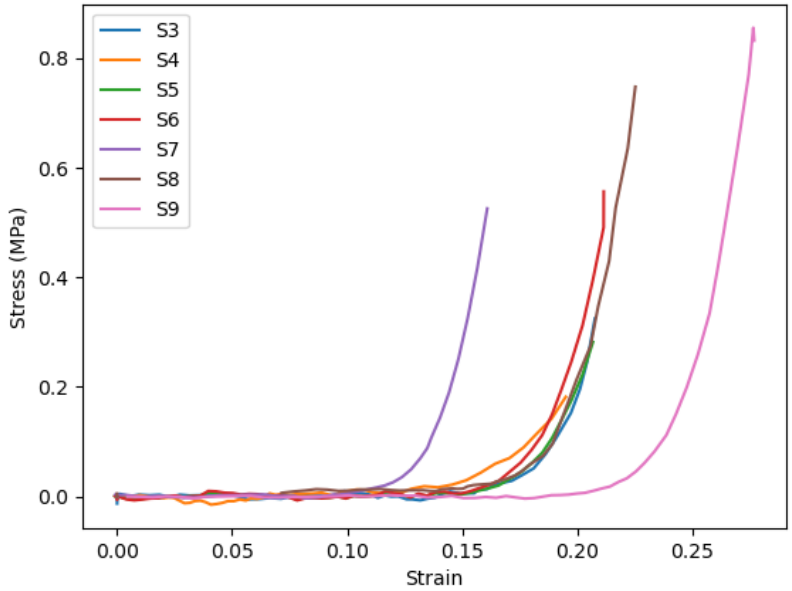

Figure 5.11 Compiled stress-strain response along the CFA axis

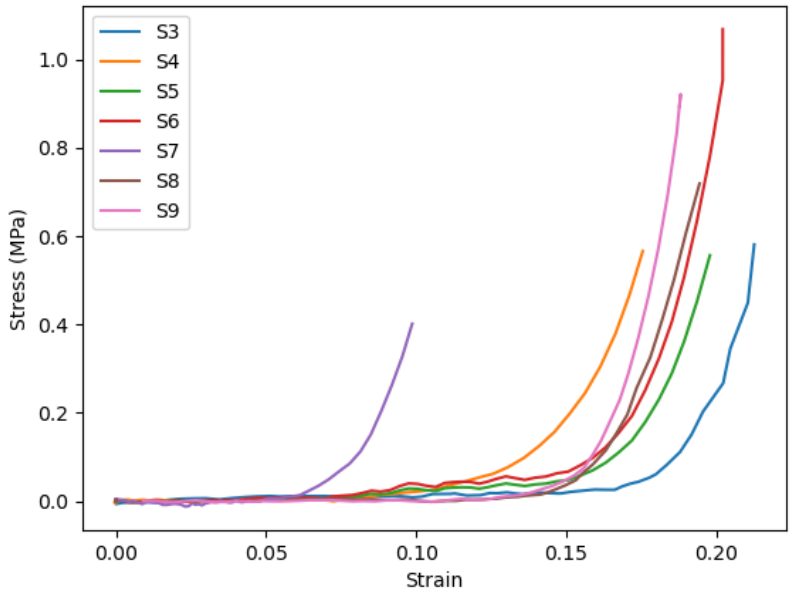

Figure 5.12 Compiled stress-strain response along the MFA axis

5.3.4 Discussion on Strain Induced During Bulge Testing

This section looks at the strain maps of the tested specimens captured at the moment when the sample was inflated to its maximum during the bulge test. The aim of this exercise was to check that the strains to which the samples were exposed prior to their test on the PBT machine did not exceed the "J" curve strain region across the square-shaped ROI. Figure C.2 and Figure C.3 show the principle strain along the horizontal (principle strain 1) axis and vertical (principle strain 2) axis, respectively, where the colour bar displays the strain in terms of mstrain (mm/m).

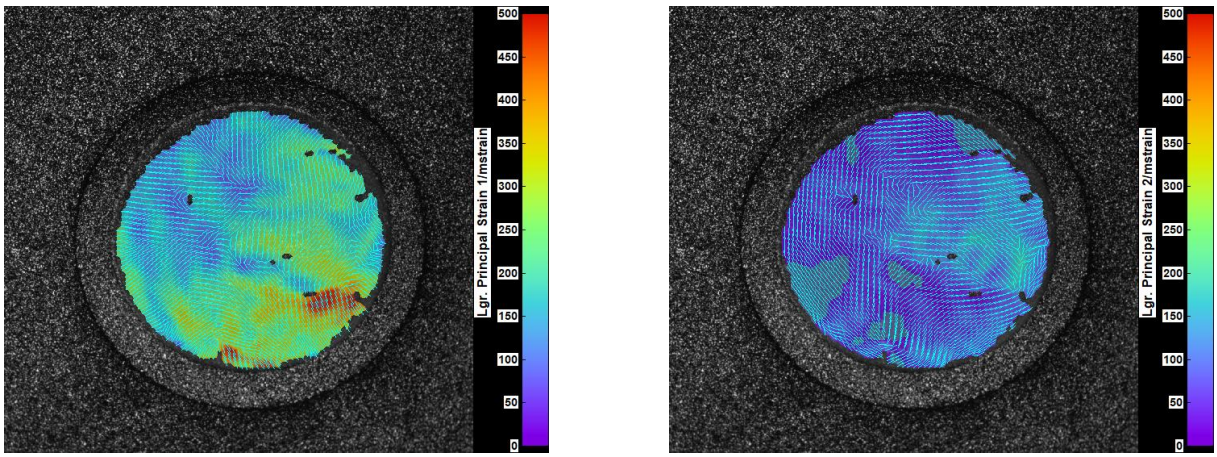

(a) Principle strain 1 **(b)** Principle strain 2

Figure 5.13 Image showing the principal strains recorded for Specimen 5 under maximum inflation

From the images captured, it was observed that across the ROI, the principle strain 1 and strain 2 values were in the range of 0.150 m/m to 0.250 m/m and 0 m/m to 0.150 m/m. These values, when compared to the strains recorded in the PBT stress-strain curves (refer to Appendix C.3), lie at the early stages of the J uptake, where the samples are still in their elastic range. This showed that the specimens in their preparation for the PBT test were not exposed to strains in the plastic range, and retained their structural integrity. There were regions where the strain values exceeded 0.4 m/m (refer to Figure 5.13a). In these regions, the tissue was in the plastic range. However, these regions lay outside the ROI and were not considered during the stress-strain analysis.

5.3.5 Out of Plane Displacement During PBT Tests

When conceptualising the clamping mechanisms, a desirable characteristic was to keep the tested samples planar under extension. It was not possible to limit out of plane displacement to the extent achieved by Caine [8]. There are multiple reasons that contributed to increase out of plane displacement. Firstly, the membrane tissue itself would sag under its

own weight on the hooks when fixed in position. Filling the bath with saline solution did help in lifting the specimen, but the sample still held a U-type shape. Secondly, manually lowering the specimen down the hooks during the transportation phase may have also been a contributing factor. Care was taken to ensure that the specimen was lowered to the same height on each of the rakes but this was not actively measured or controlled with tooling, so was dependent on the judgement of testing personnel. To display this behaviour an average of the out of plane displacement value was taken across the ROI and plotted against the time it took to extend the sample from rest to its full 1:1 extension ratio, as shown in Figure 5.14

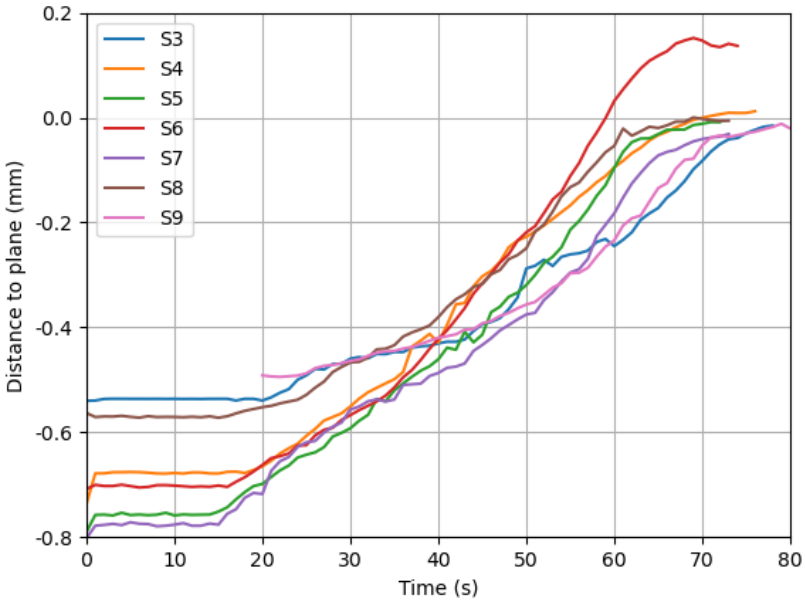

Figure 5.14 Compiled out of plane displacement observed for 1:1 extension ratio

As can be seen in Figure 5.14, the sample initially rested between 0.5 mm to 0.8 mm below the plane. Aside from Specimen 6, when under full extension the samples were lifted and brought up to within 0.5 mm of the plane. Caine [8], who designed and commissioned the PBT machine, defined that the maximum allowed out-of-plane motion should be restricted to 0.1 mm. This was based on the standard set in the BSI ISO 16482:2014 code, which applies to biaxial tensile testing of engineering metals. According to this standard, the tested samples only met this criterion when under full extension. However, given that the majority of tests were spent beyond the 0.1 mm limit, meant that the correction was not performed early and resulted in a failure in meeting this requirement.It should be noted that as tissues specimens are several orders of magnitudes more flexible than metals, this is an overly strict criteria but a standard has not been established.

5.4 Curve Fitting GOH Model

The stress-strain curves obtained from the biaxial tests were graphed and fitted to the GOH model [78] using an application called MCalibration [84]. The GOH model was chosen as the material model to curve fit because of its ability to cater for anisotropic, viscoelastic and incompressible characteristics, all of which are present in biological membrane tissue. It was also selected because of its availability in the ABAQUS finite element simulation software, making the parameters usable for future simulation work.

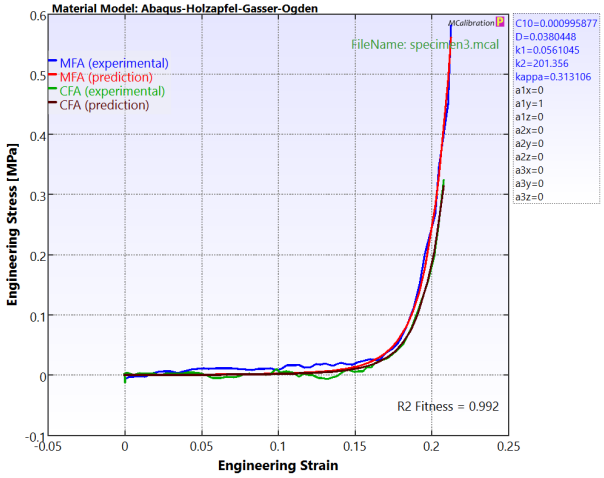

(a) Specimen 3

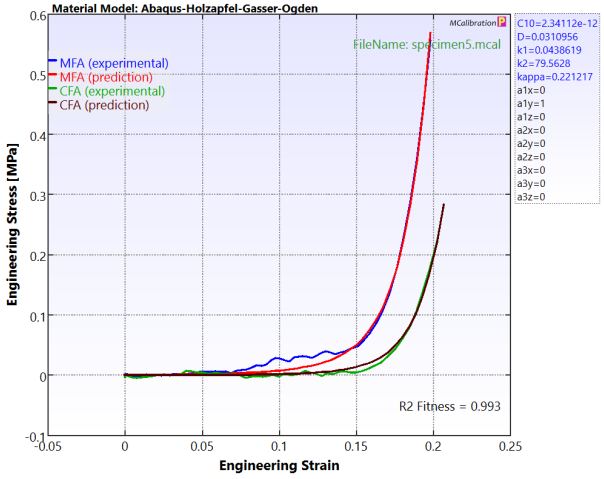

(b) Specimen 5

Figure 5.15 Graphs showing curve fitting of material model onto experimental results

Figure 5.15 shows the results of Specimen 3 and Specimen 5 after curve fitting the material model. The fitted material models are highlighted in black and the colours blue and green represent the MFA and CFA responses respectively. The complete set of curve-fitted results can be found in Appendix D. A summary of the extracted material parameters

from each specimen along with their respective R^2 fitness value has been included in Table 5.3. It was interesting to note that the mean R^2 fitness value was 0.993 and had a standard deviation of 0.003, depicting that a very good correlation was achieved.

Table 5.3 *Values obtained after curve fitting GOH model*

Name	$\mathbf{C_{10}}$	**D**	$\mathbf{k_1}$	$\mathbf{k_2}$	κ	$\mathbf{R^2}$
Specimen 3	9.96E-04	0.038	0.056	201.356	0.313	0.992
Specimen 4	1.74E-11	0.169	0.055	64.864	0.161	0.987
Specimen 5	2.34E-12	0.031	0.044	79.563	0.221	0.993
Specimen 6	1.40E-11	0.017	0.065	77.692	0.221	0.995
Specimen 7	4.32E-13	0.003	0.029	88.309	0.013	0.991
Specimen 8	3.69E-12	0.039	0.018	73.435	0.177	0.993
Specimen 9	4.95E-08	0.001	0.003	34.914	0.002	0.998
Mean	1.42E-04	0.043	0.039	88.590	0.158	0.993
STD Deviation	3.76E-04	0.058	0.023	52.584	0.114	0.003

From Table 5.3, it was seen that each GOH parameter had standard deviations of the same order of magnitude as their respective means, indicating substantial variation between specimens. The variable κ describes the dispersion of fibres (a measure of anisotropy) and ranges from 0 to $\frac{1}{3}$. $\kappa = \frac{1}{3}$ indicates a perfectly isotropic material, with decreasing κ indicating increasing anisotropy. $\kappa = 0$ would indicate all fibres perfectly aligned with a particular axis, and therefore minimal stiffness perpendicular to that axis. Over all seven specimens, κ had a mean of 0.158 and a standard deviation of 0.114.

Given that both κ and ξ (refer to section 5.3.1) describe anisotropy, although calculated differently, these parameters were then compared to better contextualise the parameters found from curve-fitting. Table 5.4 was built to qualitatively compare these two parameters by assigning the different ranges of values into one of three classes. A summary showing the ξ and κ values obtained for each specimen can be found in Table 5.5, with their cells highlighted according to their respective classification.

Table 5.4 *Classification of anisotropy*

Class	**Strongly Anisotropic**	**Mildly Anisotropic**	**Isotropic**
ξ	0 - 0.33	0.33 - 0.66	0.66 - 1
κ	0 - 0.08	0.08 - 0.25	0.25 - 0.33

Table 5.5 *Summary of ξ and κ values*

Specimen	**S3**	**S4**	**S5**	**S6**	**S7**	**S8**	**S9**
ξ	0.71	0.70	0.41	0.62	0.70	0.42	0.40
κ	0.31	0.16	0.22	0.22	0.01	0.18	0.00

Using Table 5.4, it was seen that κ on average described the material as "mildly anisotropic" behaviour, with cases of extreme anisotropy and isotropy also being observed. ξ, which was obtained from the bulge tested samples, were labelled from "mildly anisotropic" to "isotropic", with no samples lying in the strongly anisotropic range. Table 5.5 showed S4, S7 and S9 were grouped into different classes depending on which variable considered. For example S4, according to ξ was grouped as "isotropic", whilst κ grouped it as "mildly anisotropic" which highlighted showed that there was some variation between the two variables. S7 showed the most extreme case of this variation, where it was grouped as "isotropic" by ξ and "strongly anisotropic" by κ. S5, S6 and S8 were specimens, where ξ and κ grouped a given sample into the same class. While κ and Pons' isotropy index ξ are calculated differently, the different sensitivity to changes in CFA and MFA response was surprising. The sensitivity of these parameters to changes in input data are outside the scope of this project and are left for future research including numerical simulations. Ndlovu et al [85] warned of attributing good correlation to mean good material parameters were estimated. Ndlovu et al [85] noted that the curve fitting optimisation algorithm sets a new target value for each new set of data, resulting in convergence on a different set of material parameters.

Chapter 6

Conclusions and Recommendations

This dissertation aimed to design and build a clamping system that could be used to secure biological membrane tissue onto the existing planar biaxial tensile testing device at BISRU, along with a system for mounting a fragile specimen on the clamps at a pre-determined angle. After researching different clamping concepts, a rake-based system was chosen as a meaningful way to clamp membrane tissue. As such design requirements for the intended rakes were defined. Design requirements for the rake clamping system and specimen mounting apparatus were defined. The rake clamps and mounting apparatus were designed, built and commissioning tests were performed using SIS tissue. Planar biaxial tensile tests were conducted on SIS tissue following the experimental methodology and data processing procedure defined by Pons [10]. This chapter presents conclusions and provides recommendations based on the author's experiments and observations.

6.1 Novel Experimental Hardware Performance

6.1.1 Rakes

The novel rakes that were built and tested in this report met all its design requirements stipulated in section 3.3. The rakes provided a secure attachment to a biological membrane tissue testing at a desired angle when mounted on the PBT. During the transportation of the sample and under test conditions, the rakes were sufficiently rigid, with any deflection of the stainless steel hooks being recovered during unloading. The intended design feature of allowing the tissue to expand contra-laterally was also achieved, with the hooks swinging to facilitate the tissue expanding and contracting contra-laterally.

6.1.2 Rake Attachment Rig

The primary function of this device was designed to facilitate the process of attaching a sample at a specific orientation onto the hooks. Overall, this rig was functional and met its intended functional requirement. The rig functioned well in allowing the user to align the hooks along the MFA and CFA axis of the specimen. It was easy for the user to attach the hooks repeatedly and uniformly onto the specimen in the same location because of the inbuilt grooves and seats that accommodated the hook and their rakes. An additional benefit of this rig was that it was easy to carry and move around because it weighed less than 3 kg.

The drawbacks with this rig included the process of lowering a sample onto the protruding hooks and the transferring of the tissue onto the rubber matt. Lowering the sample onto the hooks was tedious because suitable fasteners were not used to secure a plated sample onto the lofted base, which resulted in the user having to hold these two components together to ensure that the sample would not separate and lose its orientation. When transferring the tissue, the user had to be careful and slow, so as not to dislodge the tissue from its hook nor damage it in the process. Maintaining the hydration level of the biological sample is important and any process that slows down sample transfer and mounting was undesirable.

6.1.3 Specimen Punching Rig

This mechanism was observed to provide a true and square-cut specimen for every sample that was punched. The guides and locating plate made it simple for the user to repeatedly produce the same sized and located square sample. The hardened punch itself remained sharp and did not experience visible damages such as edge rolling or edge chipping, over the course of testing. In summary, the punching rig met its functional requirements of producing a square geometry, with no notable shortcomings in its design.

6.1.4 Transportation Card

The transportation card worked well in transferring and loading a prepared sample onto the PBT device without disturbing the sample or the hooks unless moved by the user. As the card was both lightweight and sufficiently rigid, the user was able to hold the card with one hand freeing up the second hand for other purposes.

6.2 Improvements to Optical Deformation Measurements

This study introduced the use of CPL filters and speckling with multi-coloured paints to DIC measurements as practised at BISRU. The CPL filters removed the harsh reflections that would otherwise prevent the DIC software from evaluating facet displacement. Speckling the sample with multi-coloured paints helped in correlating the data and significantly reduced the 3D residuum value from 0.99 (observed when using white paint only) to less than 0.04.

It cannot be understated that the most difficult part of past PBT experiments was obtaining good DIC data at an acceptable residuum value. The main cause for a sample to be discarded post testing was problems with the DIC, related to unwanted reflections, poor lighting or poor speckling. The introduction of the CPL filters and the multi-coloured speckling technique mitigated all three of these factors which freed up the testing personnel to focus more on the aspects of material handling.

6.3 Thickness Measurements via Cryo-histology

Utilising cryo-histology to section and measure thicknesses of membrane tissue was found to be superior to the previously used wax-histology method. The wax-histology technique commonly produced membranes that had undergone tissue dilation, fibres fraying away and voids forming all of which led to inaccurate measurement of the sample in situ thickness. Images taken from cryo-sectioned tissue indicated compact samples with fibres lying close together, with minimal dilation or fraying. This offered a more realistic and accurate measurement of the samples' in situ thickness.

6.4 Constitutive Model Parameter Fitting

The exercise of curve-fitting the GOH model to the stress-strain curves was conducted successfully, with R^2 fitness values lying around 0.993 which indicated good correlation.However, the model parameters obtained should not be taken at face value without further investigation. In some specimens, the isotropic index measured experimentally and the GOH κ parameter, which is also a measure of isotropy, were not in good agreement. One measure might indicate the sample as being mildly to strongly anisotropic, while the other indicated a nearly isotropic sample. This, however, cannot be used to dismiss the parameters estimated and further investigation is required to conclude their accuracy.

6.5 Recommendations

Based on these findings, the following recommendations are made for future research:

1. The designed rake proved to be a successful concept and merits refinement of the design and fabrication. For thicker or stiffer biological tissues, the needle based hooks might need to be resized.

2. A study assessing the performance of these rakes to other clamping configurations should be conducted to identify which clamping method least influences the mechanical properties of a known material.

3. 3D printed polymer parts have sufficient strength and rigidity for testing biological tissue. The fabrication of 3D printed polymer parts was quicker and less expensive (from a labour perspective) than trying to machine metallic components. This should be exploited when designing any refinements to the testing apparatus.

4. The control system modifications to run the current PBT device in load control (not purely displacement control) should be investigated further, as all other aspects of the PBT are relatively mature.

5. Numerical simulations mimicking the PBT tests should be conducted using the GOH material parameters found in this report, with the aim of critiquing these parameters and identifying if the same mechanical response can be achieved.

References

[1] F. M. Hendriks, F. M. Hendriks & Author(s) F. M. Hendriks, "Mechanical behaviour of human skin in vivo - a literature review", *NAT.LAB. UNCLASSIFIED REPORT 820. PHILIPS RESEARCH LABORATORIES*, URL `http://citeseerx.ist.psu.edu/viewdoc/summary?doi=10.1.1.3.3641`.

[2] J. Hochberg, K. M. Meyer & M. D. Marion, "Suture choice and other methods of skin closure", *surgical.theclinics.com*, vol. 89, , pp. 627–641, URL `https://www.surgical.theclinics.com/article/S0039-6109(09)00035-8/abstract`.

[3] D. C. Salter, H. C. McArthur, J. E. Crosse & A. D. Dickens, "Skin mechanics measured in vivo using torsion: a new and accurate model more sensitive to age, sex and moisturizing treatment", *International journal of cosmetic science*, vol. 15, (1993), pp. 200–218.

[4] S. Diridollou, F. Patat, F. Gens, L. Vaillant, D. Black, J. M. Lagarde, Y. Gall & M. Berson, "In vivo model of the mechanical properties of the human skin under suction", *Skin Research and Technology*, vol. 6, (2000), pp. 214–221, URL `https://onlinelibrary-wiley-com.ezproxy.uct.ac.za/doi/full/10.1034/j.1600-0846.2000.006004214.x`.

[5] J. De Rigal & J.-L. Leveque, "In vivo measurement of the stratum corneum elasticity", *Bioengineering and the Skin*, vol. 1, (1985), pp. 13–23.

[6] H. Joodaki, J. Forman, A. Forghani, B. Overby, R. Kent, J. Crandall & O. Bostrom, "Comparison of kinematic behaviour of a first generation obese dummy and obese pmhs in frontal sled tests", 2015.

[7] G. W. Wood, M. B. Panzer, C. R. Bass & B. S. Myers, "Viscoelastic properties of hybrid iii head skin", *SAE International Journal of Materials and Manufacturing*, vol. 3, (2010), pp. 186–193.

[8] J. Caine, "Design and commissioning of planar biaxial tensile testing device for soft tissue", *UCT MSc Diss. 2022*.

[9] A. M. Curry, "Design, manufacture and commissioning of a low pressure quasistatic bulge tester for skin and membrane tissue", *UCT MSc Diss. 2020*.

[10] D. J. Pons, "Domes and crosses: Exploiting synergies in two methodologies for biaxial tensile testing of membrane tissues", *UCT MSc Diss. 2023*.

[11] K. Hayashi, "Mechanical properties of soft tissues and arterial walls", *Biomechanics of soft tissue in cardiovascular systems*, pp. 15–64.

[12] G. A. Holzapfel, "Biomechanics of soft tissue", *The handbook of materials behaviour models*, vol. 3, (2000), pp. 1049–1063, URL `http://www.cis.tu-graz.ac.at/biomech`.

[13] M. Geerligs, "Skin layer mechanics", *Eindhoven: TU Eindhoven*, URL `https://doi.org/10.6100/IR657803`.

[14] H. Oxlund, J. Manschot & A. Viidik, "The role of elastin in the mechanical properties of skin", *Journal of Biomechanics*, vol. 21, (1988), pp. 213–218.

[15] G. Limbert, "Constitutive modelling of skin mechanics", *Skin Biophysics: From Experimental Characterisation to Advanced Modelling*, vol. 22, (2019), pp. 19–76.

[16] C.W.J. Oomens, D.H. van Campen & H.J. Grootenboer, "A mixture approach to the mechanics of skin", *Journal of Biomechanics*, vol. 20, (1987), pp. 877–885.

[17] G. A. Holzapfel, "Biomech preprint series biomechanics of soft tissue", URL `http://www.cis.tu-graz.ac.at/biomech`.

[18] H. K. Graham, A. Eckersley, M. Ozols, K. T. Mellody & M. J. Sherratt, "Human skin: Composition, structure and visualisation methods", 2019.

[19] J. Gosline, M. Lillie, E. Carrington, P. Guerette, C. Ortlepp & K. Savage, "Elastic proteins: Biological roles and mechanical properties", 2002, URL `https://www.jstor.org/stable/3066845`.

[20] H. Joodaki & M. B. Panzer, "Skin mechanical properties and modeling: A review", *Proceedings of the Institution of Mechanical Engineers, Part H: Journal of Engineering in Medicine*, vol. 232, (2018), pp. 323–343.

[21] K. Langer, "On the anatomy and physiology of the skin 1. the cleavability of the cutis", *Br. J. Plast. Surg*, vol. 31, (1978), pp. 3–8, URL `https://ci.nii.ac.jp/naid/10024375341`.

[22] T. K. Tonge, L. S. Atlan, L. M. Voo & T. D. Nguyen, "Full-field bulge test for planar anisotropic tissues: Part i-experimental methods applied to human skin tissue", *Acta Biomaterialia*, vol. 9, (2013), pp. 5913–5925, URL `http://dx.doi.org/10.1016/j.actbio.2012.11.035`.

[23] R. B. Groves, S. A. Coulman, J. C. Birchall & S. L. Evans, "An anisotropic, hyperelastic model for skin: Experimental measurements, finite element modelling and identification of parameters for human and murine skin", *Journal of the Mechanical Behavior of Biomedical Materials*, vol. 18, (2013), pp. 167–180, URL http://dx.doi.org/10.1016/j.jmbbm.2012.10.021.

[24] A. Ni Annaidh, K. Bruyère, M. Destrade, M. D. Gilchrist, C. Maurini, M. Otténio & G. Saccomandi, "Automated estimation of collagen fibre dispersion in the dermis and its contribution to the anisotropic behaviour of skin", *Annals of Biomedical Engineering*, vol. 40, (2012), pp. 1666–1678.

[25] M. Ottenio, D. Tran, A. Ní Annaidh, M. D. Gilchrist & K. Bruyère, "Strain rate and anisotropy effects on the tensile failure characteristics of human skin", *Journal of the Mechanical Behavior of Biomedical Materials*, vol. 41, (2015), pp. 241–250.

[26] R. C. Haut, "The effects of orientation and location on the strength of dorsal rat skin in high and low speed tensile failure experiments", *Journal of Biomechanical Engineering*, vol. 111, (1989), pp. 136–140, URL https://asmedigitalcollection.asme.org/biomechanical/article/111/2/136/396789/The-Effects-of-Orientation-and-Location-on-the.

[27] G. W. Dombi, R. C. Haut & W. G. Sullivan, "Correlation of high-speed tensile strength with collagen content in control and lathyritic rat skin", *Journal of Surgical Research*, vol. 54, (1993), pp. 21–28.

[28] O. A. Shergold, N. A. Fleck & D. Radford, "The uniaxial stress versus strain response of pig skin and silicone rubber at low and high strain rates", *International Journal of Impact Engineering*, vol. 32, (2006), pp. 1384–1402, URL www.elsevier.com/locate/ijimpeng.

[29] J. Lim, J. Hong, W. W. Chen & T. Weerasooriya, "Mechanical response of pig skin under dynamic tensile loading", *International Journal of Impact Engineering*, vol. 38, (2011), pp. 130–135, URL http://dx.doi.org/10.1016/j.ijimpeng.2010.09.003.

[30] S. Bose, S. Li, E. Mele & V. V. Silberschmidt, "Dry vs. wet: Properties and performance of collagen films. part i. mechanical behaviour and strain-rate effect", *Journal of the Mechanical Behavior of Biomedical Materials*, vol. 111.

[31] F. Khatyr, C. Imberdis, P. Vescovo, D. Varchon & J. Lagarde, "Model of the viscoelastic behaviour of skin in vivo and study of anisotropy", .

[32] P Agache, "Collection explorations fonctionnelles humaines", *Physiologie de la peau et explorations fonctionnelles cutan{é}es*.

[33] A. Karimi, M. Haghighatnama, A. Shojaei, M. Navidbakhsh, A. Motevalli Haghi & S. J. Adnani Sadati, "Measurement of the viscoelastic mechanical properties of the skin tissue under uniaxial loading", *Proceedings of the Institution of Mechanical Engineers, Part L: Journal of Materials: Design and Applications*, vol. 230, (2016), pp. 418–425.

[34] G. Gabella, "The cross-ply arrangement of collagen fibres in the submucosa of the mammalian small intestine", *Cell Tissue Res*, vol. 248, (1987), pp. 491–497.

[35] S. Gunn, K. H. Sizeland, H. C. Wells & R. G. Haverkamp, "Collagen arrangement and strength in sausage casings produced from natural intestines", *Food Hydrocolloids*, vol. 129.

[36] L. Shi & V. Ronfard, "Review article biochemical and biomechanical characterization of porcine small intestinal submucosa (sis): a mini review", 2013, URL `www.IJBT.org`.

[37] A. Kalra & A. Lowe, "Mechanical behaviour of skin: A review", *Journal of Material Science Engineering*, vol. 5.

[38] A. S. Caro-Bretelle, P. N. Gountsop, P. Ienny, R. Leger, S. Corn, I. Bazin & F. Bretelle, "Effect of sample preservation on stress softening and permanent set of porcine skin", *Journal of Biomechanics*, vol. 48, (2015), pp. 3135–3141.

[39] A. Delalleau, G. Josse, J. M. Lagarde, H. Zahouani & J. M. Bergheau, "Characterization of the mechanical properties of skin by inverse analysis combined with the indentation test", *Journal of Biomechanics*, vol. 39, (2006), pp. 1603–1610.

[40] D. Batisse, R. Bazin & T. Baldeweck, "Influence of age on the wrinkling capacities of skin", *Skin Research and Technology*, vol. 8, (2002), pp. 148–154.

[41] A. Ní Annaidh, K. Bruyère, M. Destrade, M. D. Gilchrist & M. Otténio, "Characterization of the anisotropic mechanical properties of excised human skin", *Journal of the Mechanical Behavior of Biomedical Materials*, vol. 5, (2012), pp. 139–148.

[42] H. Eshel & Y. Lanir, "Effects of strain level and proteoglycan depletion on preconditioning and viscoelastic responses of rat dorsal skin", *Annals of Biomedical Engineering*, vol. 29, (2001), pp. 164–172.

[43] M. Lyons, D. C. Winter & C. K. Simms, "Mechanical characterisation of porcine rectus sheath under uniaxial and biaxial tension", *Journal of Biomechanics*, vol. 47, (2014), pp. 1876–1884, URL `http://dx.doi.org/10.1016/j.jbiomech.2014.03.009`.

[44] M. D. Ridge & V. Wright, "Mechanical properties of skin: a bioengineering study of skin structure", *Journal of applied physiology*, vol. 21, (1966), pp. 1602–1606.

[45] R. A. Macrae, K. Miller & B. J. Doyle, "Methods in mechanical testing of arterial tissue: A review", *Strain*, vol. 52, (2016), pp. 380–399.

[46] A. N. Natali, A. L. Audenino, W. Artibani, C. G. Fontanella, E. L. Carniel & E. M. Zanetti, "Bladder tissue biomechanical behavior: Experimental tests and constitutive formulation", *Journal of Biomechanics*, vol. 48, (2015), pp. 3088–3096.

[47] B. H. Ng, S. M. Chou & V. Krishna, "The influence of gripping techniques on the tensile properties of tendons", *Proceedings of the Institution of Mechanical Engineers, Part H: Journal of Engineering in Medicine*, vol. 219, (2005), pp. 349–354.

[48] D. F. Shi, D. M. Wang, C. T. Wang & A. Liu, "A novel, inexpensive and easy to use tendon clamp for in vitro biomechanical testing", *Medical Engineering and Physics*, vol. 34, (2012), pp. 516–520.

[49] D. J. Riemersa & H. C. Schamhardt, "The cryo-jaw, a clamp designed for in vitro rheology studies of horse digital flexor tendons", *Journal of Biomechanics*, vol. 15, (1982), pp. 619–620.

[50] Y. Lanir & Y.C. Fung, "Two-dimensional mechanical properties of rabbit skin—ii. experimental results", *Journal of Biomechanics*, vol. 7, (1974), pp. 171–182.

[51] A. Avanzini & D. Battini, "Integrated experimental and numerical comparison of different approaches for planar biaxial testing of a hyperelastic material", *Advances in Materials Science and Engineering*, vol. 2016.

[52] W. Sun, M. S. Sacks & M. J. Scott, "Effects of boundary conditions on the estimation of the planar biaxial mechanical properties of soft tissues", *Journal of Biomechanical Engineering*, vol. 127, (2005), pp. 709–715.

[53] R. J. Jaccodine & W. A. Schlegel, "Measurement of strains at si[U+2010]sio interface", *Journal of Applied Physics*, vol. 37, (1966), pp. 2429–2434.

[54] N. Reuge, F. M. Schmidt, Y. Le Maoult, M. Rachik & F. Abbé, "Elastomer biaxial characterization using bubble inflation technique. i: Experimental investigations", *Polymer Engineering Science*, vol. 41, (2001), pp. 522–531.

[55] J. Y. Sheng, L. Y. Zhang, B. Li, G. F. Wang & X. Q. Feng, "Bulge test method for measuring the hyperelastic parameters of soft membranes", *Acta Mechanica*, vol. 228, (2017), pp. 4187–4197.

[56] T. K. Tonge, "Micro-mechanical approaches for the hierarchical modeling of soft biological tissues; micro-mechanical approaches for the hierarchical modeling of soft biological tissues", 2014.

[57] S. D. Waldman & J. M. Lee, "Boundary conditions during biaxial testing of planar connective tissues. part 1: Dynamic behavior", .

[58] P. M. F. Nielsen, P. J. Hunter & B. H. Smaill, "Biaxial testing of membrane biomaterials: Testing equipment and procedures", *Journal of Biomechanical Engineering*, vol. 113, (1991), pp. 295–300.

[59] H. Fehervary, M. Smoljkić, J. Vander Sloten & N. Famaey, "Planar biaxial testing of soft biological tissue using rakes: A critical analysis of protocol and fitting process", *Journal of the Mechanical Behavior of Biomedical Materials*, vol. 61, (2016), pp. 135–151.

[60] N. T. Jacobs, D.H. Cortes, S. E. Szczesny, E. J. Vresilovic & D. M. Elliot, "Effect of boundary conditions on stress-strain uniformity in biaxial tension of annulus fibrosus", URL `http://mrlforums.sci.utah.edu/forums//project.php?projectid=1`.

[61] M. S. Sirry, "Computational biomechanics of acute myocardial infarction and its treatment", *UCT PhD Diss. 2015*.

[62] A. Avanzini & D. Battini, "Integrated experimental and numerical comparison of different approaches for planar biaxial testing of a hyperelastic material", *Advances in Materials Science and Engineering*, vol. 2016.

[63] A. Eilaghi, J. G. Flanagan, G. W. Brodland & C. R. Ethier, "Strain uniformity in biaxial specimens is highly sensitive to attachment details", *Journal of Biomechanical Engineering*, vol. 131.

[64] R. Jafar & M. R Labrosse, "Rigid rakes outperform hooks and pulleys as attachments in testing of anisotropic hyperelastic materials: experiments and simulations", URL `https://www.cellscale.com/wp-content/uploads/2019/03/BioTester%20White%20Paper%20-%20Rigid%20Rakes`.

[65] Z. Liu, K. Yeung & Z. Liu, "The preconditioning and stress relaxation of skin tissue", *Journal of Biomedical Pharmaceutical Engineering*, vol. 2, (2008), pp. 22–28.

[66] M. S Sacks, "Biaxial mechanical evaluation of planar biological materials", *Journal of Elasticity*, vol. 61, (2000), pp. 199–246.

[67] D.R. Veronda & R.A. Westmann, "Mechanical characterization of skin—finite deformations", *Journal of Biomechanics*, vol. 3, (1970), pp. 111–124.

[68] B. Kim, S. B. Lee, J. Lee, S. Cho, H. Park, S. Yeom & S. H. Park, "A comparison among neo-hookean model, mooney-rivlin model, and ogden model for chloroprene rubber", *International Journal of Precision Engineering and Manufacturing*, vol. 13, (2012), pp. 759–764.

[69] O. H. Yeoh, "Some forms of the strain energy function for rubber", *Rubber Chemistry and Technology*, vol. 66, (1993), pp. 754–771.

[70] R. J. Lapeer, P. D. Gasson & V. Karri, "Simulating plastic surgery: From human skin tensile tests, through hyperelastic finite element models to real-time haptics", *Progress in Biophysics and Molecular Biology*, vol. 103, (2010), pp. 208–216.

[71] R. W. Ogden, "Large deformation isotropic elasticity - on the correlation of theory and experiment for incompressible rubberlike solids", 1972, URL `https://about.jstor.org/terms`.

[72] Y. Fung, *Biomechanics: mechanical properties of living tissues*, Springer, 1993.

[73] W. Sun & M. S. Sacks, "Finite element implementation of a generalized fung-elastic constitutive model for planar soft tissues", *Biomechanics and Modeling in Mechanobiology*, vol. 4, (2005), pp. 190–199.

[74] Y. Lanir, "Constitutive equations for fibrous connective tissues", *Journal of Biomechanics*, vol. 16, (1983), pp. 1–12.

[75] J. A. Weiss, B. N. Makerc & S. Govindjeed, "Computer methods in applied mechanics and englneerlng finite element implementation of incompressible, transversely isotropic hyperelasticity", 1996.

[76] T. K. Tonge, L.M. Voo & T. D. Nguyen, "Full-field bulge test for planar anisotropic tissues: Part ii-a thin shell method for determining material parameters and comparison of two distributed fiber modeling approaches", *Acta Biomaterialia*, vol. 9, (2013), pp. 5926–5942, URL `http://dx.doi.org/10.1016/j.actbio.2012.11.034`.

[77] G. A. Holzapfel, T. C. Gasser & R. W. Ogden, "A new constitutive framework for arterial wall mechanics and a comparative study of material models", *Journal of Elasticity*, vol. 61, (2000), pp. 1–48.

[78] T. C. Gasser, R.W. Ogden & G. A. Holzapfel, "Hyperelastic modelling of arterial layers with distributed collagen fibre orientations", 2006.

[79] D. Zhang & D. D. Arola, "Applications of digital image correlation to biological tissues", *Journal of Biomedical Optics*, vol. 9, (2004), p. 691.

[80] D. Pillay, "Marking strategies for optical tracking of skin and biological membrane deformation", *UCT BSc Eng Rep. 2019*.

[81] W. S. LePage, S. H. Daly & J. A. Shaw, "Cross polarization for improved digital image correlation", *Experimental Mechanics*, vol. 56, (2016), pp. 969–985.

[82] M. Simson, "What is cross polarization and how you can use it in your photography - diy photography", 2021, URL `https://www.diyphotography.net/what-is-cross-polarization-and-how-you-can-use-it-in-your-photography/`.

[83] D. E. Maidana, S. Notomi, T. Ueta, T. Zhou, D. Joseph, C. Kosmidou, J. M. Caminal-Mitjana, J. W. Miller & D. G. Vavvas, "Thicknesstool: automated imagej retinal layer thickness and profile in digital images", *Scientific Reports*, vol. 10, (2020), p. 18459.

[84] "Mcalibration", 2022, URL `https://polymerfem.com/`.

[85] Z. Ndlovu, D. Desai, T. Pandelani, H. Ngwangwa & F. Nemavhola, "Biaxial estimation of biomechanical constitutive parameters of passive porcine sclera soft tissue", *Applied Bionics and Biomechanics*, vol. 2022.

[86] A Klein, "3d print a magnetic switch, and how it works", 2019, URL `https://www.youtube.com/watch?v=n9tZIFfM14o&ab_channel=AndrewKlein`.

Appendices

Appendix A

Preliminary Design Concepts

This section provides a brief of early concepts that were designed and built. However, these concepts were deemed unsuitable for numerous reasons but provided the author key insights for subsequent designs.

A.1 Specimen cutting rig

One of the first major hurdles that had to be overcome was the process of excising a square shaped tissue in a consistent and repeatable manner. The first concept was heavily inspired by the tool designed by Pons [10] and is illustrated in Figure. The tool consisted of a 3D printing part with four slits that each held protruding razor blades. The slits were orientated such that the razor blades would connect to form a square shaped geometry that would be the outline of the specimen. A cutting base was also designed that also had slits to accommodate the blades when they were driven down by the user

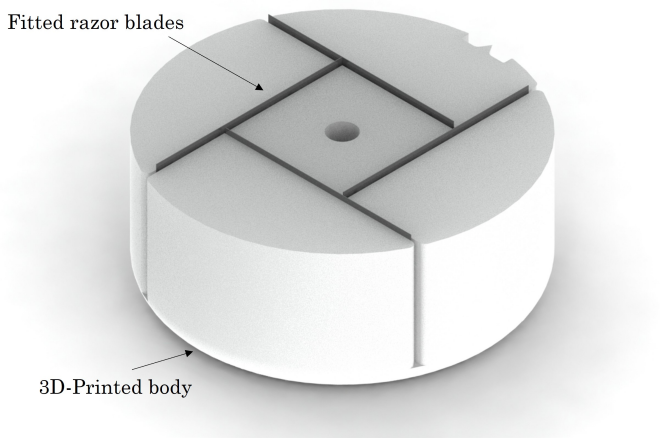

Figure A.1 Rendered image of the cutting tool

The idea was that the membrane tissue would be placed on a cutting base,a cover would then be placed on top to secure the tissue in position, thereafter, the cutting tool would be seated on top of the specimen and pressed down by the user to force the blade to cut through the tissue. Note that the cutting base which was made from PLA was designed with grooves to accommodate the blades during the cutting operation. Figure shows a general assembly of this cutting rig.

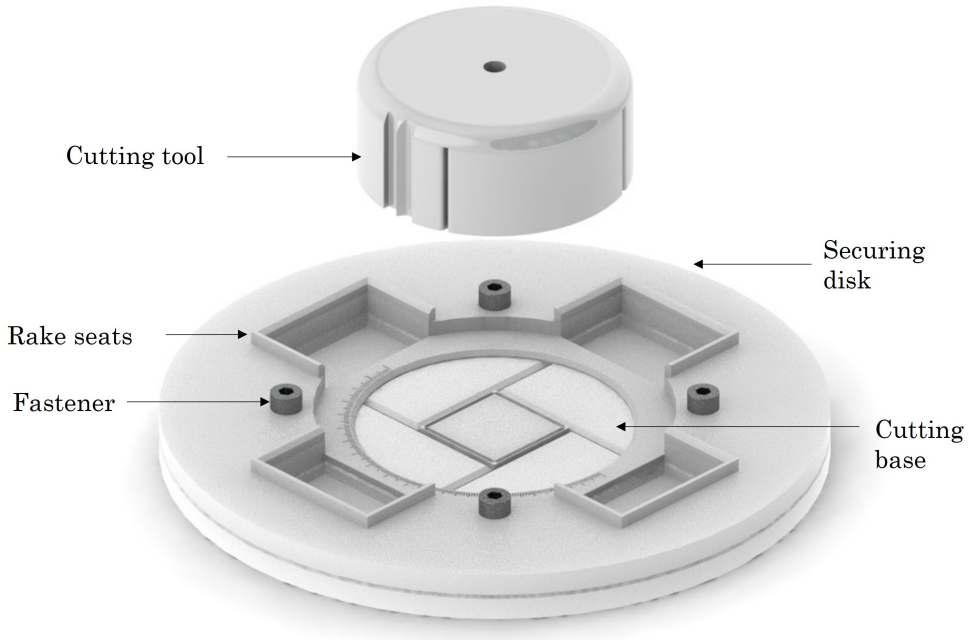

Figure A.2 Rendered image of the cutting rig

There were major flaws discovered when this prototype was built and tested. Most notably was that the cutter failed to cut the tissue at all. The tissue was seen to wrap around the razor blades and slide into the grooves without being sheared. The plastic base was swapped with a rubber base, with the idea that the blades would pass through the tissue and into the matt providing minimal chance for the tissue to wrap around the blade. This did not lead to any improvements. The razor blades began to tilt and warp when pressed down upon and did not provide any clear cuts. Another issue was that the although the desired shape was a closed of square, this could not be achieved as there were gaps at the interface where two blades met. This meant even if this cutting tool succeeded in excising the tissue, the user would still need to cut at the four edges to form a square that too without disturbing the tissue.

Given these findings, it was obvious that another means to cut the tissue had to be found. The following concept was based on a punching die which was used to excise circular disks from a rubber matt. A 35 mm round punch was used to see if a circular specimen could when the sample is placed on a plastic surface. A hammer was used to impart an impact load onto the punch. The first attempt saw the punch travel through

the both the specimen and the plastic base, with the main positive being that a clean cut was produced. Figures provides photographs of this test being conducted.

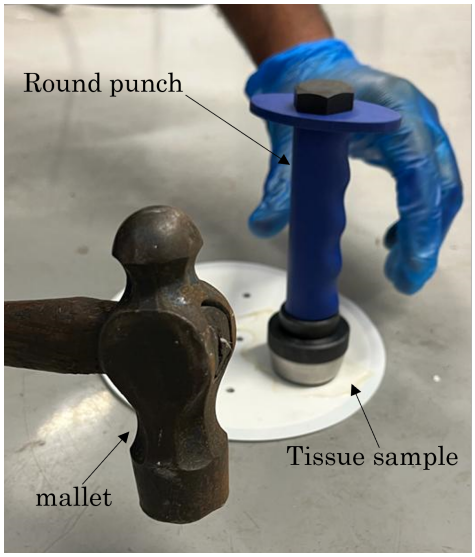

(a) Photograph of round punch being tested

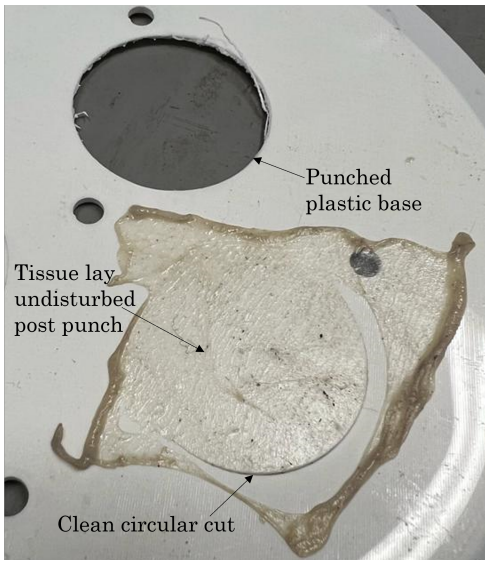

(b) Photograph showing the results after punching

Figure A.3 Photographs showing the punch being tested and the result after punching

The fact that a clean cut was observed gave enough evidence to move forward with this punching concept. As a result, a square punching die was machined out of M300 steel with the foresight that this steel may need to be hardened to increase its durability. The square die was tested to check whether it worked as desired and sure enough the die cut through the specimen and the plastic to give a square shaped specimen. Figure shows photographs of the die fitted onto its punching handle, the die with the excised shaped embedded in it and the cut square tissue.

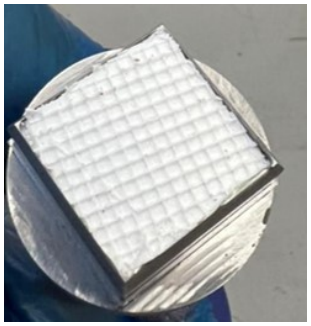

(a) Embedded sample

(b) Punched material

(c) Blunted die

Figure A.4 Photographs showing the square punch post test, the square sample produced and the wear on the die

The only concern remaining was on the durability of the die and how to prevent the punched material from sticking into the die. After a couple of uses of the die the sharpened edges had begun to blunt and some edges had started to roll over. The answer to this problem was to heat treat the die such that the material would hardened and be more resistant to blunting. Preventing the material from embedding into the die was a more simpler solution, it just required that the edges of the blade be sharpened using polishing paper. This allowed a much cleaner cut and hence cause the excised material from sticking against the die.

A.2 Rake attachment prototype

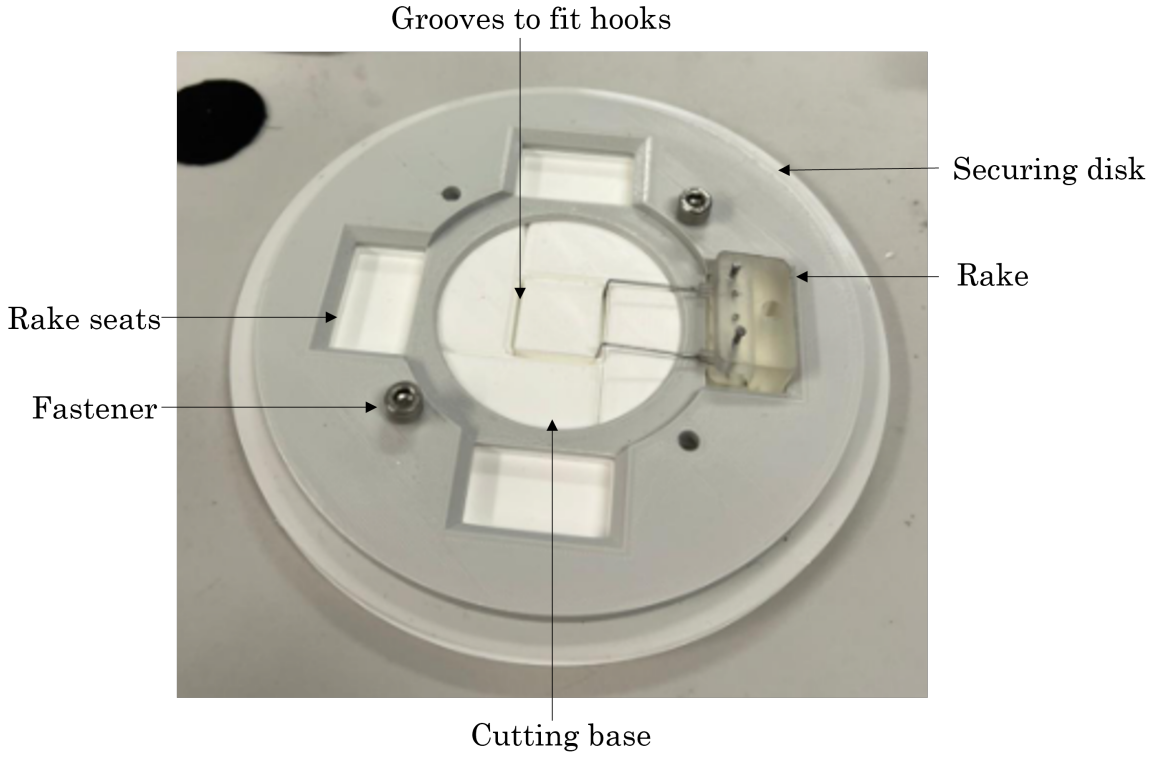

Figure A.5 Photograph of rake attachment rig prototype

Shown in Figure was the concept built to hook the rakes onto the specimen. The working concept was that after the sample was cut using the cutting tool (see Figure A.1), rakes would be individually lowered into their seats and in doing so the downward facing hooks would pierce and attach themselves to the specimen. Once all the rakes have been attached a tool would then be used to lift the rakes and sample together to be transported to the PBT machine.

Similar to the cutting tool, when this concept was built and tested, numerous design flaws were discovered. Most notably was that the hooks failed to pierce the specimen when the rakes were lowered into their seats. Due to the tissue being hyper-elastic, it would stretch

and deform with the hooks indenting into it without being punctured through. Attempts were made to individually press the hooks into the tissue, but there was not enough space beneath the specimen to drive the hook through. Also noted was that the specimen would stick to the base plate, making it impossible to lift the specimen without the use of a pair of tweezers. Given that the hooks were all downward facing, in the event that the specimen were to be lifted the tissue would prefer to be stuck to the base and the tissue would simply slip off the hooks they were attached to. These findings led the author to abandon this concept and rethink their approach to this problem.

The next concept relied on the principle that the specimen would lowered onto the hooks, unlike the previous concept. With this idea, a platform that could seat a series of protruding hooks was designed. The height of this platform was set to allow the hooks to protrude at least 10 mm above it. To lower the tissue, the sample was spread onto a metal disk which had a circular opening that would slide over the platform and thereby force the sample onto the hooks. Figure shows a photograph of this concept being tested.

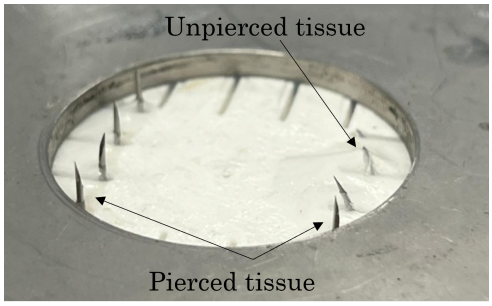

(a) Sample lowered onto the platform

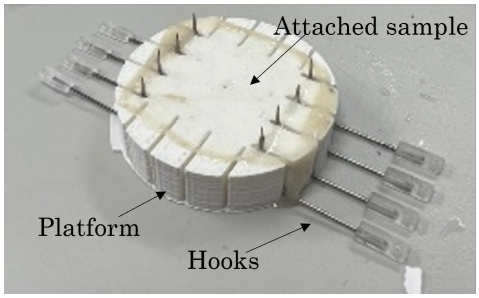

(b) Sample attached to the hooks

Figure A.6 Photographs showing sample lowered onto the platform and attached to the hooks

The test showed that with this configuration the tissue would be pierced by the hooks. There was the need to use a spatula to force some of the tissue to be pierced all the way through, but this was deemed as an extra step that would have to be taken. An added benefit from using this configuration was that because the hooks were now facing upwards, lifting the sample was made much simpler as the tissue would rest against the horizontal part of the hooks and detach itself from the plastic base.

A.3 Transportation tool

The first transportation tool that was designed was based on the work performed by Klein [86]. Klein [86] had previously built a tool that used magnetism to attract ferritic materials to it, that could then be transported as required. Figure A.7 shows the design of this transportation tool with a sectioned view given as well. The tool consisted of two halves,

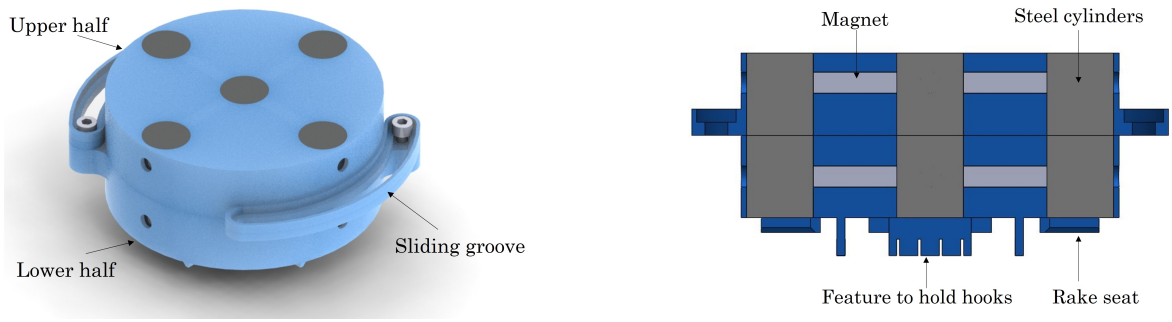

(a) Isometric View **(b)** Section View

Figure A.7 Illustration showing isometric and section views of the transportation tool

where each half held five steel cylinders and four neodymium magnets. These magnets lay horizontally with neighbouring pairs seated such that their polarity was opposite to it. The two halves were connected using two socket screws with enough clearance to allow them to rotate about its axis. With this arrangement the user is able to control the direction of the magnetic field, by rotating the upper half relative to the lower half. Where in one configuration the magnetic field offers no attractive force to external ferritic material and vice versa. A diagram showing the arrangement of these two configurations are shown in Figure A.8. There was no doubt that this tool would not function as designed because it

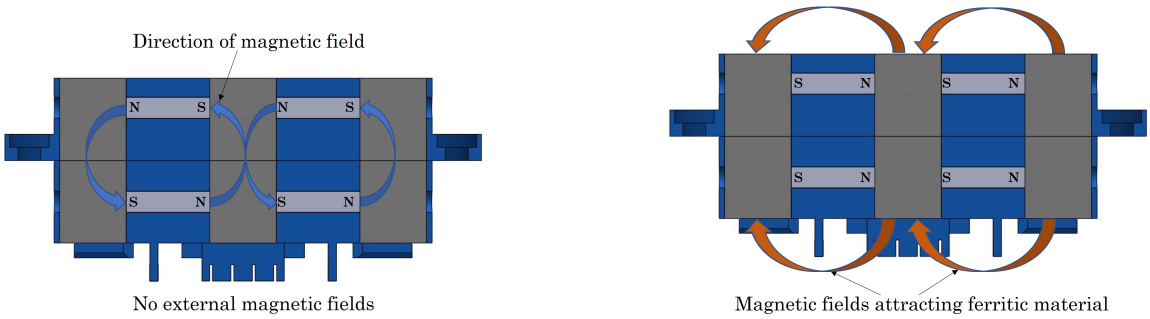

(a) Switched off **(b)** Switched on

Figure A.8 Diagram showing the configuration for the transportation to be switched off and on

is a commonly used component in industry. However, because of its bulky nature, its size relative to the carrying piece and the lack of visibility the user would have when seating this device with the rakes attached onto the PBT machine made it unfit for the purpose of this experiment. Hence an alternative more simpler solution had to be found.

Appendix B

Casting Process and Sleeve Heights

B.1 Casting rubber mat

The mould used to cast the rubber base consisted of an upper-half and lower-half, as shown in Figure B.1. The lower-half held all the polymer mixture, with the upper half supplying vents for air and excess material to escape from.

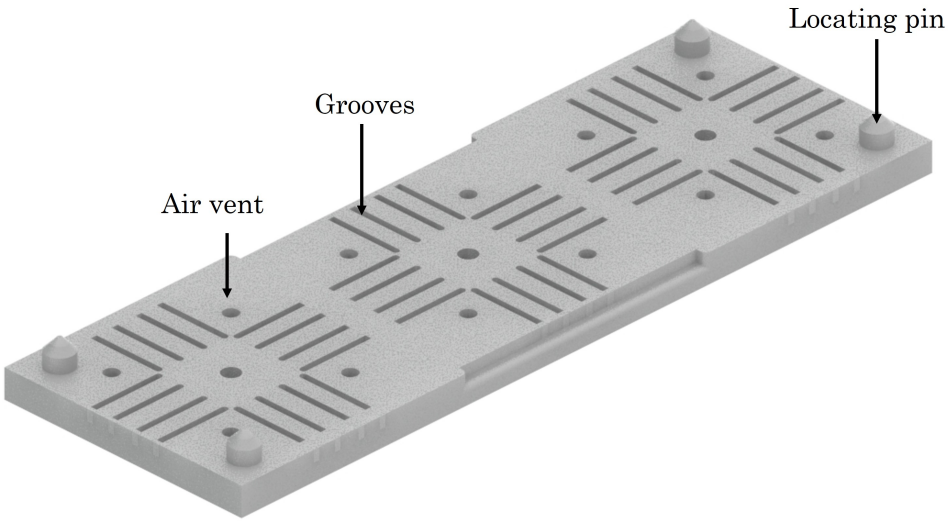

(a) Upper-half

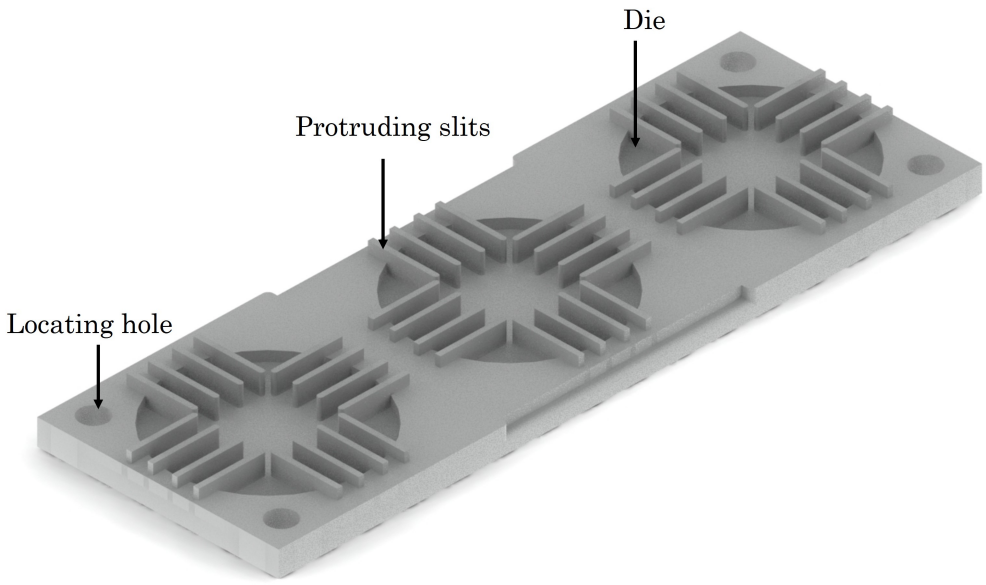

(b) Lower-half

Figure B.1 Illustration of the upper-half and lower-half of the mould

To cast the rubber mat, the following steps were followed:

- The surface of the moulds were wiped down with isopropanol and left to dry
- A release agent was then applied to the die area so that it would be easier to release the cast matt from the mould
- The MoldMax60 containers labelled Part A and Part B were then stirred individually
- A cup was then placed on a scale and 40 g of Part A followed by 1.2 g of Part B was poured into it. The mixture was then stirred for 3 min
- Using a wooden spatula, the mixture was poured into one half of the mould and care was taken that all three dies were completely filled.
- The filled mould was then placed in a vacuum degassing machine to removed any air trapped in the mixture. This usually took around 2 min to release most of the trapped air.
- The mould was then removed from the degassing machine and placed on a flat surface. The upper-half mould was then mounted onto the lower-half, and pressed down upon by a heavy mass placed onto of the upper-half mould
- The mould was then left to cure for a duration of 24 h, after which the moulds were separated to release the three cast mats and any excess material was excised off.

Figures B.2 B.3 and B.4, all show photographs of the final steps of removing the cast rubber mat.

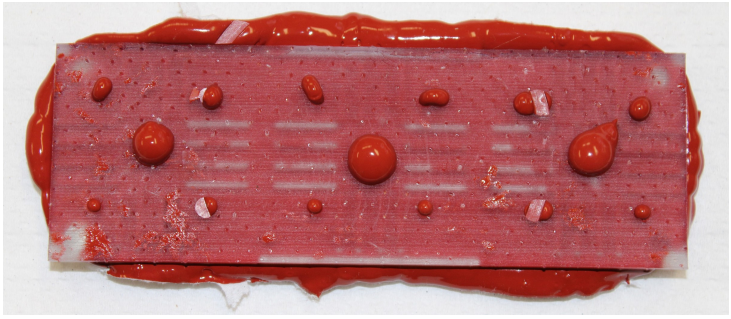

Figure B.2 Image of mould after overnight curing

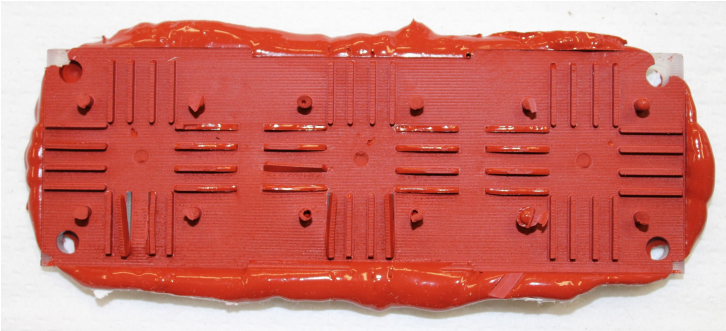

Figure B.3 Image taken after removal of the upper-half mould

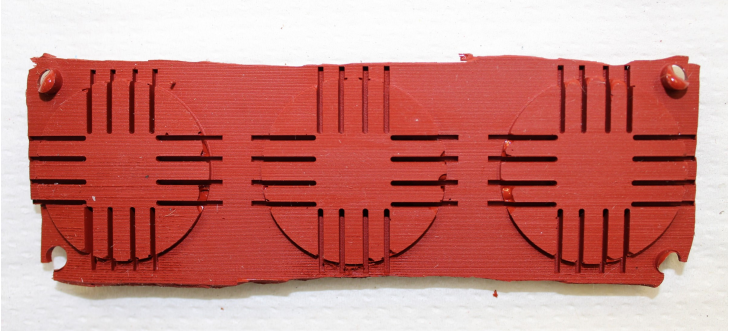

Figure B.4 Image of the cast rubber mats with excess material

B.2 Sleeve Heights

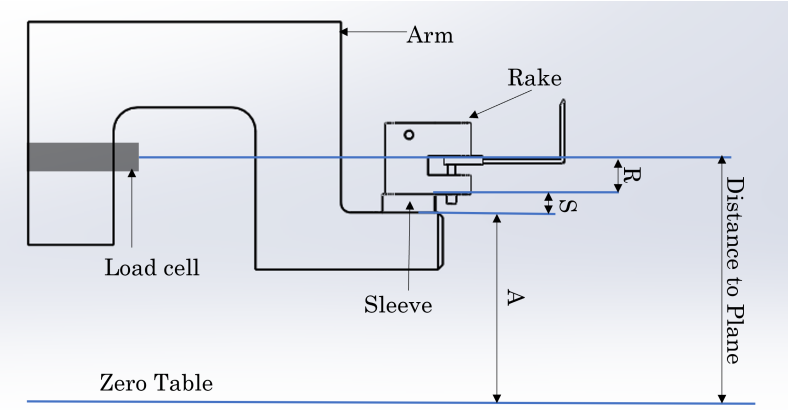

Figure B.5 Diagram showing sleeve fitted onto arms

Individual sleeves had to be fabricated using an FDM printer to bring the rakes up to lie along the same plane as the load cell. The aim was to minimise any bending stress being applied to the load cell. The PBT machine was placed on a zero table, where the distance of each arm relative to the base (A) and the distance of the load cell relative to the ground was measured using a height gauge. Figure B.5 shows a diagram of an arm fitted with its sleeve and rake, where labels R and S refer to the height of the hook relative to the

sleeve and the height of the sleeve. The distance to plane was measured to be 114.98 mm. Table B.1 provides a summary of the arm heights measured (A) along with the respective sleeve heights needed to bring the rakes all onto the same plane. Note that the distance to plane and R were measured to be 114.98 mm and 9.20 mm respectively.

Table B.1 *Summary of sleeve heights associated with each arm*

	Heights / mm		
Name	**A**	**A+R**	**S**
Arm1	104.16	113.36	1.62
Arm2	104.26	113.46	1.52
Arm3	101.89	111.09	3.89
Arm4	101.56	110.76	4.22
Distance to Plane	114.98		

Appendix C

Comprehensive experimental results

C.1 Bulge-test results

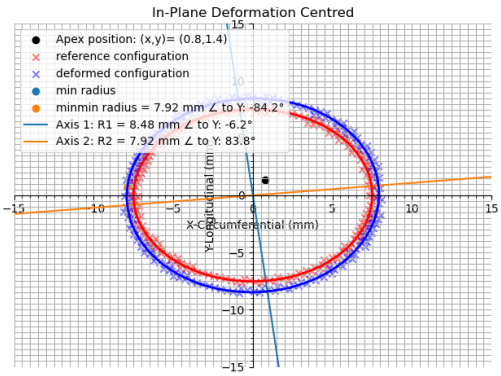

(a) Specimen 1

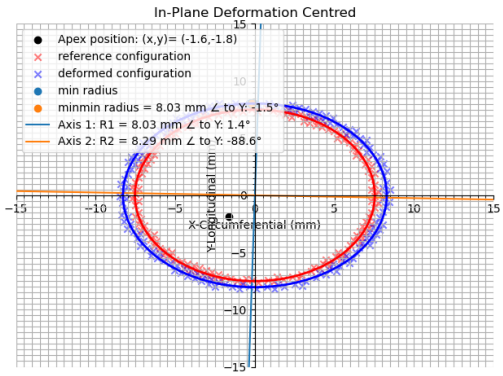

(b) Specimen 2

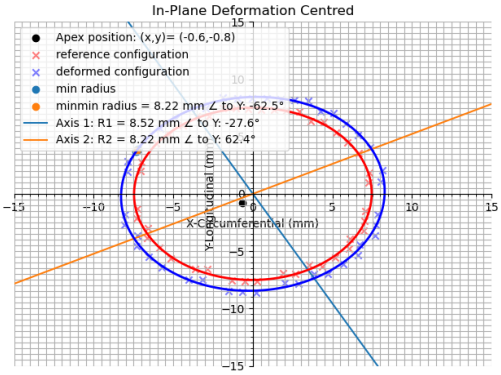

(c) Specimen 3

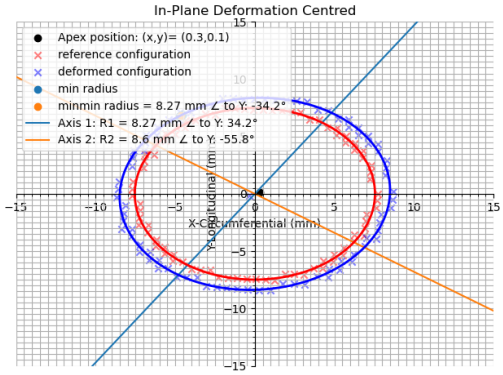

(d) Specimen 4

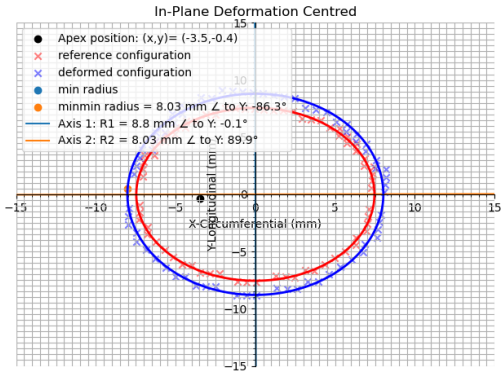

(e) Specimen 5

Figure C.1 Results obtained from Bulge tester for the first four specimens

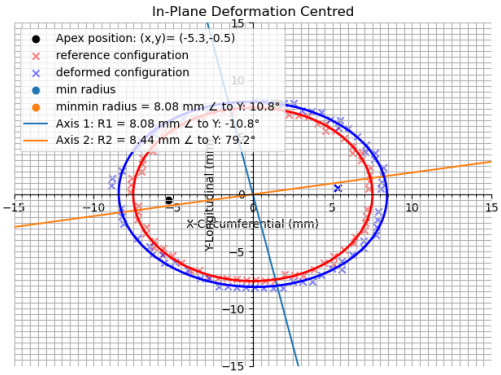

(f) Specimen 6

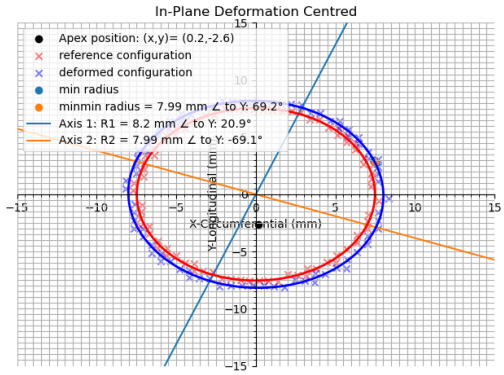

(g) Specimen 7

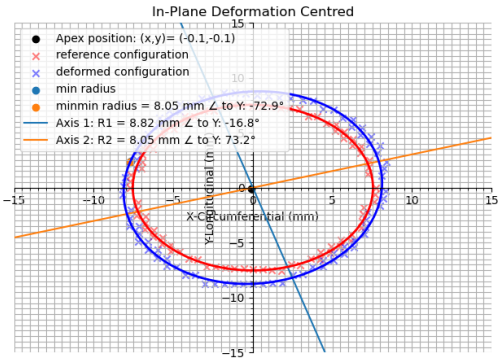

(h) Specimen 8

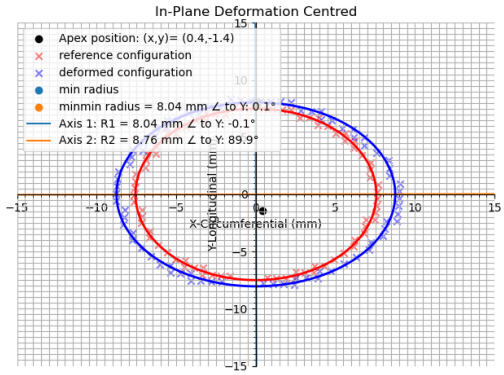

(i) Specimen 9

Figure C.1 Results obtained from Bulge tester for the remaining three specimens

C.2 PBT Video Recordings

Video recordings of Specimen 2 and Specimen 5 undergoing PBT tests has been provided in the links below:

- Specimen 2
  `https://drive.google.com/file/d/1VQk7xT08EPMyv4JVdyRbyy7AtrB5qHgH/view?usp=sharing`

- Specimen 5
  `https://drive.google.com/file/d/1TIQxV2X8us07gUjcacgCp9PjoSnzXJix/view?usp=sharing`

where the Specimen 2 video, shows the rakes swinging which lead to a poor strain measurements, and Specimen 5 shows footage of a normal PBT test.

C.3 Stress-strain curves

Specimen 1 HE

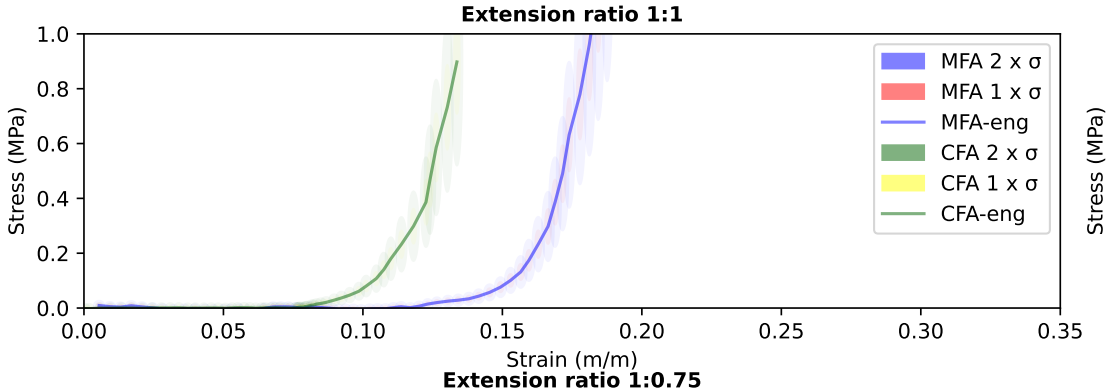

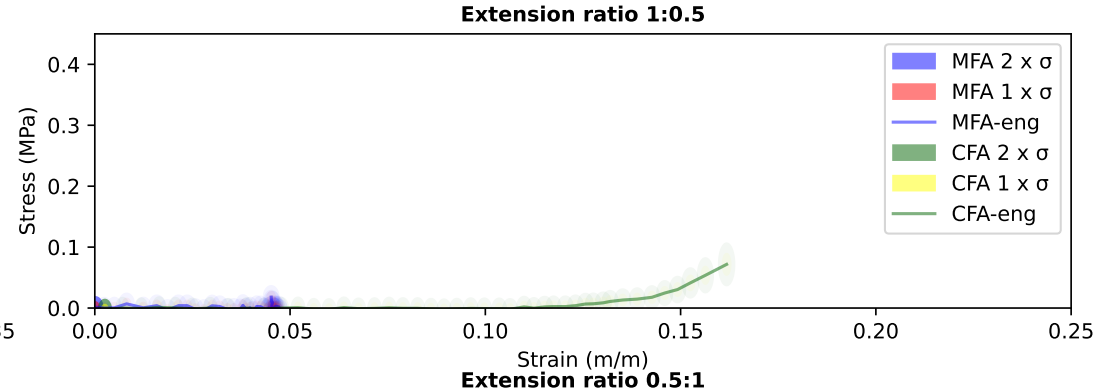

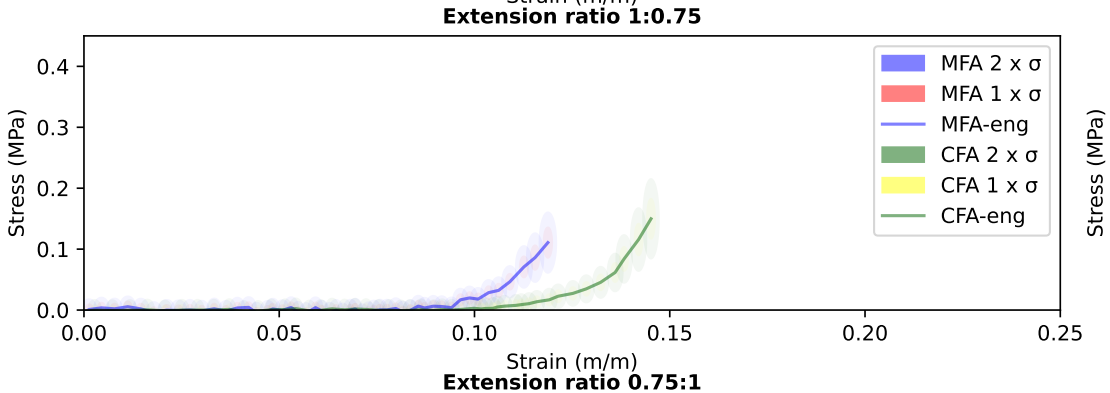

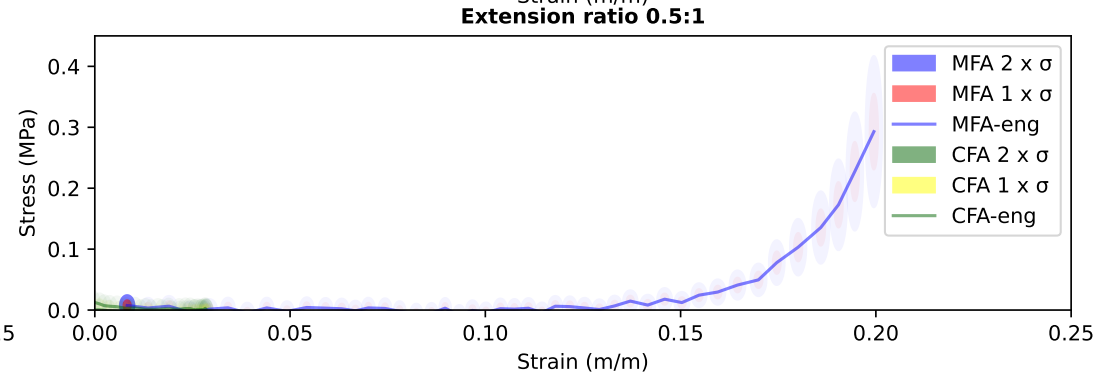

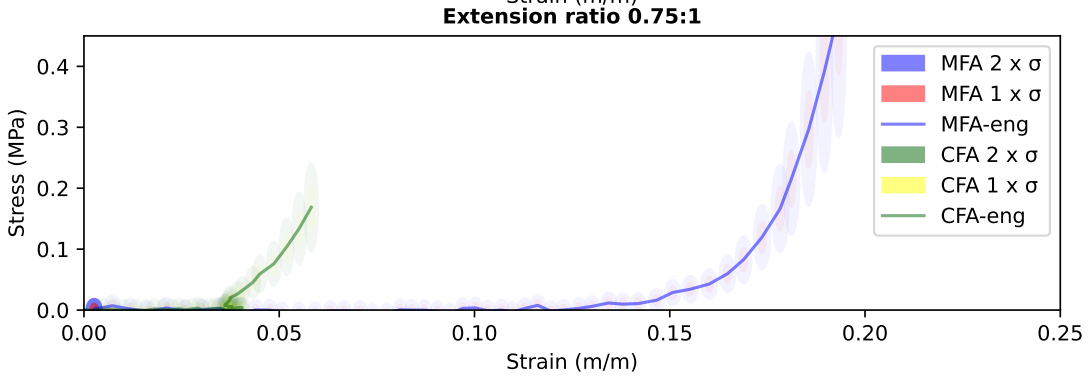

Comments: The thickness of this sample was assumed to be 50 µm, as this was part of the preliminary tests and the cryo-histology method had not yet been implemented. Looking at the 1:1 extension graph, the CFA had a stiffer response than the MFA curve, indicating that the axis may have been misidentified.

Specimen 2 HE

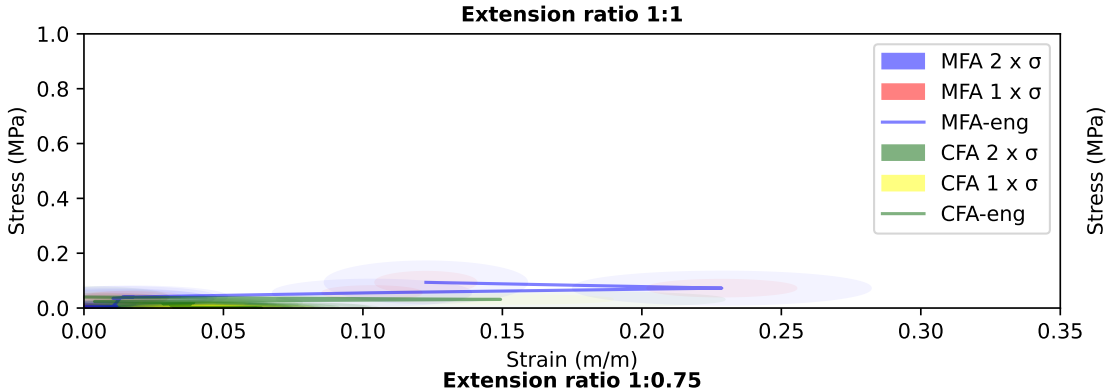

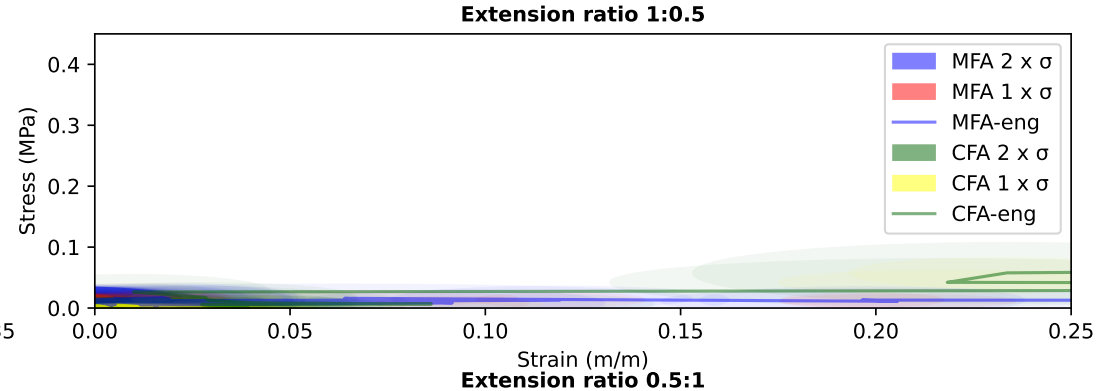

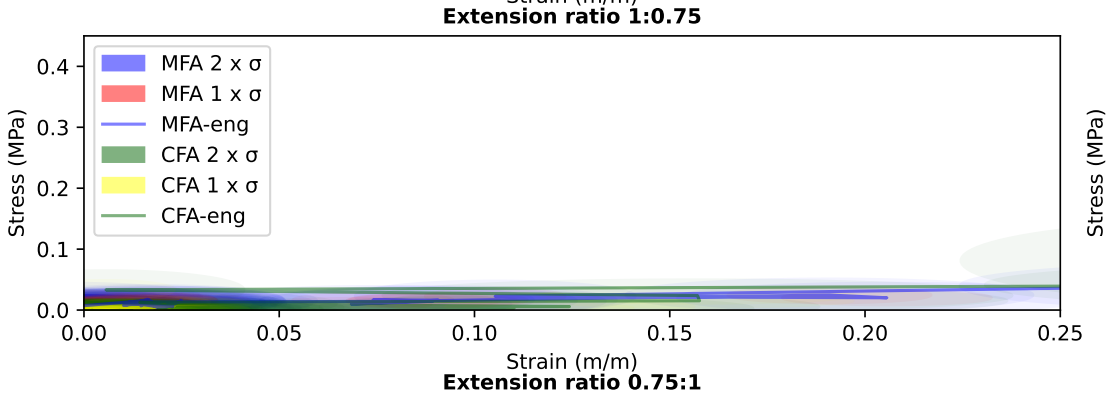

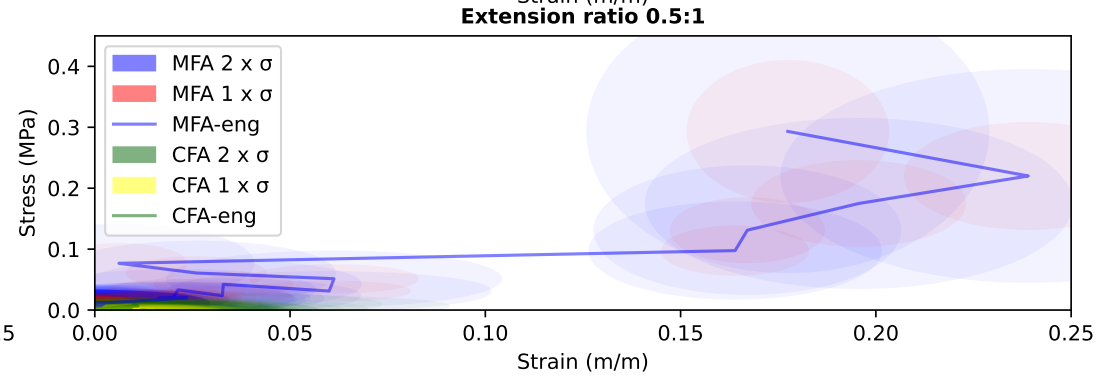

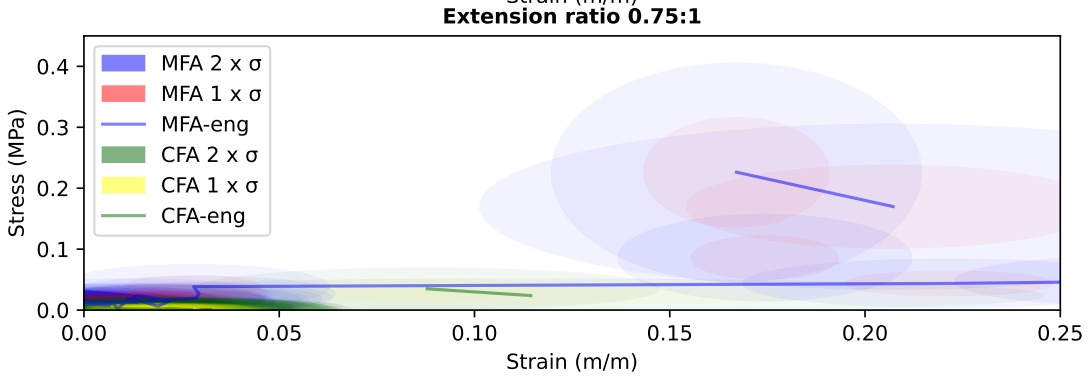

Comments: A typical stress-strain response was not observed across all extension ratios. The haphazard motion seen was due to the rakes erratically swinging while testing. Appendix C.2 provides a hyperlink showing a video capturing this motion. It was discovered that the rakes were incorrectly seated, which caused this unexpected behaviour and subsequently had to be discarded.

Specimen 3 HE

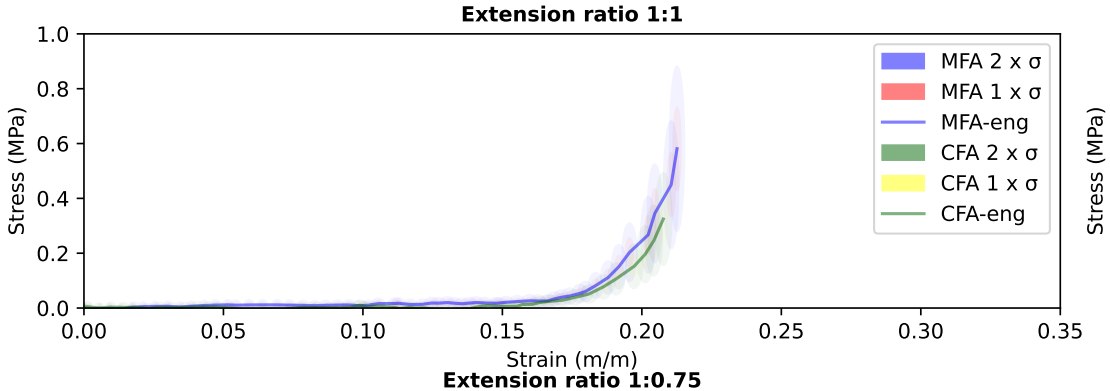

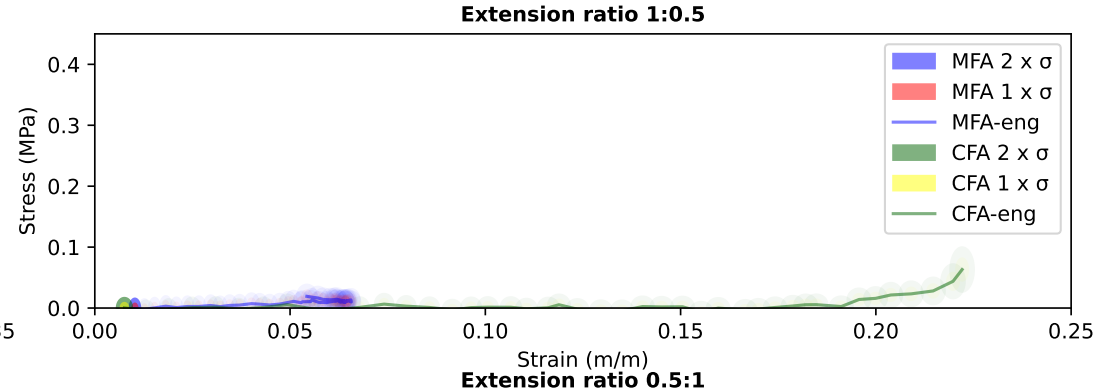

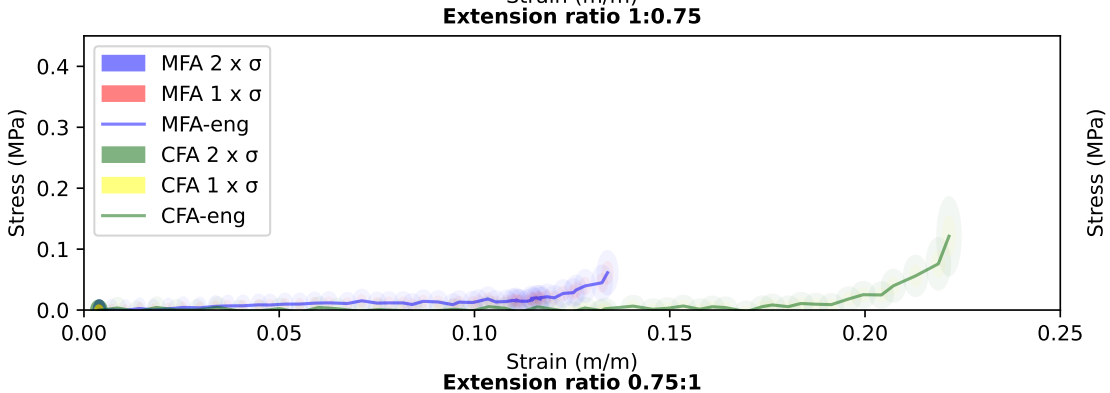

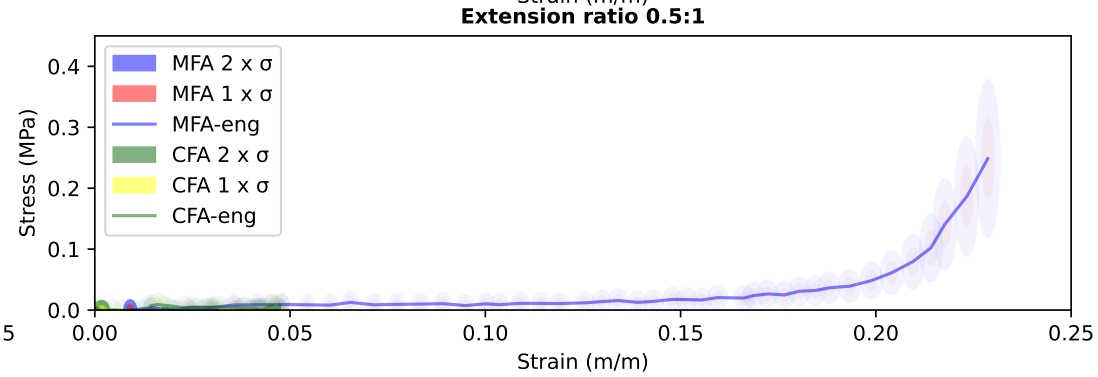

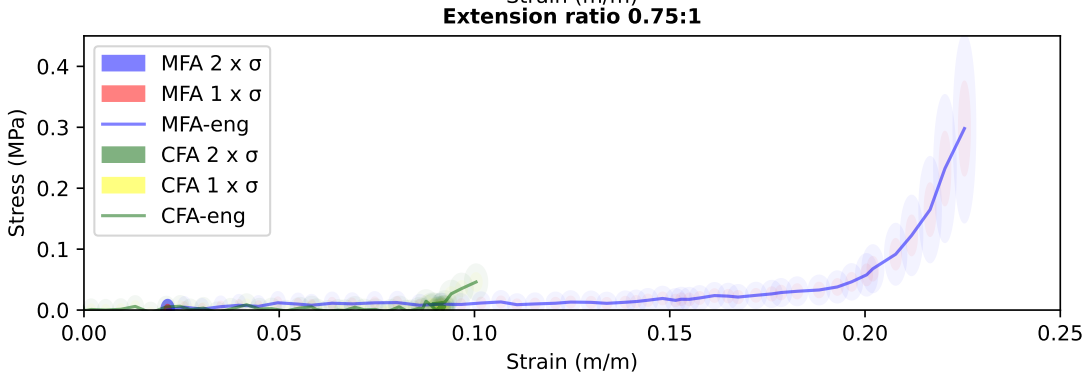

Comments: Both the CFA and MFA closely followed each other, with the MFA having a slightly stiffer response. While maintaining the MFA extension and reducing the CFA extension from 1 to 0.5, the MFA curve held the same trajectory but had decreasing maximum stress values. When the CFA extension was held at 1 and the MFA was reduced from 1 to 0.5, there was a steep drop in the stress and strain exerted on the CFA. This showed that the stress response of the CFA axis was heavily dependent on the MFA.

Specimen 4 HE

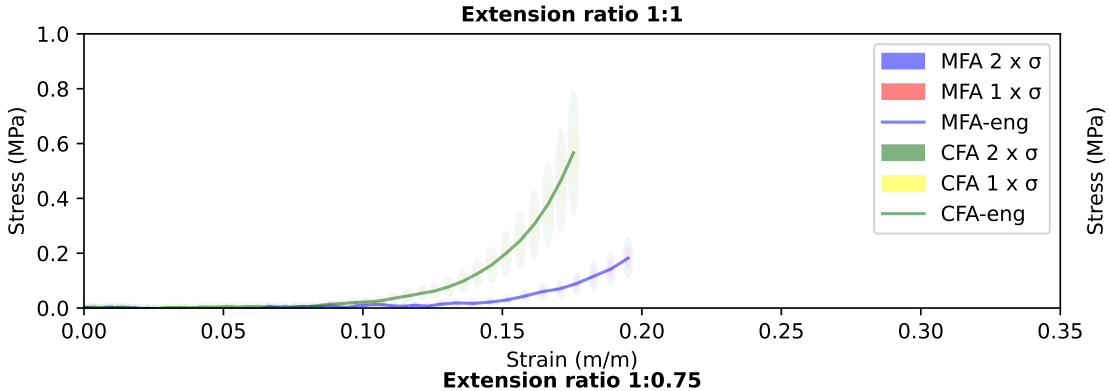

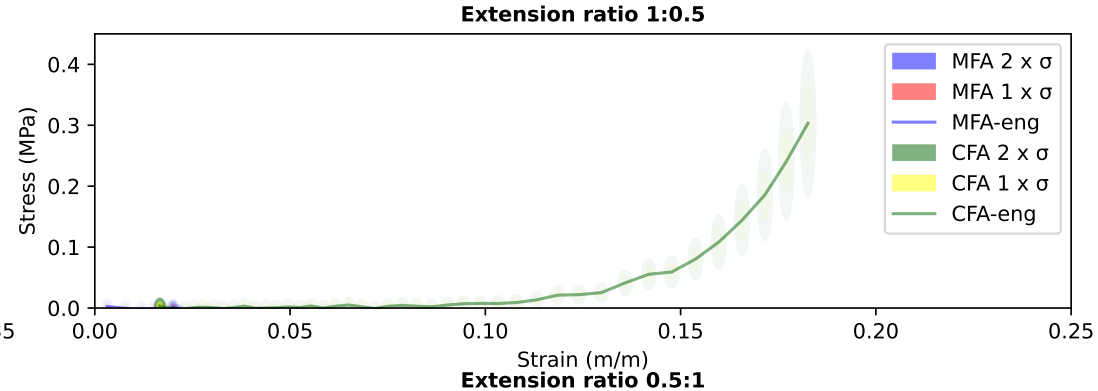

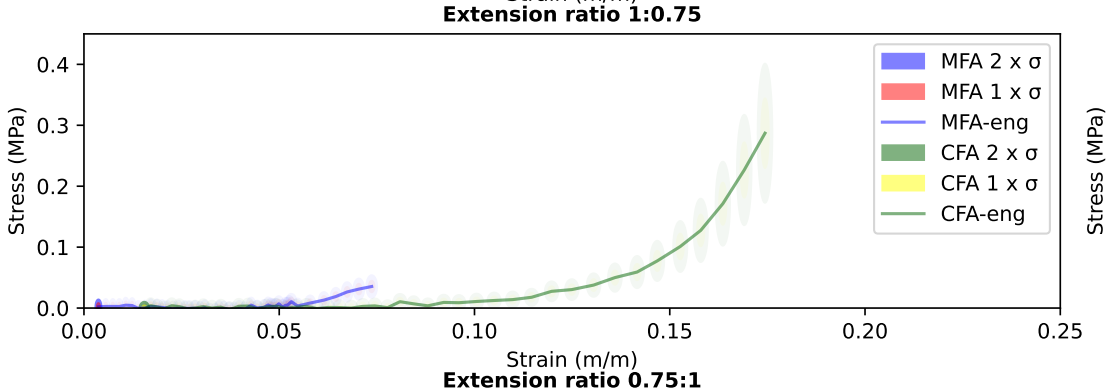

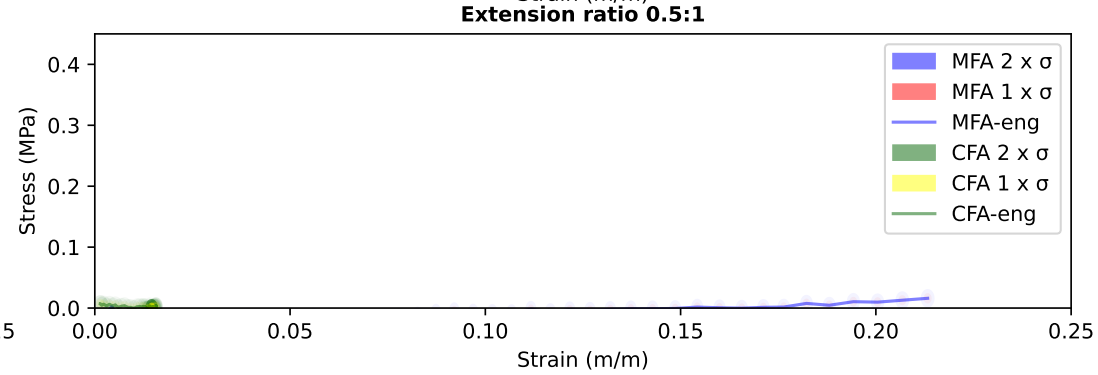

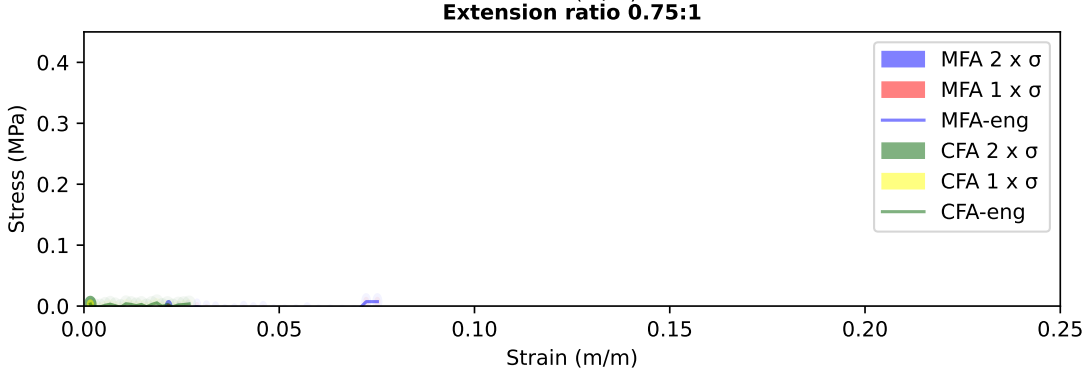

Comments: Like Specimen 1, the MFA and CFA were incorrectly identified as can be seen by the stiffer response shown by the labelled CFA curve. Stress-strain data can only be seen when the CFA is held at 100% extension. In the remaining graphs, the loads recorded were too low to warrant any discussion. The CFA held the same stress-strain response in all cases where its extension was kept at 100%.

Specimen 5 HE

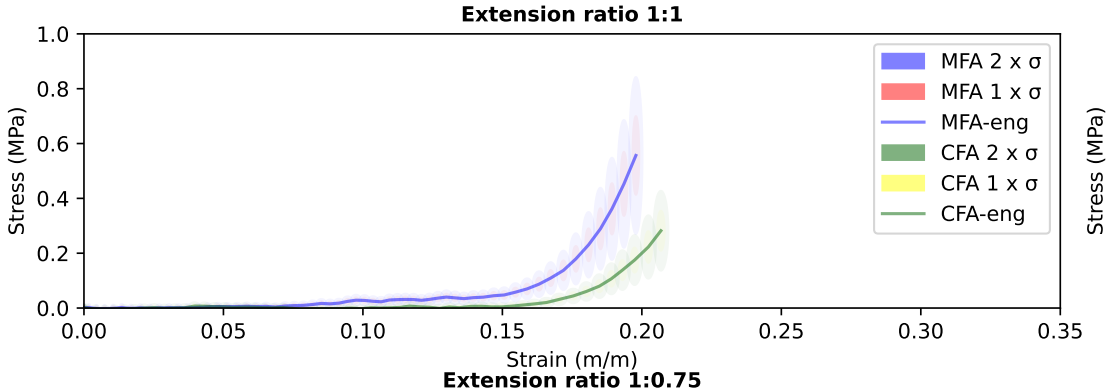

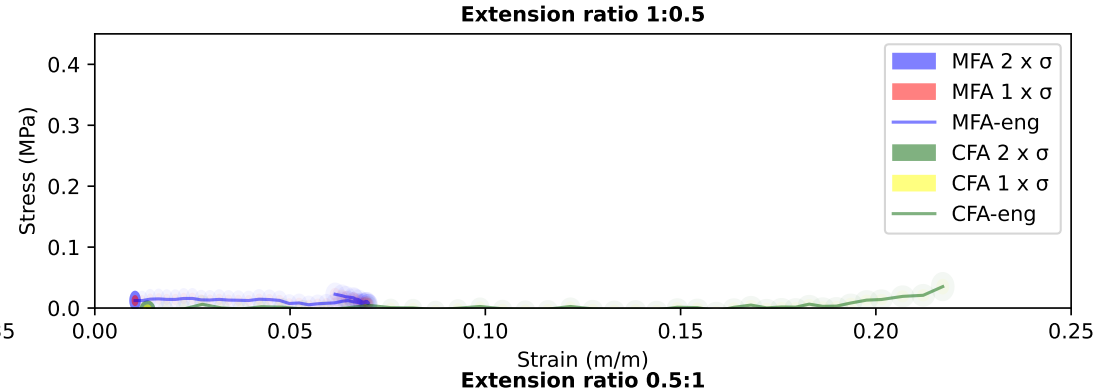

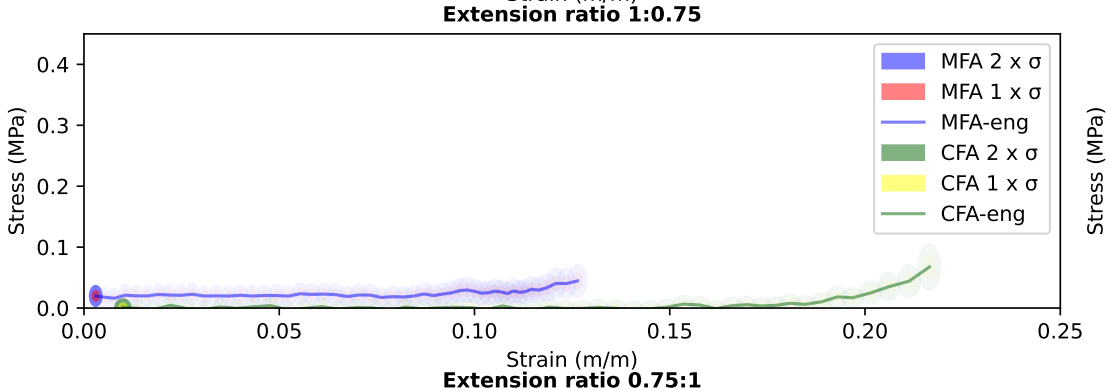

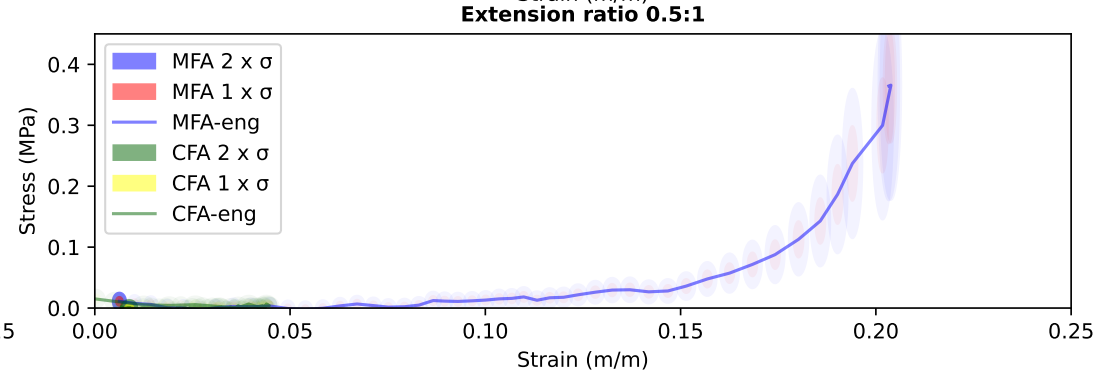

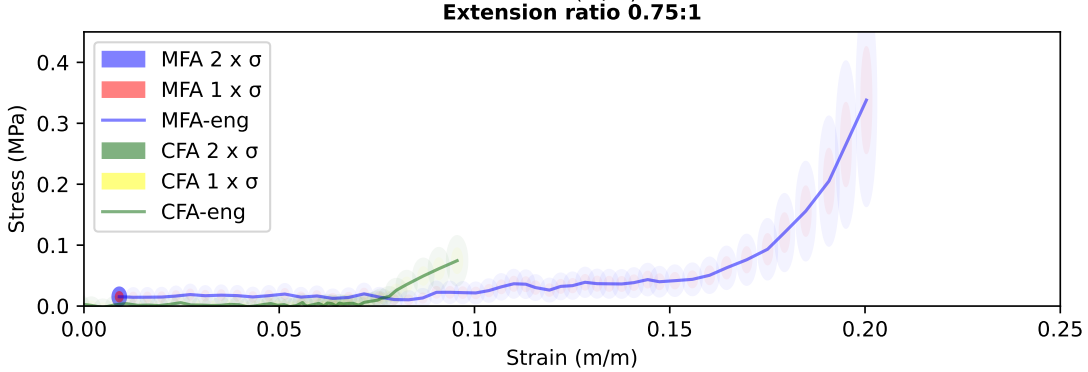

Comments: The MFA and CFA axes were correctly identified. The MFA response was observed to be very dependent on the extension exerted along the CFA axis, where the lower the CFA was extended, the lower the loads and strains recorded along the MFA. In the scenarios where the CFA was under 100% extension, the MFA would experience a large stress-strain response very similar to the MFA curve in the 1:1 ratio.

Specimen 6 HE

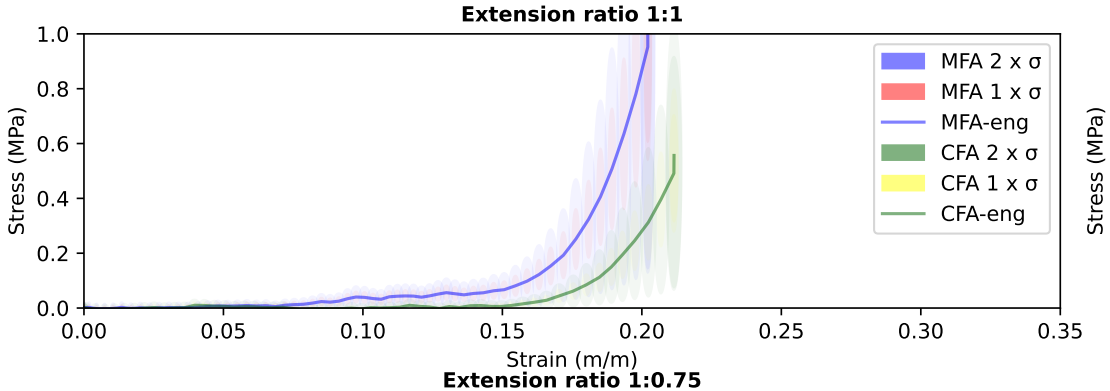

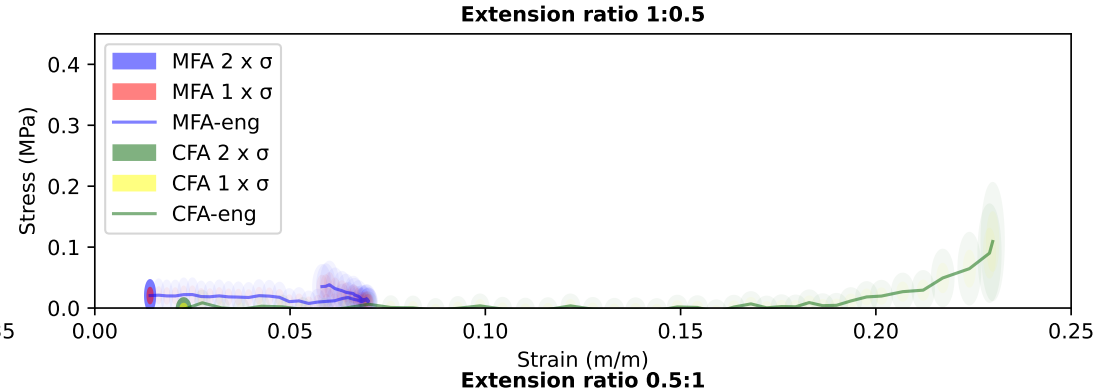

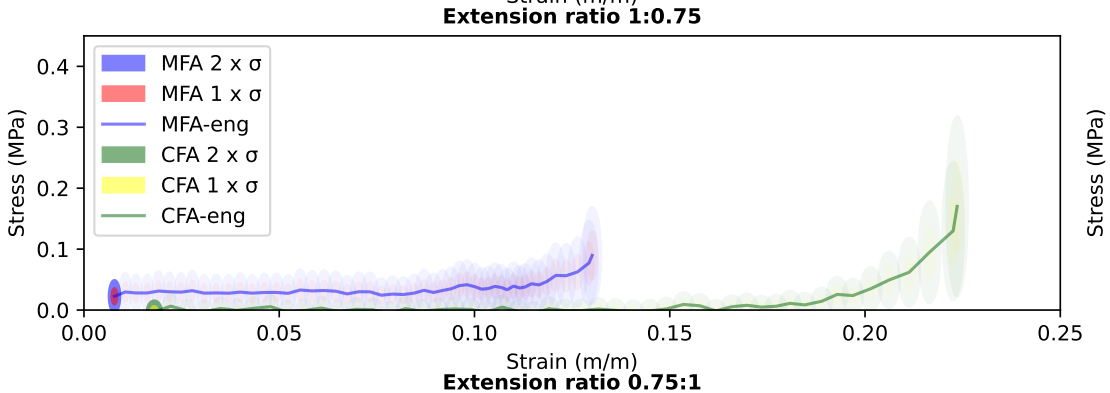

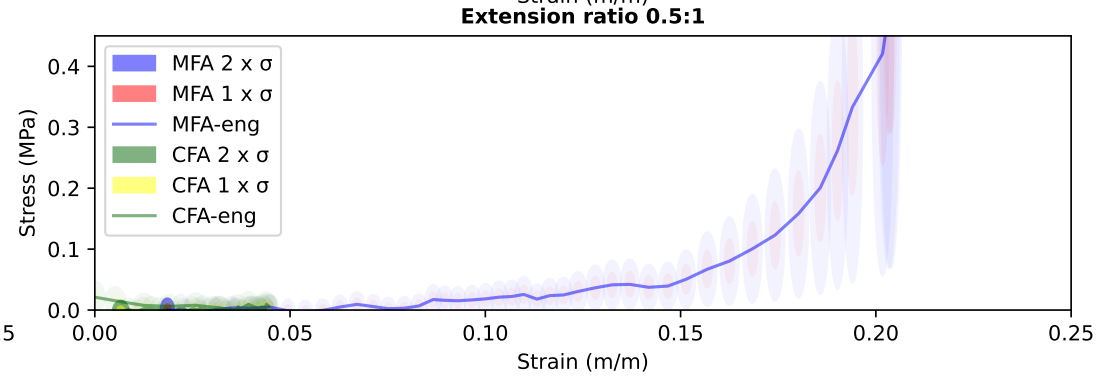

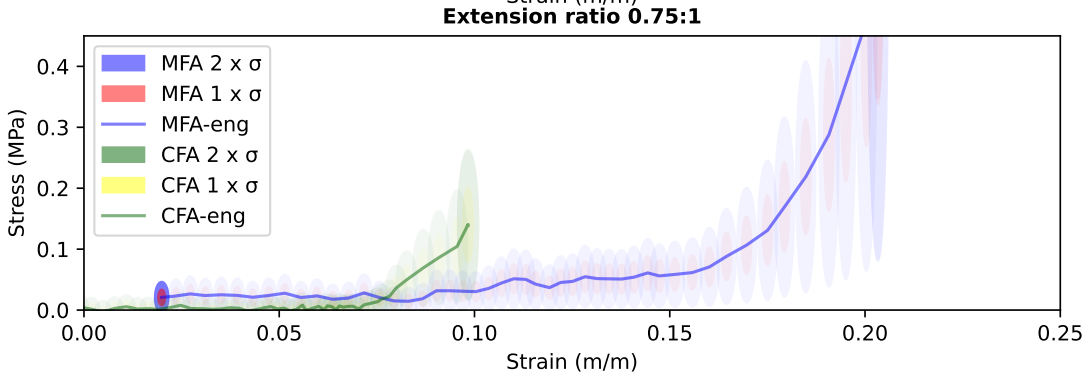

Comments: Similar characteristic behaviour to Specimen 5.

Specimen 7 HE

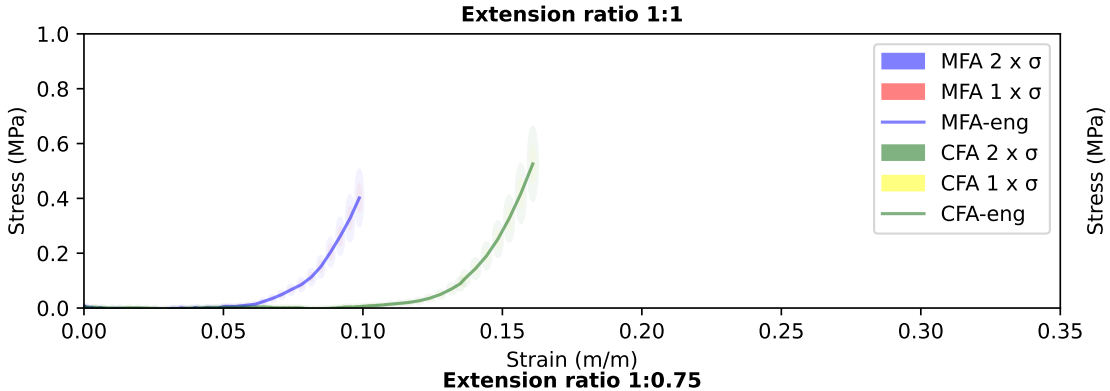

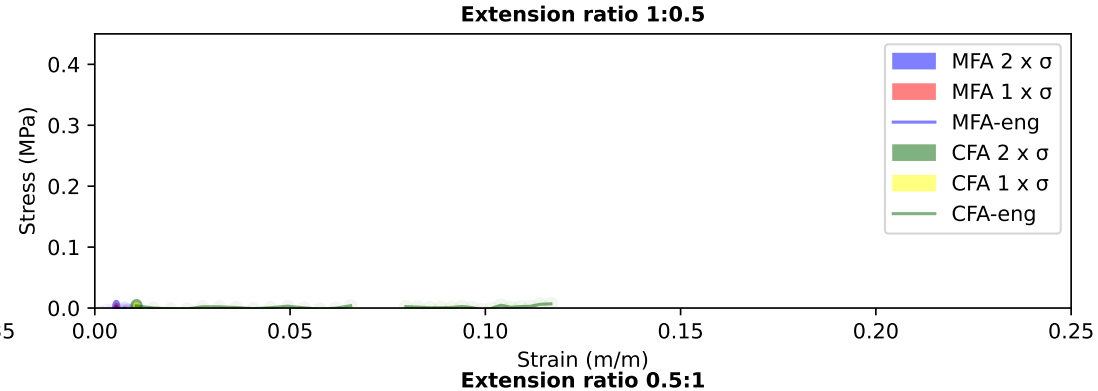

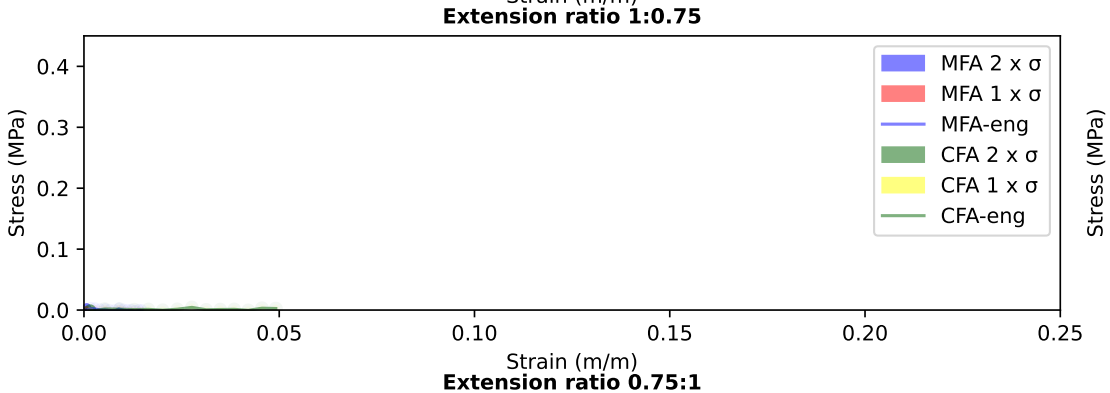

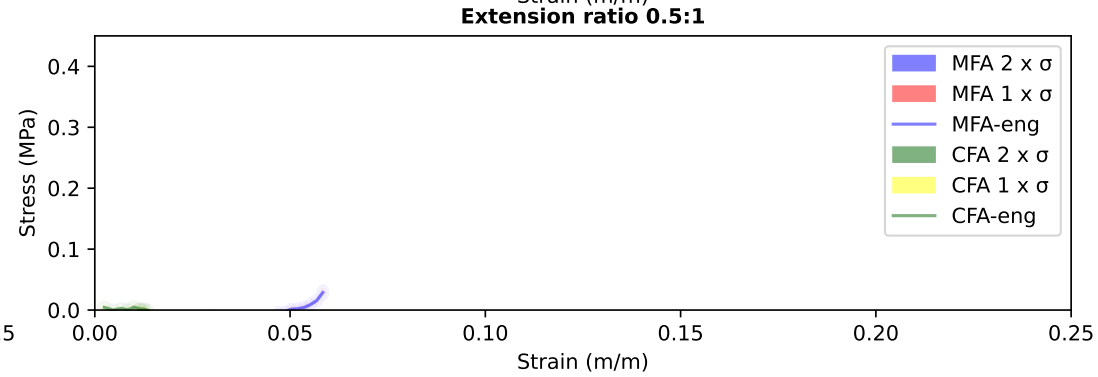

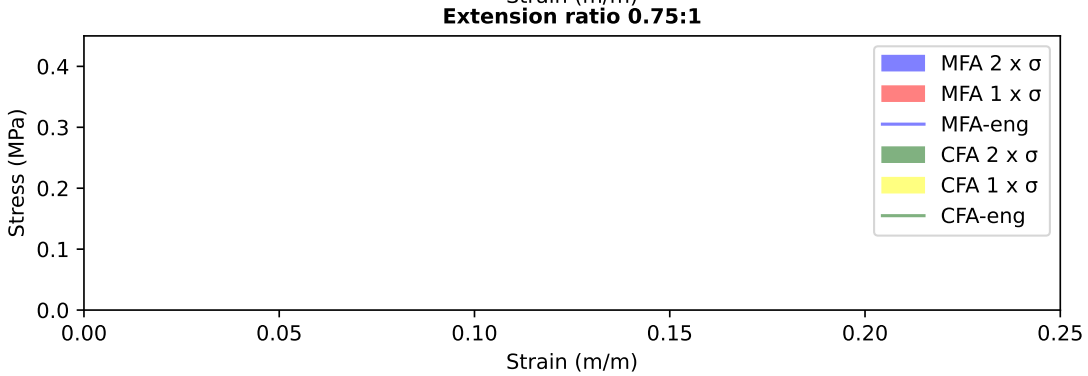

Comments: The MFA and CFA axes were correctly identified, based on the response seen under a 1:1 extension. For the remaining extension ratios, the load readings were very low.

Specimen 8 HE

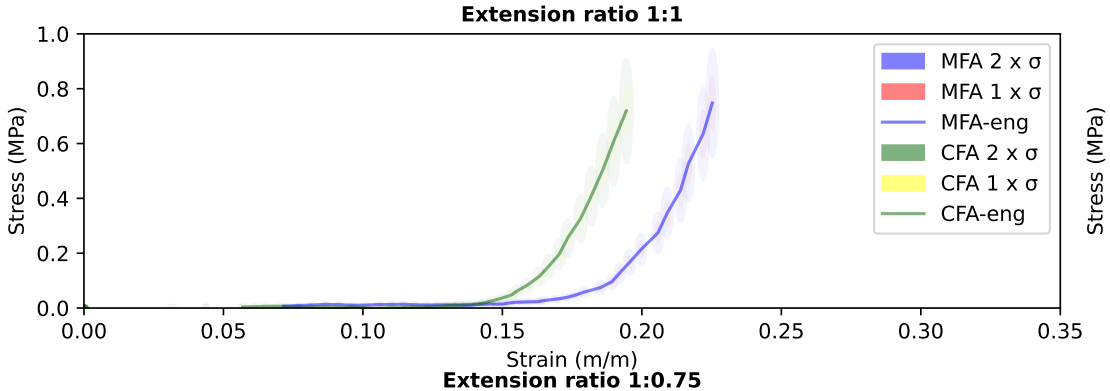

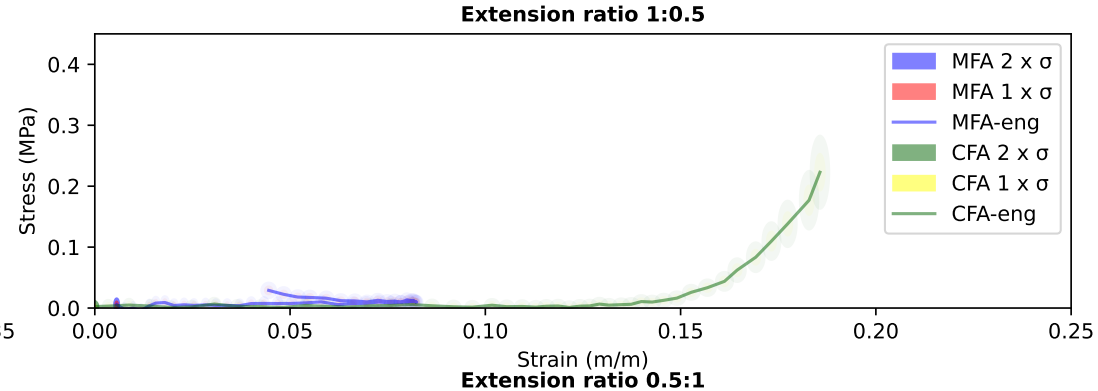

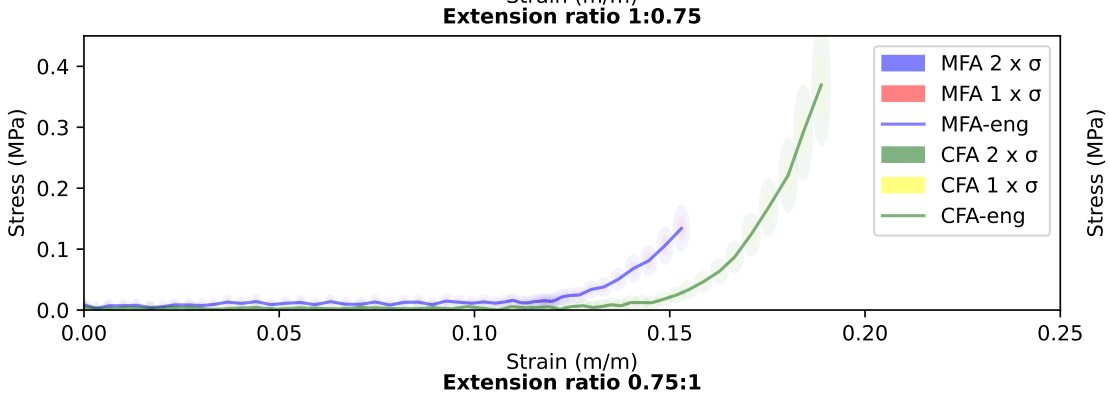

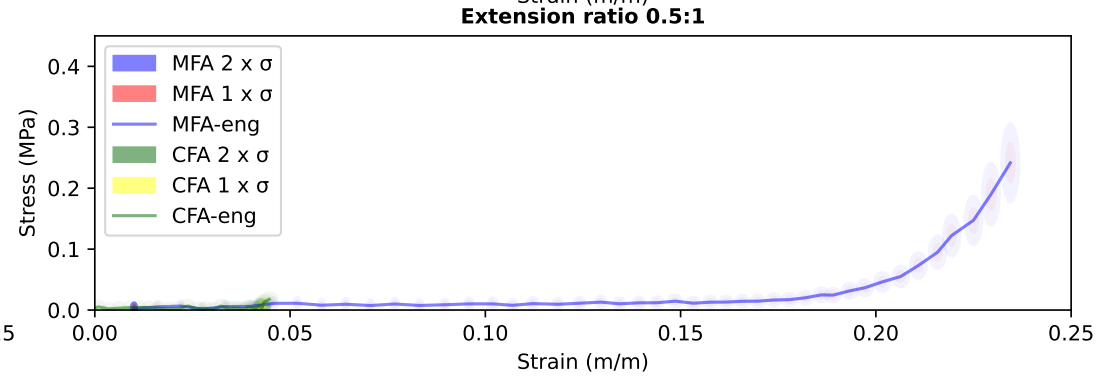

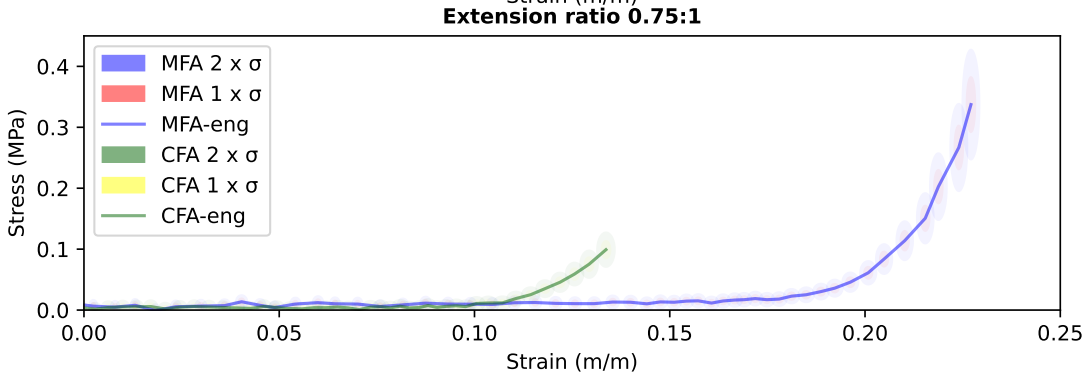

Comments: The MFA and CFA axes were correctly identified. Assuming the CFA curves were coloured blue, and the MFA curves were green, the behaviour is analogous to that of Specimen 5. At the 1:0.5 extension ratio, the blue curve shows a decrease in strain, resulting from the sample contracting and travelling back to its resting position.

Specimen 9 HE

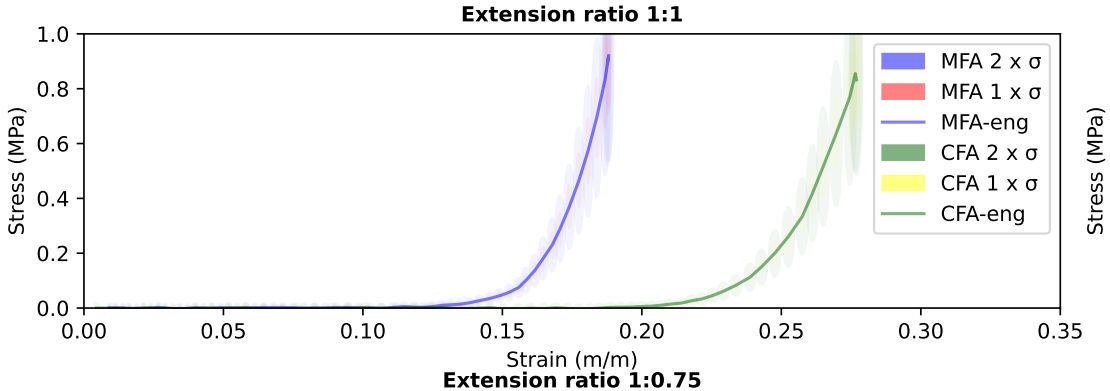

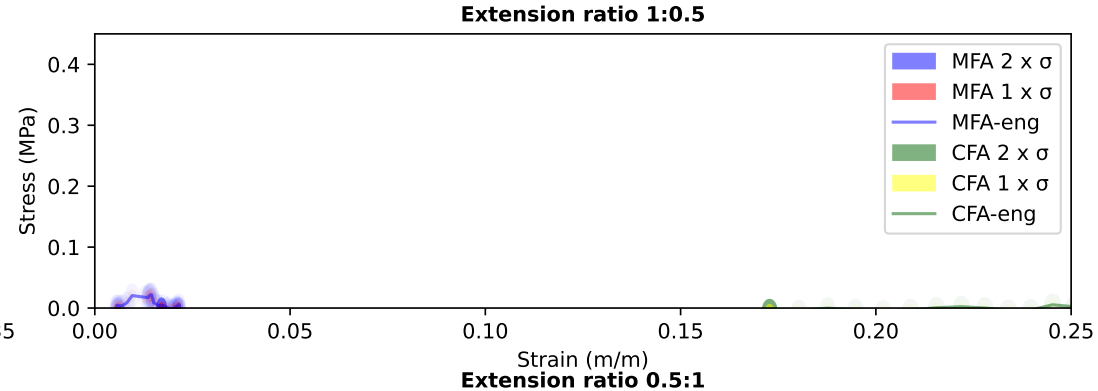

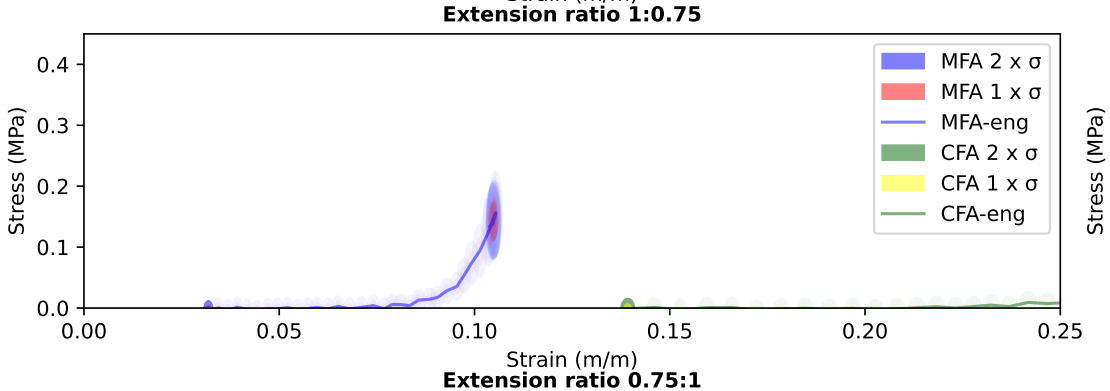

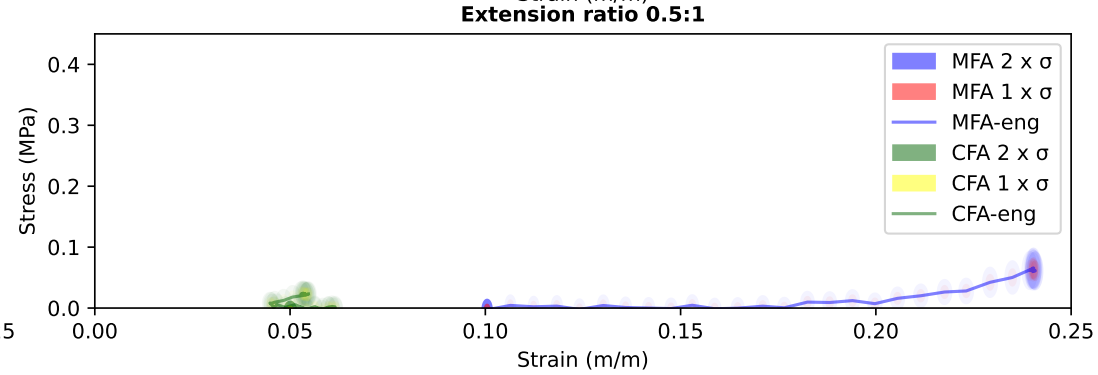

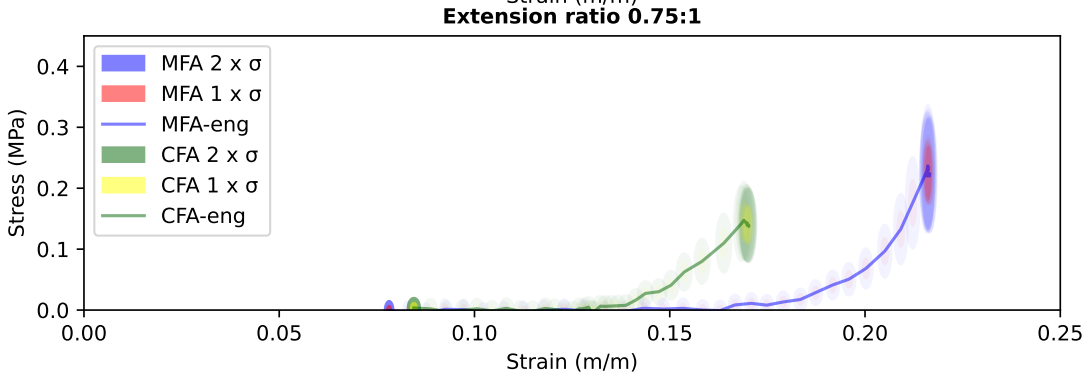

Comments: The MFA and CFA axes were correctly identified. Loads recorded when the MFA extension was reduced to 0.75 and 0.5 were low for both axes. Reducing the CFA extension lowered the stress response on the MFA axis, with the characteristic "J" curve occurring at different strains than those under a 1:1 extension ratio.

C.4 Bulge-test strain maps

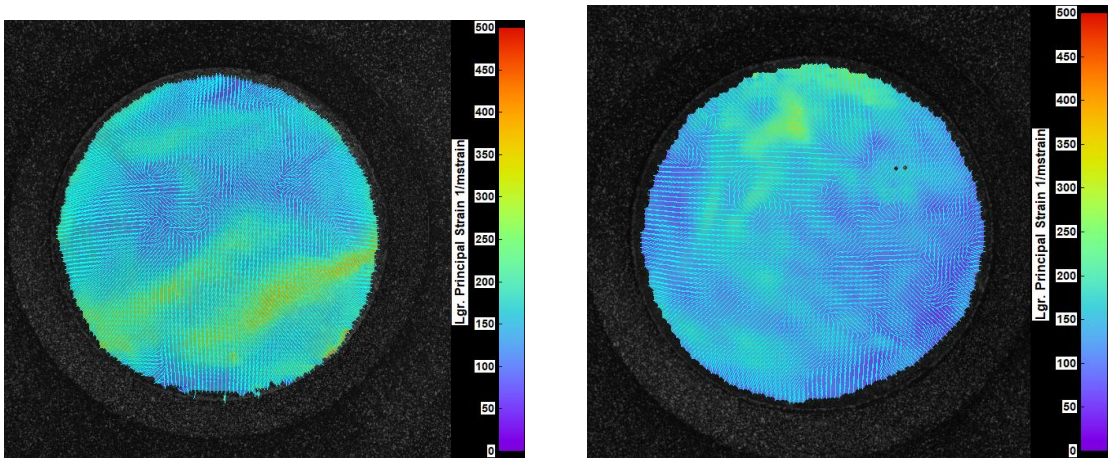

(a) Specimen 1

(b) Specimen 2

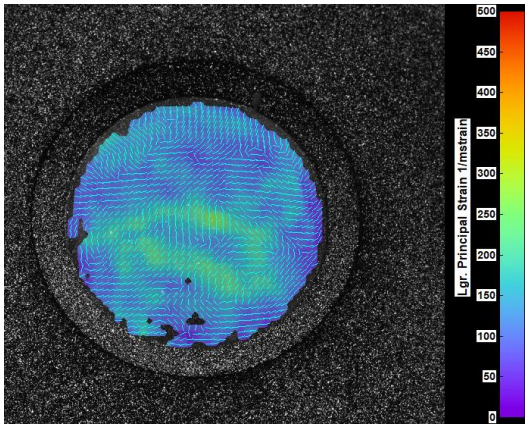

(c) Specimen 3

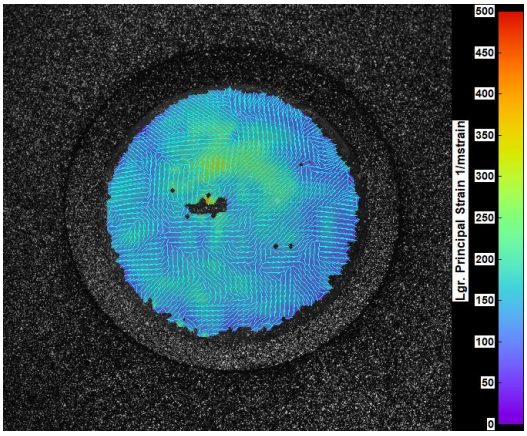

(d) Specimen 4

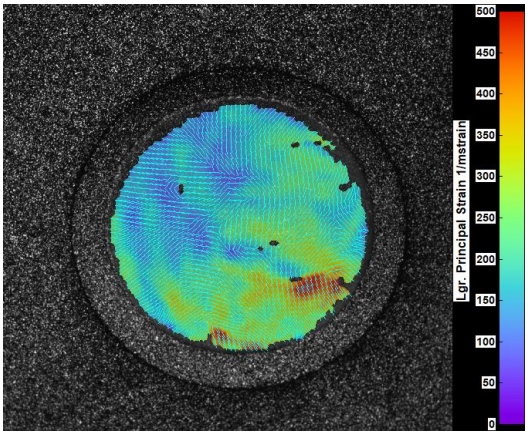

(e) Specimen 5

Figure C.2 Map showing the principle strain 1 values for the first four specimens

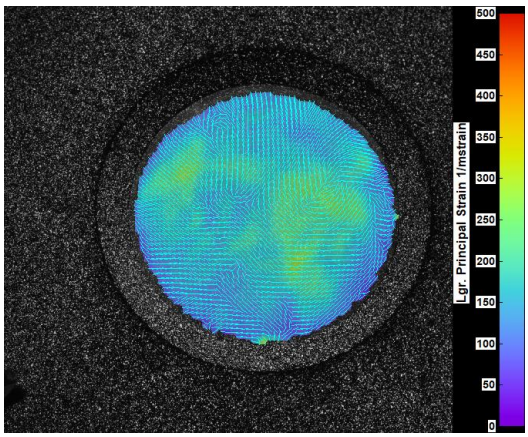

(f) Specimen 6

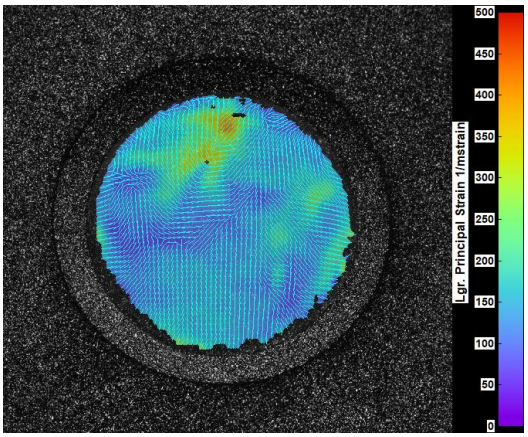

(g) Specimen 7

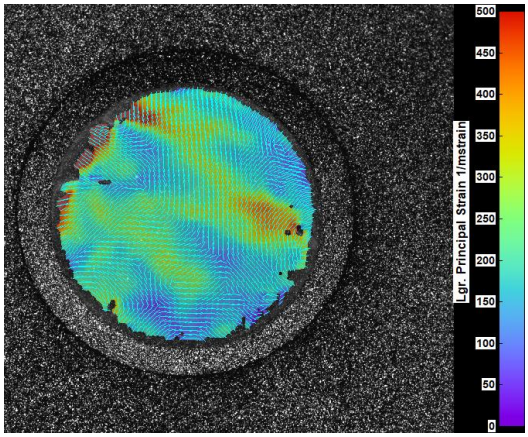

(h) Specimen 8

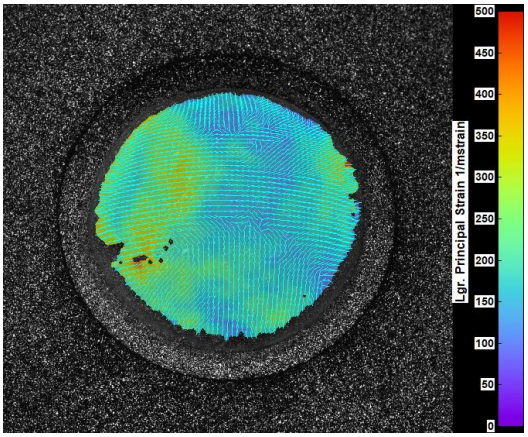

(i) Specimen 9

Figure C.2 Map showing the principle strain 1 values for the remaining three specimens

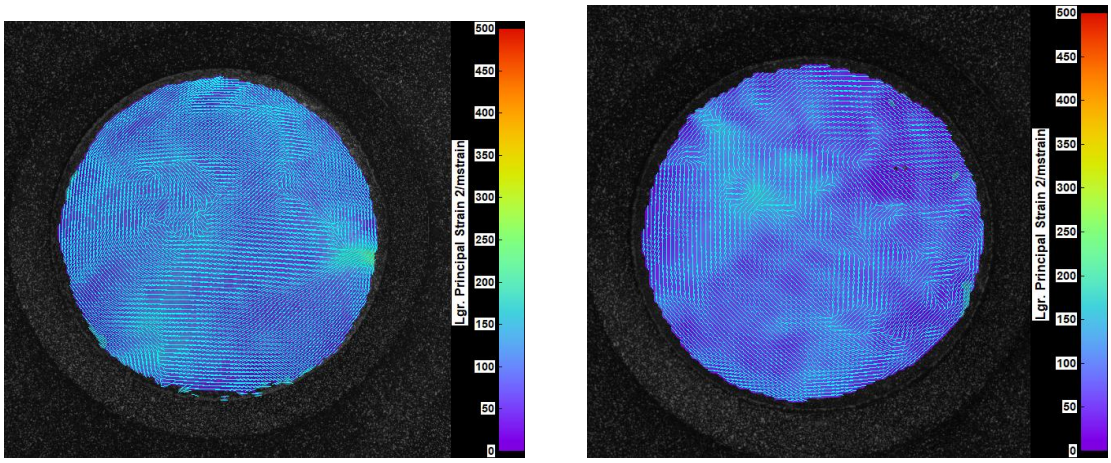

(a) Specimen 1

(b) Specimen 2

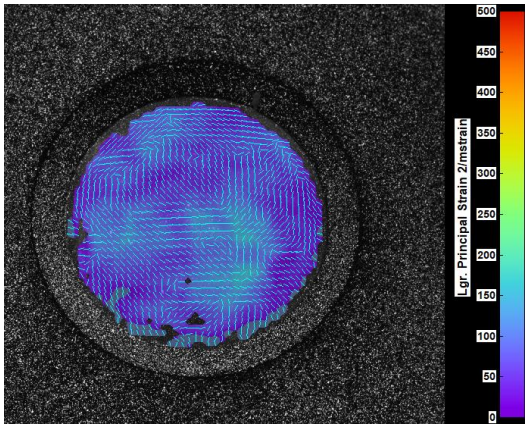

(c) Specimen 3

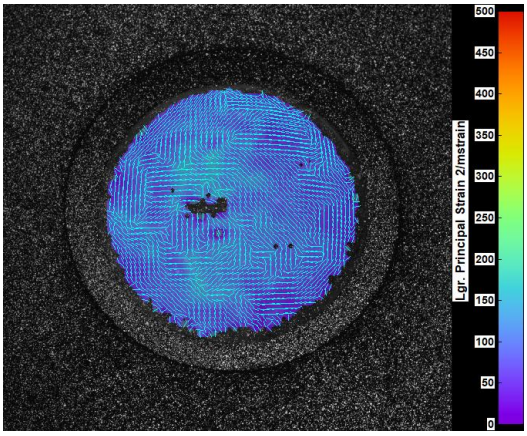

(d) Specimen 4

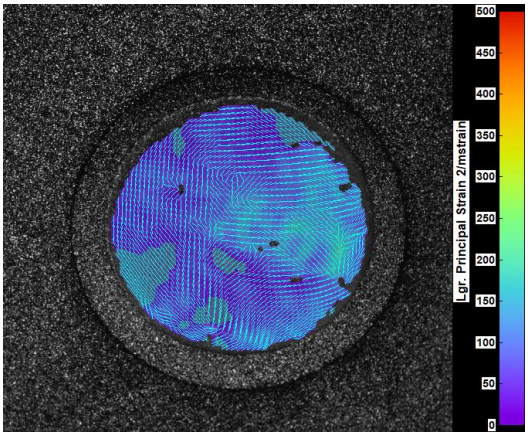

(e) Specimen 5

Figure C.3 Map showing the principle strain 2 values for the first four specimens

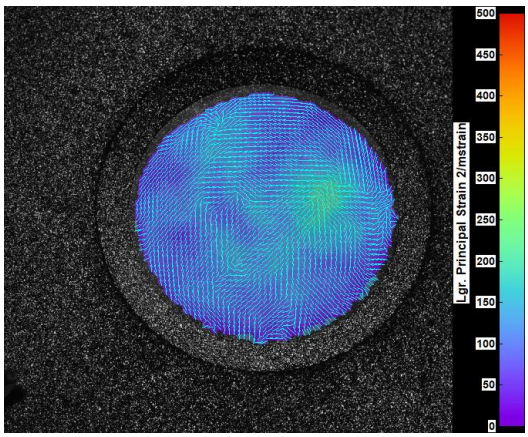

(f) Specimen 6

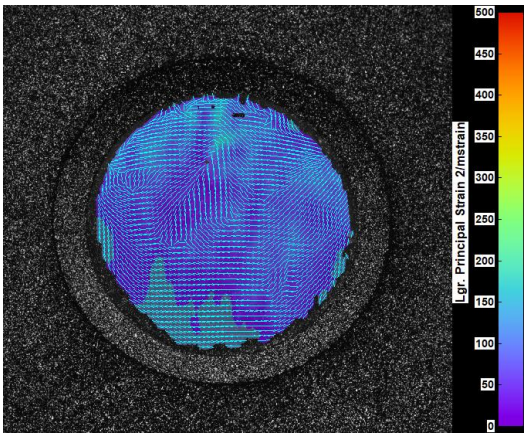

(g) Specimen 7

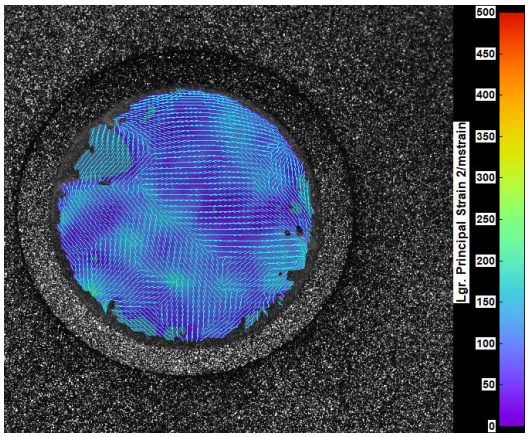

(h) Specimen 8

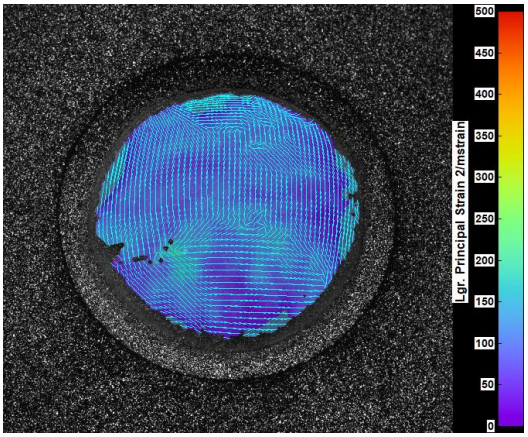

(i) Specimen 9

Figure C.3 Map showing the principle strain 2 values for the first four specimens

C.5 Greyscale Charts

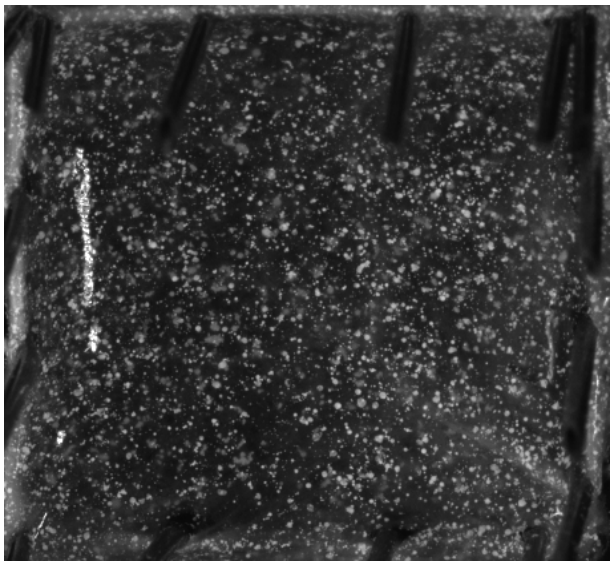

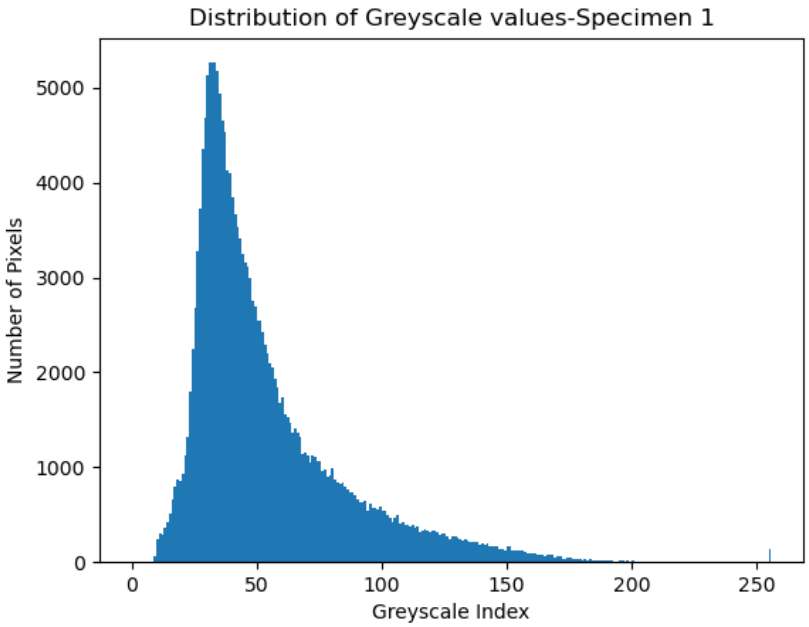

Figure C.4 Greyscale values observed on Specimen 1

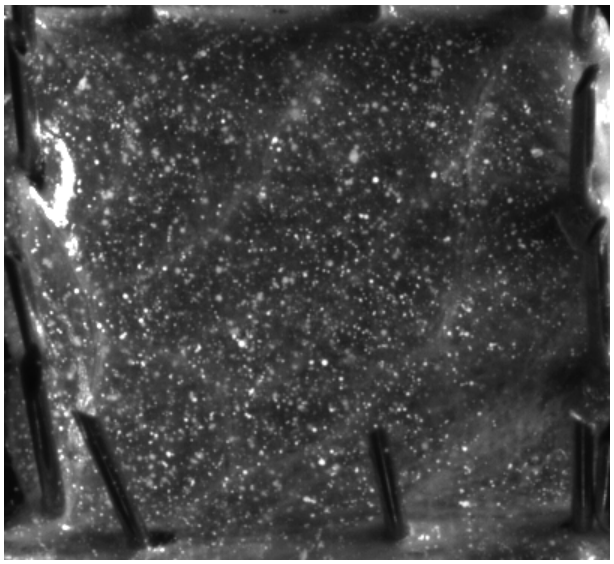

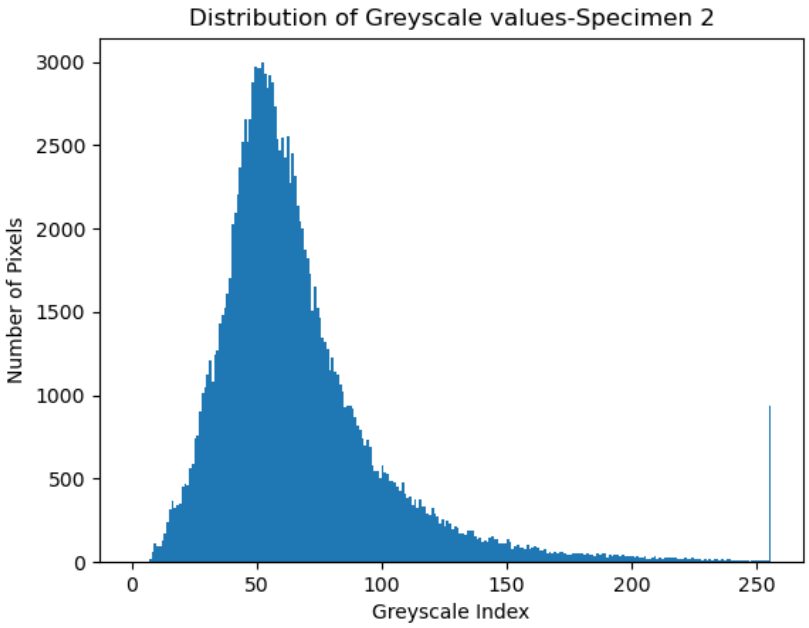

Figure C.5 Greyscale values observed on Specimen 2

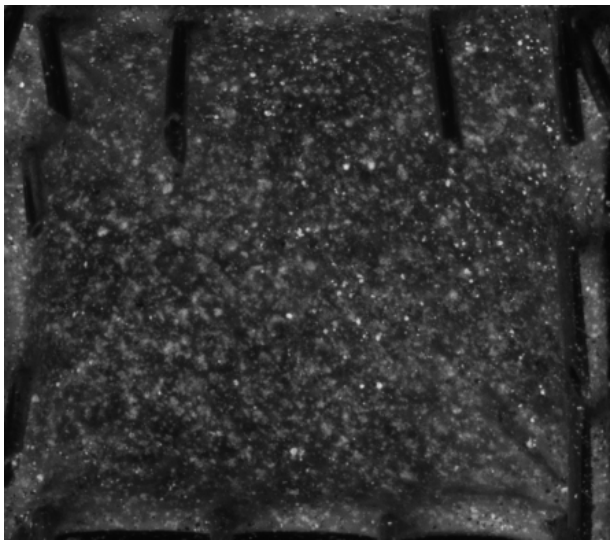

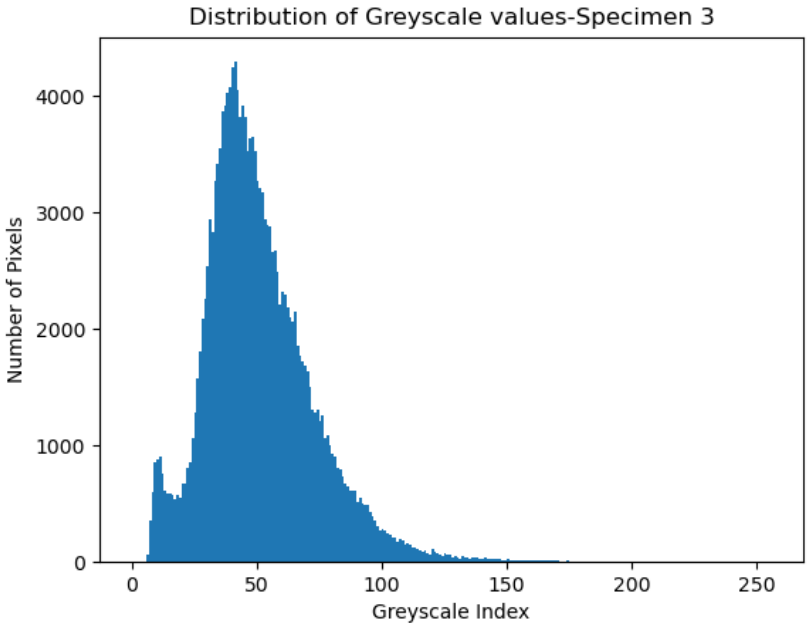

Figure C.6 Greyscale values observed on Specimen 3

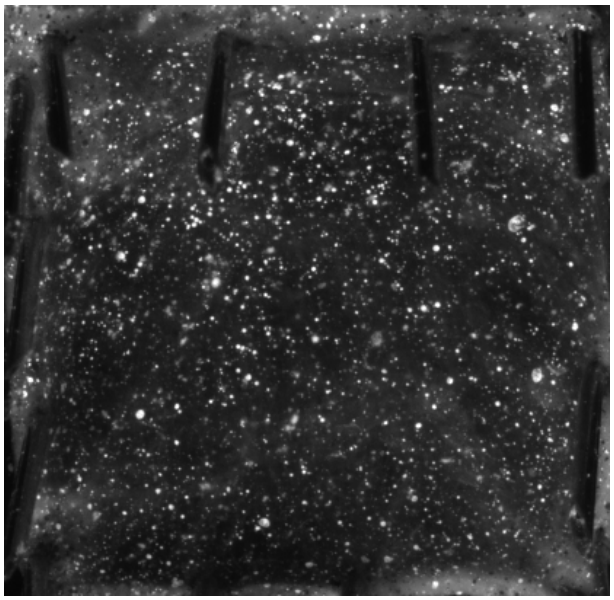

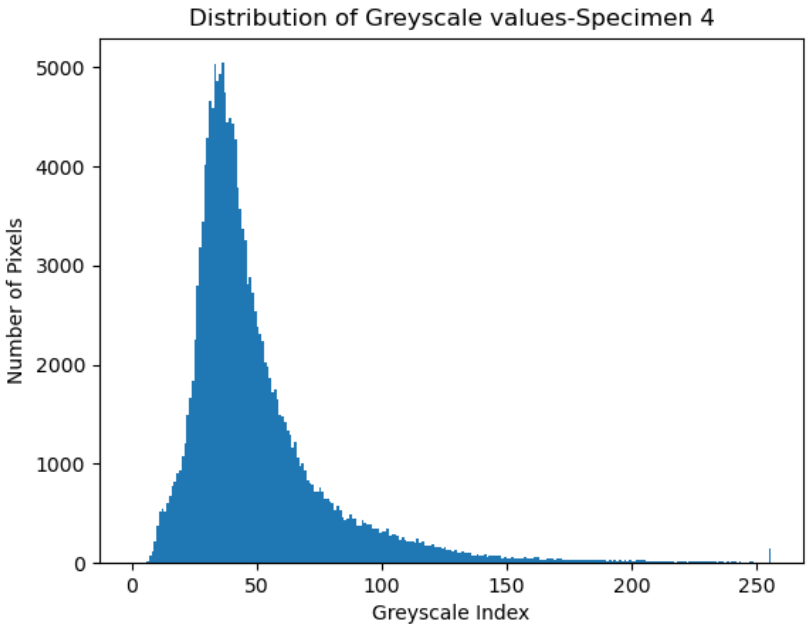

Figure C.7 Greyscale values observed on Specimen 4

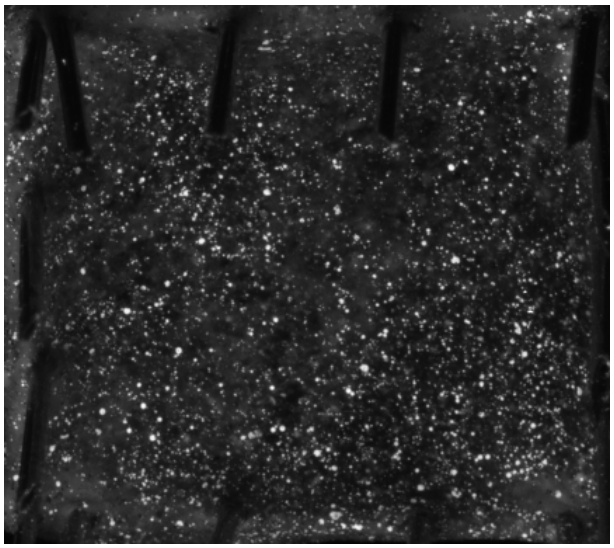

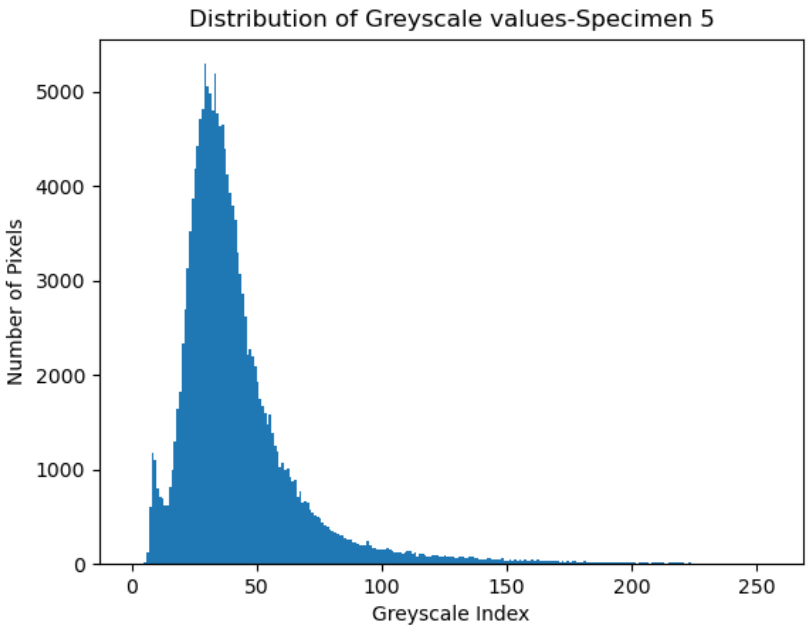

Figure C.8 Greyscale values observed on Specimen 5

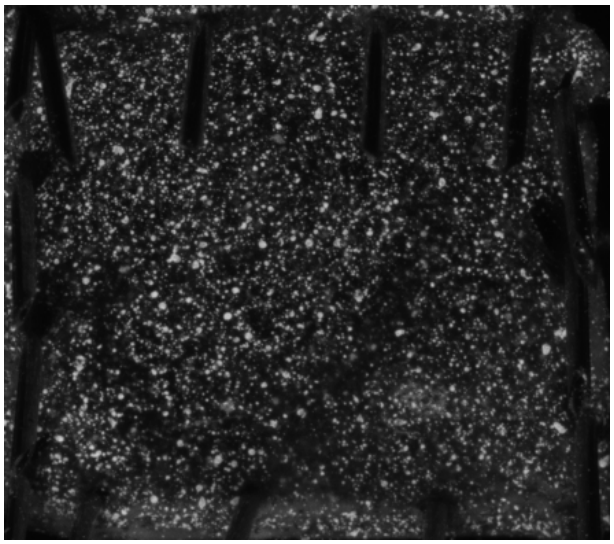

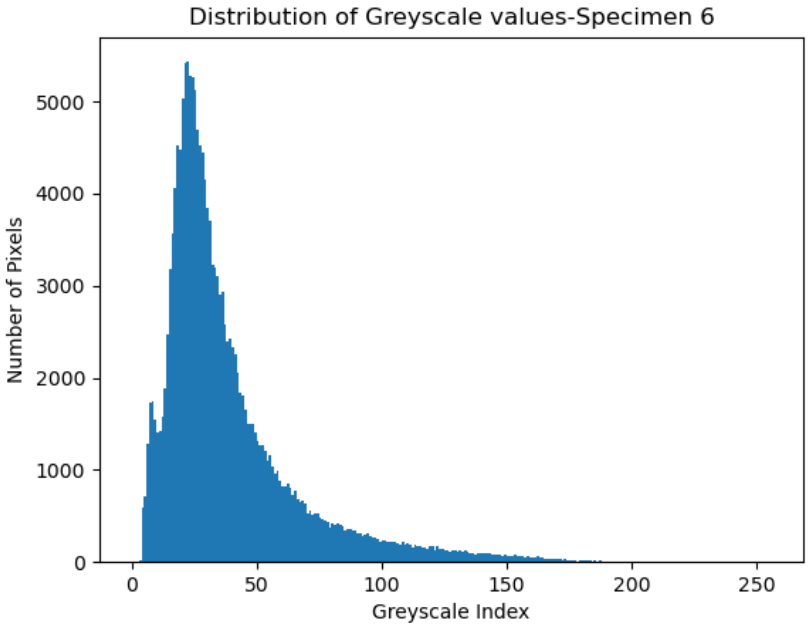

Figure C.9 Greyscale values observed on Specimen 6

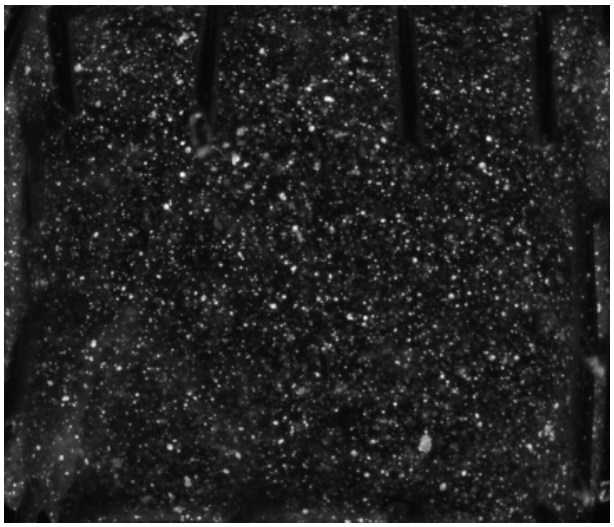

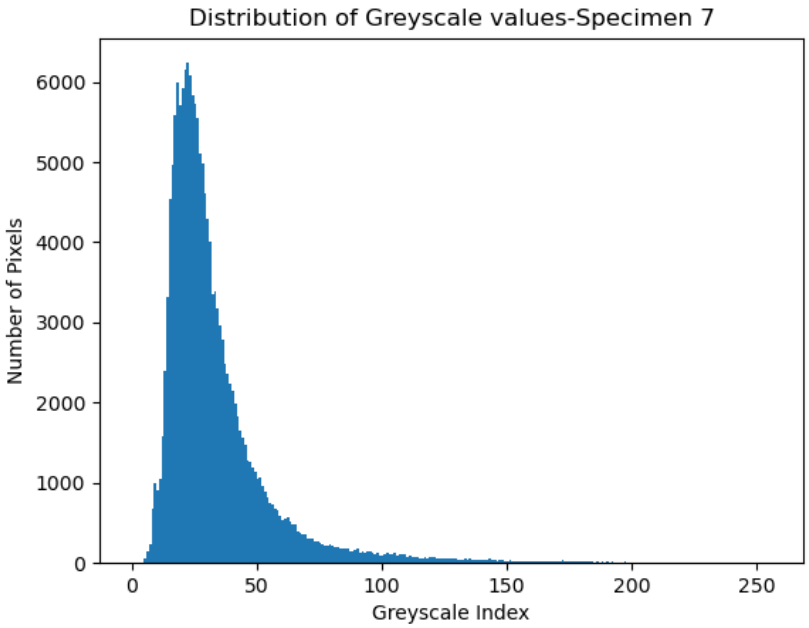

Figure C.10 Greyscale values observed on Specimen 7

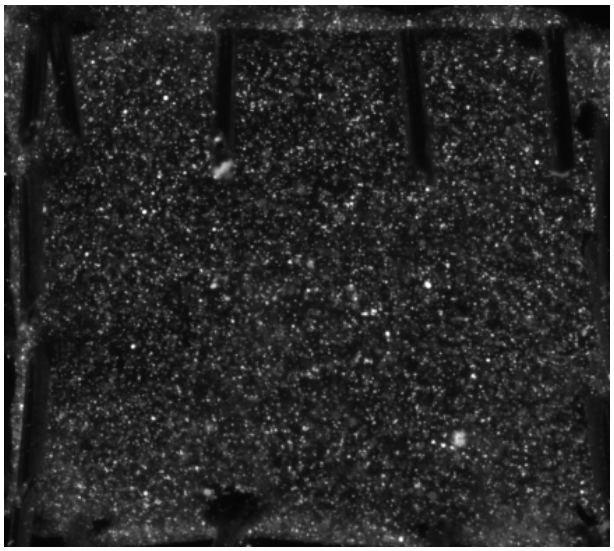

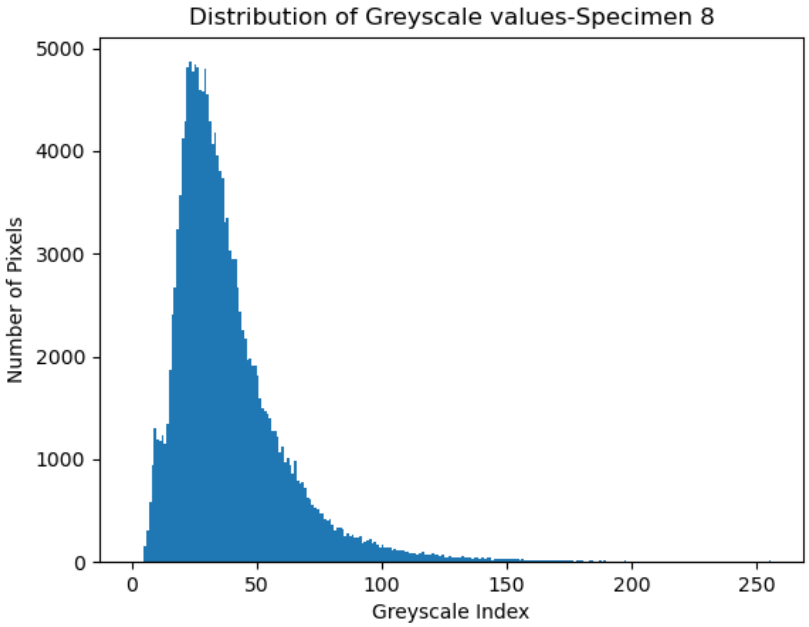

Figure C.11 Greyscale values observed on Specimen 8

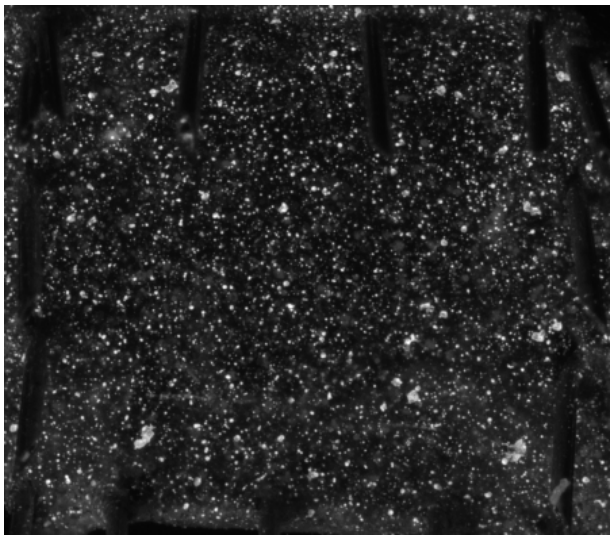

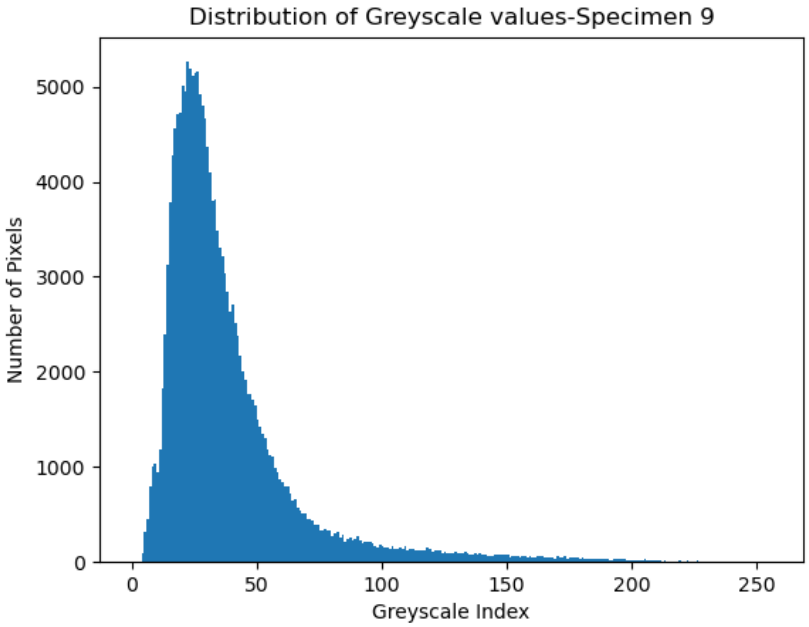

Figure C.12 Greyscale values observed on Specimen 9

Appendix D

Curve Fitting Experimental Data

D.1 Gasser-Ogden-Holfzapfel Material Model

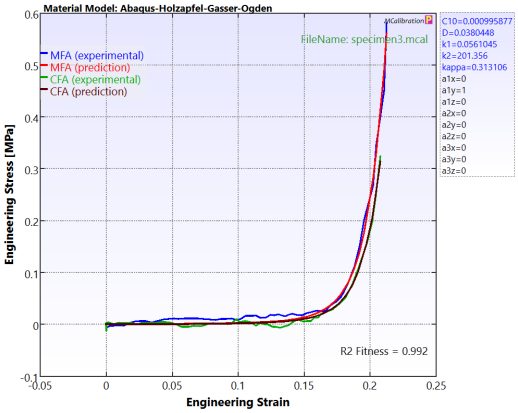

(a) Specimen 3

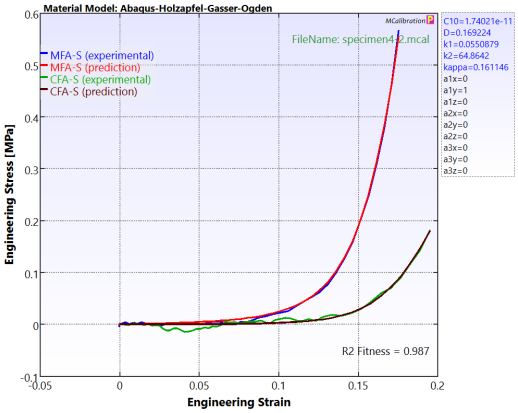

(b) Specimen 4

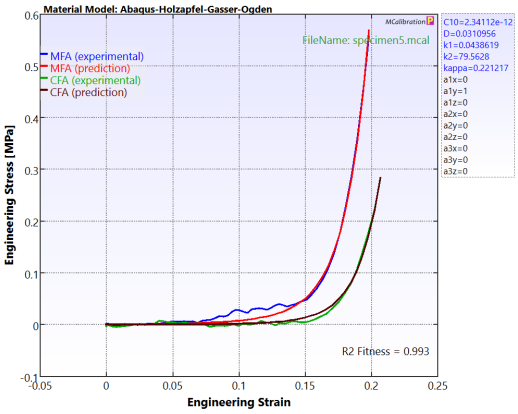

(c) Specimen 5

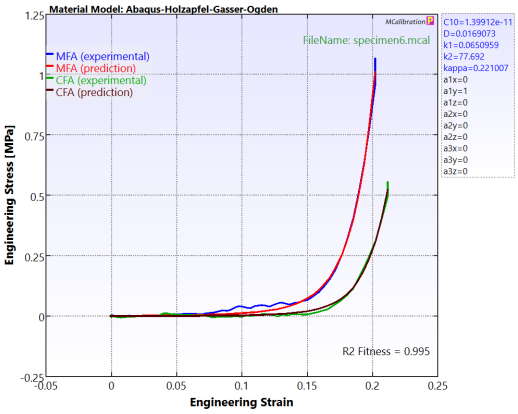

(d) Specimen 6

Figure D.1 Experimental data curve-fitted using MCalibration for the first four specimens

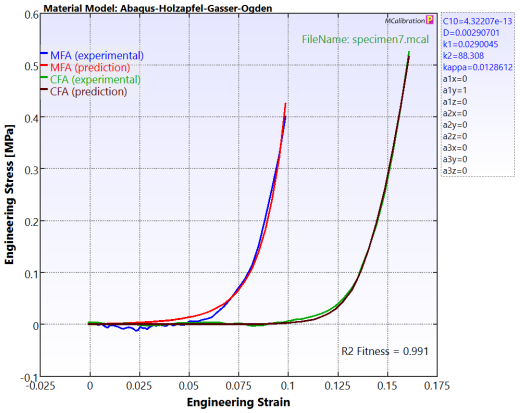

(e) Specimen 7

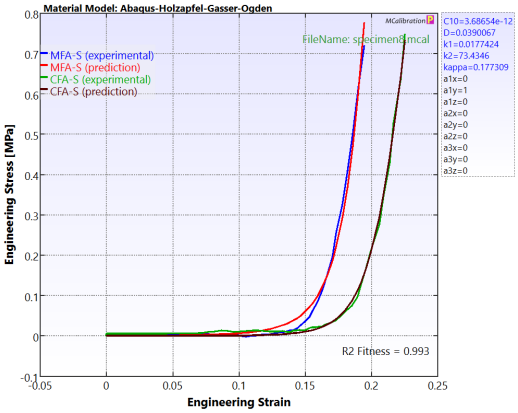

(f) Specimen 8

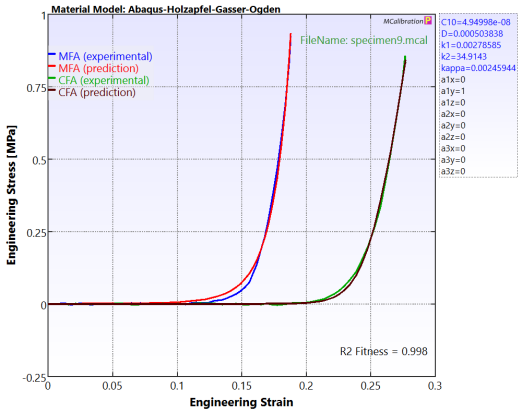

(g) Specimen 9

Figure D.1 Experimental data curve-fitted using MCalibration for the remaining three specimens

Appendix E

Cryo-Histology

E.1 Qualitative assessment of two different preparation methods

There were two methods for preserving a tissue in preparation for cryo-sectioning , namely PFA (Paraformaldehyde) and non-PFA fixed samples. The staff at the Histology in UCT's Department of Human Biology, suggested that both methods be looked at before deciding which method to follow.

Following a PFA fixed sample, the tissue is placed in a Paraformaldehyde (PFA) solution and then increased gradients of sucrose concentration (up to 30 % as cryoprotectant) is added to the solution. After soaking overnight, the tissue is removed and embedded in an optimal cutting temperature (OCT) compound and frozen in liquid nitrogen. The Non-PFA fixed method, had the tissue directly embedded in OCT compound and frozen in liquid nitrogen. To determine which method should be followed cryo-sectioned samples made following these two methods had to be viewed and compared under a microscope. Note that a haematoxylin and eosin (H&E) stain was added to the sectioned samples to make them visible under a microscope.

Figure E.1 shows images of three PFA fixed and three Non-PFA fixed samples. Immediately by looking at these images, it was seen that the PFA-fixed samples were much thicker than the Non-PFA fixed samples. This was caused by the overnight soaking causing the tissue to absorb fluid and dilate as a result.There were also larger strands of fibres fraying out of the membrane for the PFA fixed which made it more difficult for the ImageJ processing tool to correctly identify the thickness boundaries of the sectioned tissue. Given that the aim of the histology study was to determine the thickness of the sample in situ, the fact that the PFA fixed sample dilated significantly meant that the Non-PFA fixed method was the method to follow.

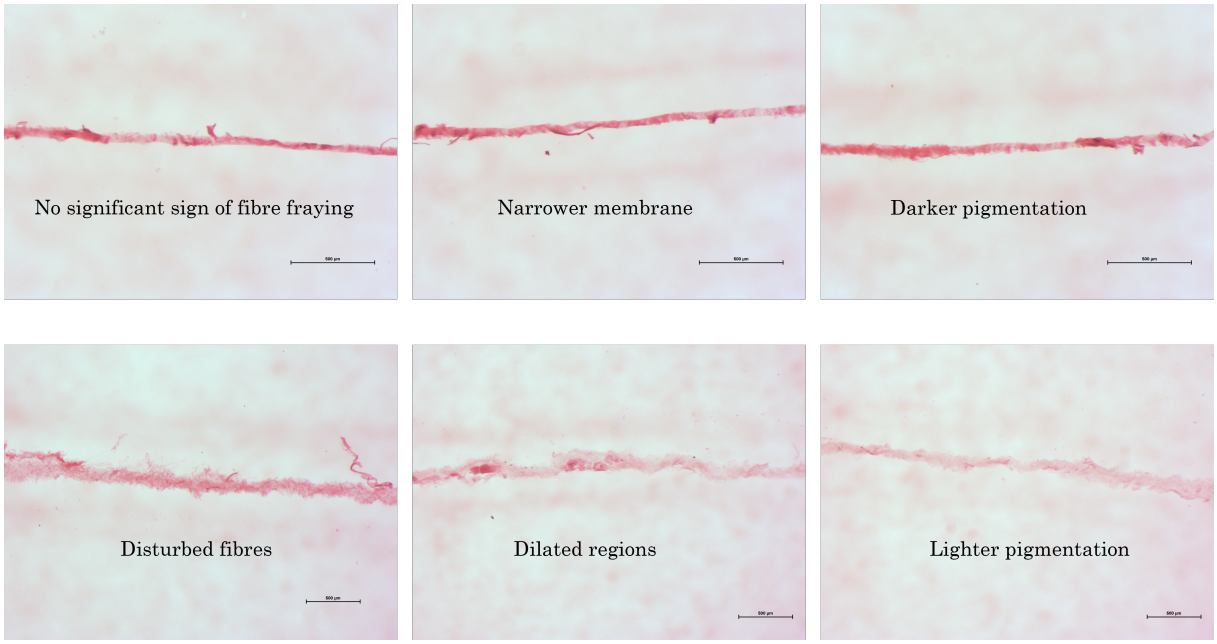

Figure E.1 Images taken of Non-PFA fixed (top row) and PFA fixed (bottom row) samples

E.2 Qualitative assessment between various section thickness used

There were three options available for the section thickness at which the frozen tissue could be sliced. These were 10 µm, 25 µm and 50 µm thick. A set of Non-PFA fixed samples were prepared and sectioned accordingly, to be assessed. Figure E.2 shows what the tissue looked like at these three different thickness.

Compared to the 25 µm and 50 µm, the 10 µm thick tissue produced the worst image to measure its cross-sectional thickness. Along the length of the sample, the tissue is discontinuous with fibres detached and speckled across the image. Regarding the 25 µm thick slide, the membrane held its shape much better than the 10 µm, with fewer discontinuities and fewer detached fibres. There were regions where the tissue seemed to curl upon itself which would produce a false reading of the samples thickness.

The 50 µm thick slide produced the cleanest image with no detached tissue making the boundary of the membrane easily identifiable using ImageJ. The density and colour of the pigmentation was also more uniform than the other two samples which also helped in isolating pixels that were tissue from the background. There were also no signs that the tissue had been disturbed during the process, with the sample holding a straight and roughly uniform shape along its length. It is important to note that theses slides were all sectioned from the same frozen embedded tissue and the alteration made was the

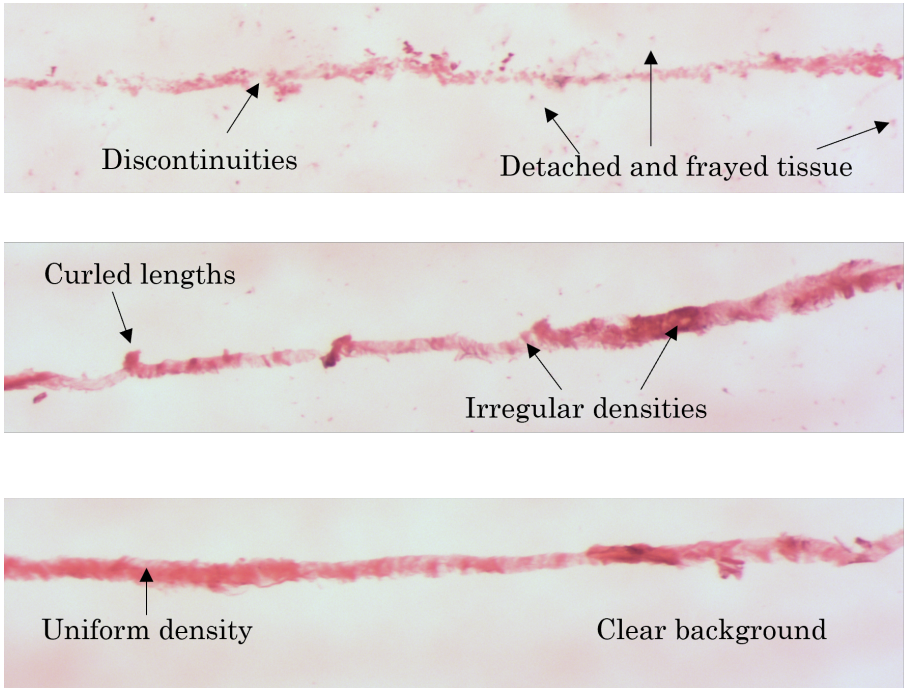

Figure E.2 Images showing tissue sectioned to 10 µm (top), 25 µm (middle) and 50 µm (bottom) thicknesses

thickness at which each section was cut. Given what was observed, it was clear that for the histology study the samples will be sectioned at 50 µm intervals.

Appendix F

Engineering Drawings

SolidWorks Academic - not for commercial use

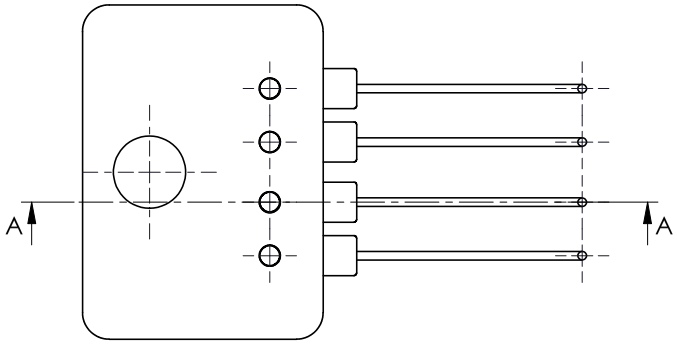

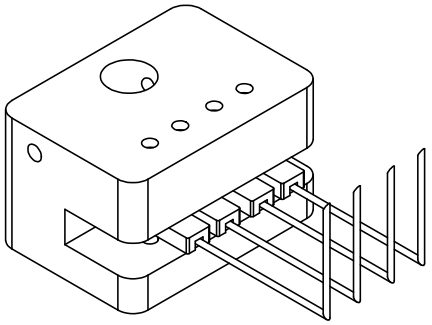

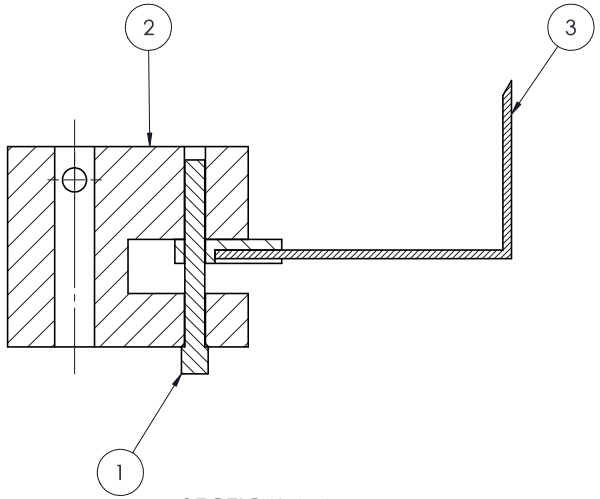

SECTION A-A
SCALE 2.5 : 1

NO.	PART NUMBER	DESCRIPTION	SPECIFICATION	QTY
3	011	Hook	See DWG for details	4
2	010	Clip	See DWG for details	1
1	009	Panel Pin		4

Scale: 5:2 on A3	University of Cape Town Department of Mechanical Engineering			
Drawn By: Aashir Siddiqui	All un-toleranced dimensions to adhere to ISO 2768-m	Title: Rake		
Checked :	Assembly drawing	Drawing Number : GA002	Rev. : A	Sheet : 1 of 1

SOLIDWORKS Educational Product. For Instructional Use Only.

SolidWorks Academic - not for commercial use

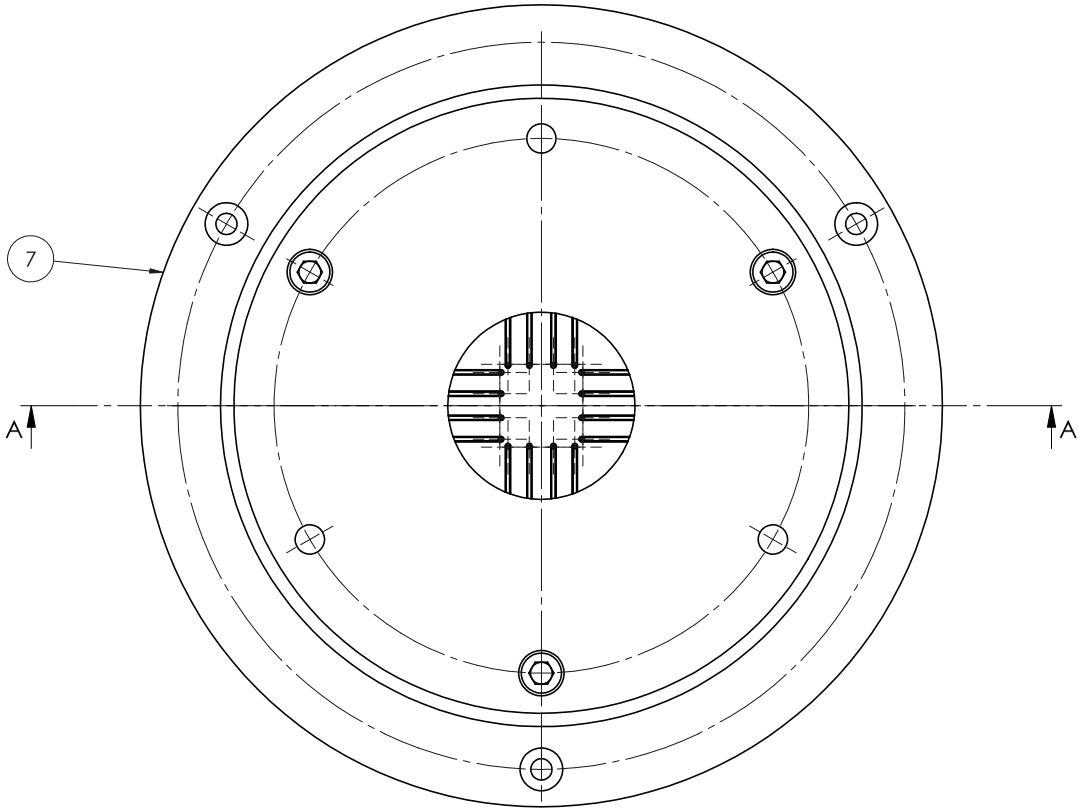

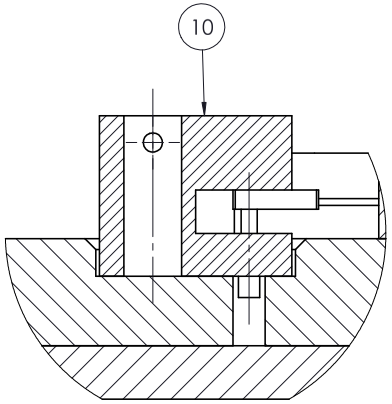

DETAIL B
SCALE 2 : 1

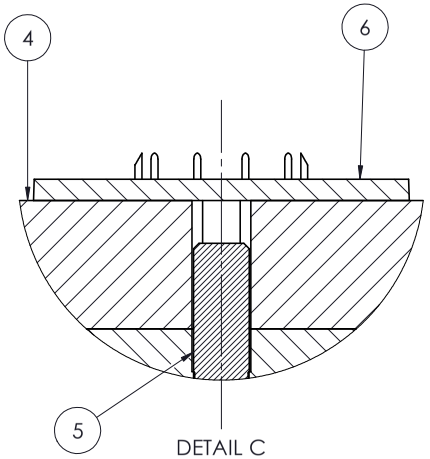

DETAIL C
SCALE 2 : 1

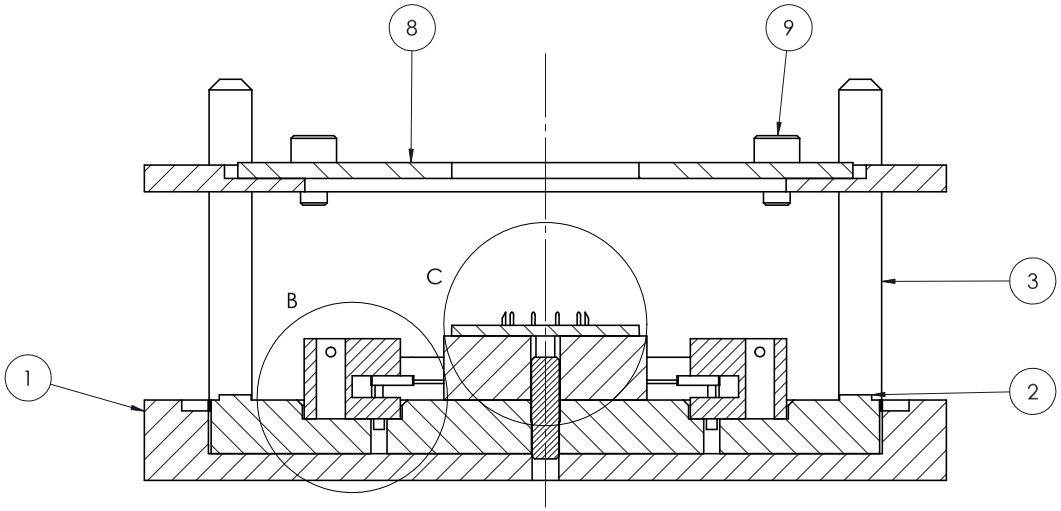

SECTION A-A
SCALE 1 : 1

NO.	PART NUMBER	DESCRIPTION	SPECIFICATION	QTY
10	GA002	Rake	See DWG for details	4
9	B18.3.1M - 5 x 0.8 x 8 Hex SHCS -- 8NHX			3
8	008	Specimen Plate	See DWG for details, Stainless Steel (ferritic)	1
7	007	Lofted Base	See DWG for details, Material <not specified>	1
6	006	Rubber Matt	See DWG for details, Material <not specified>	1
5	005	Key	See DWG for details, Plain Carbon Steel	1
4	004	Cutting Platform	See DWG for details, Material <not specified>	1
3	003	Lowering Guide	See DWG for details, Plain Carbon Steel	3
2	002	Rotatable Base	See DWG for details, Material <not specified>	1
1	001	Base Plate	See DWG for details, Plain Carbon Steel	1

Scale: 1:1 on A3	University of Cape Town Department of Mechanical Engineering			
Drawn By: Aashir Siddiqui	All un-toleranced dimensions to adhere to ISO 2768-m	Title: Rake Attachment Rig		
Checked :	Assembly drawing	Drawing Number : GA001	Rev. : A	Sheet : 1 of 1

SOLIDWORKS Educational Product. For Instructional Use Only.

SolidWorks Academic - not for commercial use

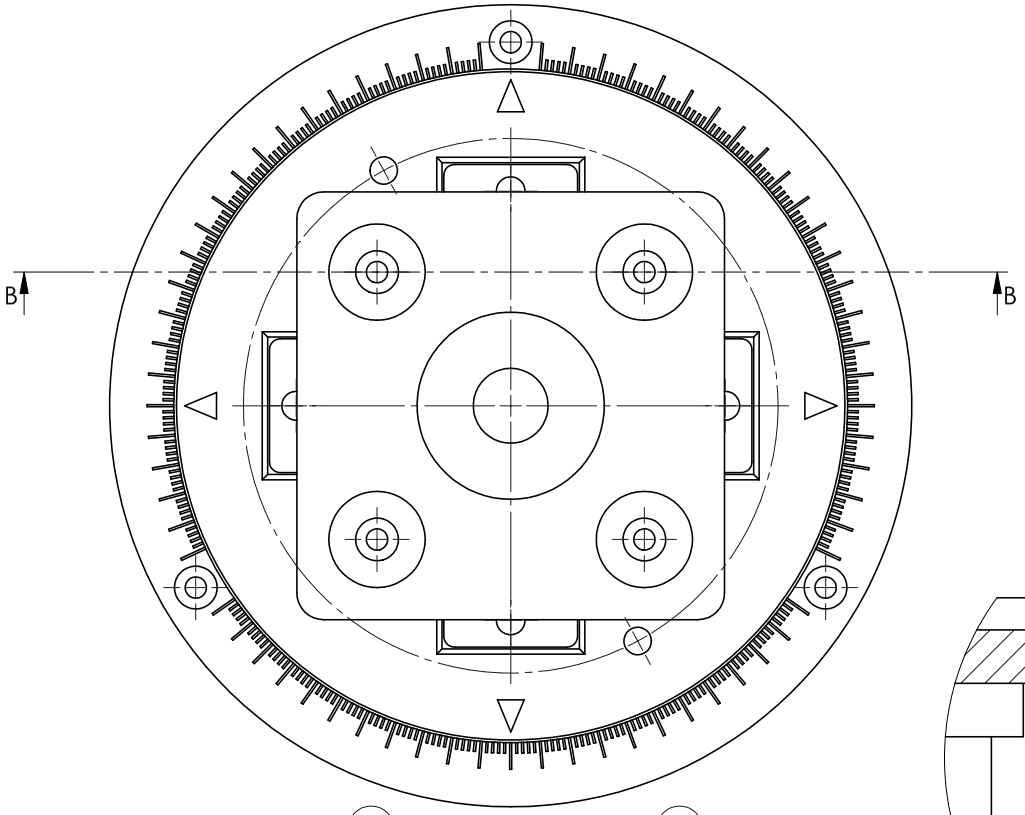

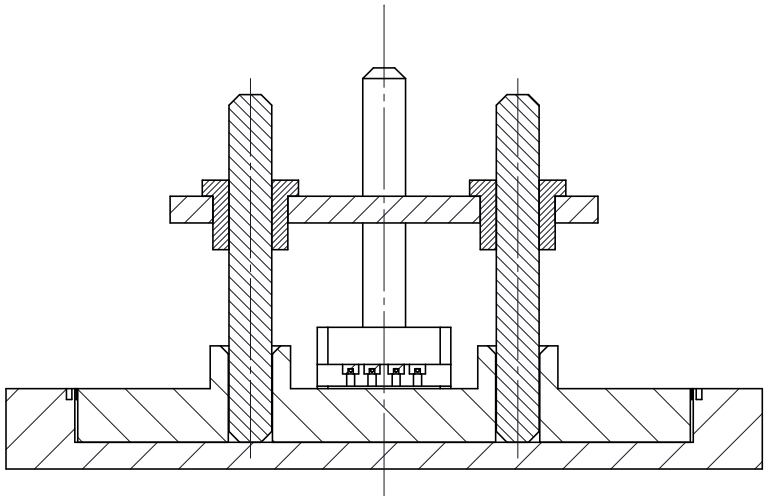

SECTION B-B
SCALE 1 : 1

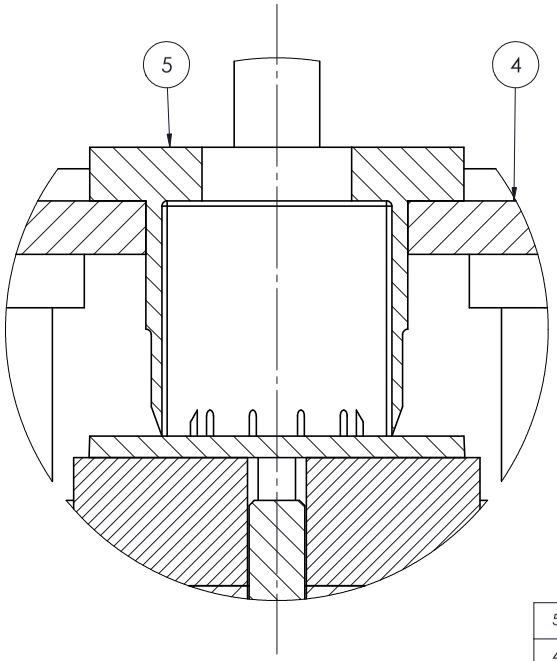

DETAIL A
SCALE 2 : 1

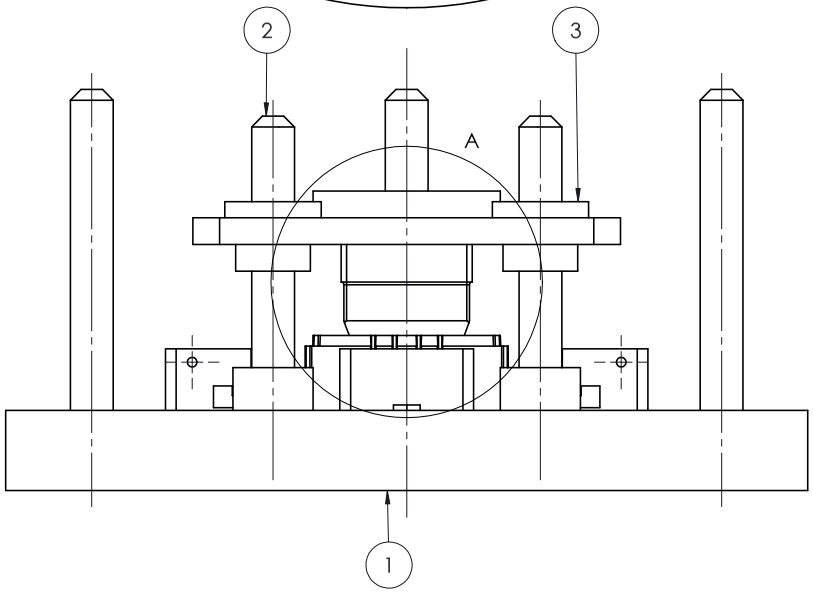

NO.	PART NUMBER	DESCRIPTION	SPECIFICATION	QTY
5	012	Square Punch	See DWG for details, Material <not specified>	1
4	013	Locating Plate	See DWG for details, Material <not specified>	1
3	014	Bushing	See DWG for details, Phosphor bronze 10% D, UNS C52400	4
2	015	Guide	See DWG for details, Material <not specified>	4
1	GA002	Rake Attachment Rig	See DWG for details	1

Scale: 1:1 on A3	University of Cape Town Department of Mechanical Engineering			
Drawn By: Aashir Siddiqui	All un-toleranced dimensions to adhere to ISO 2768-m	Title: Punch Rig		
Checked :	Assembly drawing	Drawing Number : GA003	Rev. : A	Sheet : 1 of 1

SOLIDWORKS Educational Product. For Instructional Use Only.